Investigation of Probe-Induced Dust Voids in a Weakly Magnetized Dusty Plasma

by

Spencer Paul LeBlanc

A dissertation submitted to the Graduate Faculty of
Auburn University
in partial fulfillment of the
requirements for the Degree of
Doctor of Philosophy

Auburn, Alabama
December 14, 2019

Keywords: dusty plasma, magnetized plasma, dust voids

Approved by

Edward Thomas, Jr., Charles W. Barkley Endowed Professor of Physics
Yu Lin, Alumni Professor of Physics
David Maurer, Professor of Physics
Dennis Bodewits, Associate Professor of Physics

Abstract

Dust voids, or regions free of dust grains surrounded by dusty plasmas, have been observed in a wide array of experimental configurations, from microgravity systems, to 3-dimensional dust clouds, to 2-dimensional monolayers. Broadly, these dust voids have fallen into one of two modes: voids driven by a repulsive electrostatic force on the dust grains, opposed by an inward ion drag force (ion-collecting voids); and voids driven by an outward ion drag force, maintained by an inward electrostatic force (ion-streaming voids). By configuring an rf plasma system so that the main ionization volume falls within the interior of a 2-dimensional void in a dust monolayer, a system has been created in which dust voids can display both modes, as well as a transitionary mode between the two. A modification of the Avinash model of ion-collecting dust voids is applied to the ion-streaming modes and is used to estimate the ion drift velocities in both modes. The ions are found to be both subthermal and subsonic. The voids are also placed under the influence of an externally applied magnetic field. By comparing with the non-magnetized results, the effect of the magnetic field on the electric charge of the dust grains is calculated. The voids are also observed to deform significantly under the influence of the magnetic field, and this behavior is explained via the geometry of the dust confinement potential of the rf sheath, in conjunction with a complex arrangement of plasma drifts.

Acknowledgments

There are very very many people who were vital to my success throughout the lengthy graduate school process, and I will do my best to recognize everyone. I take it as a sign of just how fortunate I am that I'm afraid this section will run quite long. First and foremost, I must thank my parents, Karen and Marcus LeBlanc, for their love and lifelong encouragement to pursue my interest in the sciences. My grandmothers, Jo Ann Massey and Myrle LeBlanc, along with all of the aunts and uncles and cousins and nieces and nephews (especially my amazingly awesome godson Luke Wiggins), and my father- and mother-in-law Gilbert Abeyta and Deborah Christian, for their limitless support throughout this process. Thanks so much to all of you.

My advisor, Dr. Edward Thomas, for his patience, assistance, and guidance over the last several years. This was only possible with your help, and I hope I didn't give you too many gray hairs in the process. Darrick Artis, without whom the entire laboratory would come to a grinding halt, was indispensable both as a technician and a friend. Dr. Uwe Konopka for his "outside the box" thinking and inspiration when most needed. Dr. Lénaïc Couëdel for his particular guidance with the design of this experiment, and his shared love of coffee.

The many other graduate students who helped me along the way. Drs. Ami DuBois, Ivan Arnold, Mark Cianciosa, Dylan Reedy, Min Khalil, and Jonathan Hebert, friends and mentors all. Dr. Brian Lynch, who I hope I didn't distract too much in the office. Dr. Taylor Hall, who I know I distracted too much in the office. Peter Traverso, who challenged me both intellectually and physically throughout our graduate school experience, and made sure I never had to worry about

what to do with leftover food. Misha McKinley, Brandon Doyle, Mohamad Menati, Lori Scott, Steve Williams, and Dylan Funk, you all had a hand in this thing too. Spenser Burrows helped get me across the finish line in both college and graduate school, and that deserves recognition.

Drs. Joe Perez and Jim Hanson both worked tirelessly as department chairs to keep this whole train on the rails, and for that they deserve thanks as well. The wonderful women who ran this department—Jennifer Morris, Freddie Killian, Prissy Goodson, Glenda Stroud, and Mary Prater—you all do so much and absolutely deserve more credit than you receive, and I'd like to thank you all sincerely from the bottom of my heart.

Last and most of all, I must thank my beloved wife Maggie Abeyta (as well as our dog Baguette). None of this would have been possible without Maggie by my side, pulling me up when I was down, and making every day better. Maggie, you're my muse and my inspiration, and I can never thank you enough for all that you do.

Table of Contents

List of Tables

List of Figures

Chapter 1 - Introduction and Plasma Background

1. Overview and Scope

Plasma, commonly referred to as the "fourth state of matter," is the most abundant form of matter in the visible universe. When an external energy source is applied to the atoms or molecules of a gas—most often in the form of either direct heating or an applied electric field, either static or oscillating—one or more of the electrons may be freed from an atom and released into the surrounding environment, forming a plasma. The result of this process is a gaseous system composed not only of electrically neutral atoms and molecules, but of negatively charged electrons and positively charged ions. This system can both create and react to electromagnetic fields in a collective manner, allowing plasmas to display both fluid and gas-like properties.

Despite being the most common state of matter in the visible universe, the awareness of plasma is relatively sparse to most people. Plasmas were not discussed in the scientific community until relatively recently, when Michael Faraday delivered a lecture on the topic of "Radiant Matter" in 1816, at the time merely a theoretical supposition of a fourth state of matter "expanded and rarefied" beyond the regime of gases. It would be not be until 1879 that this "radiant matter" first appears in scientific literature, when Sir William Crookes drew upon Faraday's remarks to describe the phenomenon of gases, when sealed and decompressed in vacuum tubes, reacting to electric potentials by "exciting phosphorescence."[1]

The study of plasmas was intermittent and sporadic for some time, highlighted primarily by Thomson's description of cathode rays in 1897[2], until Irving Langmuir began his extensive investigations in the 1920s, yielding many of the diagnostic techniques and descriptive terms still used in plasma physics today.[3,4] Indeed, it was Langmuir who first used the term "plasma" in

reference to these excited gases, as the transport of electrons through the plasma bulk reminded him of "the way blood plasma carries red and white corpuscles and germs."[5]

Today, plasma physics is a broad, diversified field with dozens of sub-fields and billions of dollars' worth of research performed around the world, both in academic and industrial settings. Plasma and its properties are used in the fabrication of semiconductors for microprocessors[6], in lighting and screens for monitors and televisions, and in plasma torches for industrial welding and cutting applications. Physicists and engineers seek to use plasma to contain nuclear fusion reactions, with the goal of providing a clean, plentiful, cost-effective energy source. Space researchers study plasmas both as an academic subject (e.g. the interstellar medium, black hole accretion disks), as well as for use as a tool for space exploration (ion thrusters and heat shielding on spacecraft).

The specific focus of this dissertation will be on dusty plasmas, a sub-field of plasma physics in which microscopic particles, or grains, are introduced into a plasma environment. By collecting ions and electrons from their surroundings, these grains acquire a net electric charge. This allows the dust to interact with the various electromagnetic fields created by the background plasma, created by the other grains, or imposed externally. In almost all cases in laboratory dusty plasmas, this charge will be negative, due to the higher mobility of the electrons. As a results, a dusty plasma is a new type of four-component plasma system composed of electrons, ions, neutral atoms, and charged dust. This also makes dusty plasmas quite attractive to experimentalists due to their ability to be observed by the naked eye, and recorded with traditional photo and video equipment.

When a central electric potential or charge concentration occurs in a dusty plasma, the dust grains will form a void, or a dust-free region of space, surrounding that point. In the case of negatively charged dust grains, the boundary of this void region occurs at a point at which a force

balance exists between an electrostatic force in one direction, and a drag force caused by (positively-charged) ions streaming in the opposite direction. Solving this force balance equation allows us to express the length scale of these voids in terms of two unknown parameters: the electric charge of the dust grains, and the flow velocity of the ions. By carefully creating and measuring these dust voids, there is valuable insight to be gained into both of these quantities, and the ways in which they change as the experimental conditions are varied.

Of great recent interest in the scientific community is the influence of magnetic fields on plasma systems. While the general effects of magnetic fields on single, isolated charged particles are well known, there are still many outstanding questions regarding the nature of collective interactions in magnetized plasmas because of the modification of particle transport parallel and perpendicular to the magnetic field. Moreover, in a dusty plasma, the presence of a magnetic field can also modify the fluxes of electrons and ions to the dust particles, not only altering their charge, but also modifying the free charge density distribution in the background plasma. As will be shown, the magnitude of a magnetic field's effect on a particle can vary drastically depending on the particle's charge-to-mass ratio. Thus, the electrons, ions, and dust grains will all have significantly different responses to an applied magnetic field.

In this dissertation, two specific physical phenomena will be investigated. The first is the ability for dust voids under the right experimental parameters to exhibit two different equilibrium modes driven by differing arrangements of the forces on the dust grains. The second is the response of these dust voids to an externally applied magnetic field, and the asymmetric nature of this response.

2. Plasma background

The primary state variables of a plasma are the density, temperature, and electrostatic potential. While each species in the plasma—electron, ion, and dust—can have a separate density and temperature, it is the spatial distribution of these charged species that gives rise to the plasma potential. From these fundamental parameters, it is then possible to derive the important physical scales that can be used to characterize the properties of the plasma. In this section, a number of important properties and physical quantities relevant to plasmas will be introduced. These will be necessary in the discussion of experimental results in Ch. 4.

a. Quasineutrality in Dusty Plasmas

An important characteristic of plasma systems is that of "quasineutrality," or the tendency for the plasma to maintain a net neutral charge over its bulk, due to the conservation of charge when neutral atoms are ionized.

This condition is expressed mathematically as

$$\sum_s n_s q_s = 0 \tag{1-1}$$

with s referring to a particular plasma species, n_s to the average number density of that plasma species, and q_s to the individual electric charge. In the specific case of a dusty plasma, this equation takes the form

$$\sum_s n_s q_s = e(n_i - n_e - Zn_d) = 0 \tag{1-2}$$

with i, e, and d referring to the ions, electrons, and dust grains, respectively, and Z referring to the average charge number of an individual dust grain within the dusty plasma.

Eq. (1-2) will be important in Ch. 2 when deriving the underlying physical model and theory of dust voids.

b. Debye Shielding

One of the most fundamental phenomena related to plasma is the ability to shield electric potentials, as from a charged dust grain.[7,8] This effect, referred to as Debye shielding, can be illustrated as a uniform, quasi-neutral background plasma of ions and electrons, into which a single positively-charged sphere is inserted. A number of electrons would be attracted into a spherical shell or cloud around the positively charged sphere, until the negative charge of this cloud was equal in magnitude to the positive charge of the sphere. At this point, a Gaussian sphere containing both the sphere and the surrounding electron cloud would contain a total charge of 0, and charged particles outside that sphere would be perfectly screened from any resulting electric fields.

In a plasma, in which the electrons are at a non-zero temperature and therefore are subject to some degree of thermal motion, there would be some electrons near the edge of this cloud which would escape the electrostatic potential of the sphere, making the shielding imperfect. The "edge" of this cloud is defined as the radius r at which the electrostatic energy $e\Phi_s$ is equal to the thermal energy $k_B T_e$, with e referring to the electron charge, $\Phi_s(r)$ to the electric potential, k_B to the Boltzmann constant, and T_e to the electron temperature.

This characteristic shielding length, referred to as the Debye length, can be calculated in a dusty plasma system as follows. We begin by examining Poisson's equation for the ions, electrons, and dust:

$$\nabla^2 \Phi = \frac{-e}{\varepsilon_0}(-n_e + n_i - Zn_d) \tag{1-3}$$

with Φ the electrostatic potential and ε_0 the permittivity of free space. The ions and electrons are taken to be in Boltzmann equilibrium:

$$n_s = n_{s,0} e^{\frac{-q_s \Phi}{k_B T_s}} \tag{1-4}$$

Far away from the test charge, the electrostatic energy will be quite small, so the thermal energy will dominate $k_B T_e \gg |q_s \Phi|$ and Eq. (1-4) can be simplified by taking the Taylor expansion of the exponential and keeping only the first (linear) term:

$$n_s \approx n_{s,0}\left(1 - \frac{q_s \Phi}{k_B T_s}\right) \tag{1-5}$$

Using the quasineutrality condition Eq. (1-2) and substituting Eq. (1-5) into Eq. (1-3) for both the ions and electrons yields the differential equation

$$\nabla^2 \Phi - \left(\frac{e^2 n_{e,0}}{\varepsilon_0 k_B T_e} + \frac{e^2 n_{i,0}}{\varepsilon_0 k_B T_i}\right)\Phi = 0 \tag{1-6}$$

In order to solve this differential equation, the Debye length for a plasma species *s* is defined:

$$\lambda_{Ds} = \sqrt{\frac{\varepsilon_o k_B T_s}{e^2 n_{s,0}}} \tag{1-7}$$

This allows Eq. 1-6 to be rewritten more simply as:

$$\nabla^2 \Phi - \left(\frac{1}{\lambda_{De}^2} + \frac{1}{\lambda_{Di}^2}\right)\Phi = 0 \tag{1-8}$$

This differential equation can be solved by defining the dust Debye length λ_{Dd} as a combination (due to the dusty plasma quasi-neutrality equation) of the ion and electron Debye lengths, defined as

$$\frac{1}{\lambda_{Dd}^2} = \frac{1}{\lambda_{De}^2} + \frac{1}{\lambda_{Di}^2} \tag{1-9}$$

The Debye lengths associated with various plasma species are frequently used as useful and convenient units when characterizing various phenomena. The Debye length can be thought of as

the fundamental length scale for interactions and effects within a plasma system. The solutions to Eq. (1-8) take the form

$$\Phi(r) = -\frac{Z_d e}{4\pi\varepsilon_0 r} e^{-r/\lambda_{Dd}} \tag{1-10}$$

This is referred to as the Debye potential, or the shielded Coulomb potential, and describes the resultant electrostatic potential a distance r from a dust grain with a charge of $Z_d e$. The potential decays far more rapidly in r than would the potential due to the same charge in a vacuum, the result of the Debye shielding effect. Far away from the dust grain the resultant potential is 0. It is worth noting that due to the effects of the dusty plasma quasi-neutrality condition (Eq. (1-2)), the shielding length is dependent only on the unperturbed densities and temperatures of the ions and electrons, as can be seen in Eq. (1-7).

c. Gyromotion

When an external magnetic field is introduced to a plasma system, the transport of particles is modified significantly. This can be shown by calculating the trajectory at the single particle scale. The equation of motion for a single particle of mass m and charge q in a magnetic field $\vec{B} = B\hat{z}$ is written:

$$m\frac{d\vec{v}}{dt} = q(\vec{v} \times \vec{B}) \tag{1-11}$$

Carrying out this cross section and separating variables:

$$m\dot{v}_x = qBv_y \tag{1-12}$$

$$m\dot{v}_y = -qBv_x \tag{1-13}$$

$$m\dot{v}_z = 0 \tag{1-14}$$

Taking time derivatives of Eqs. (1-12) and (1-13) and dividing by m yields:

$$\ddot{v}_x = \frac{qB}{m}\dot{v}_y = -\left(\frac{qB}{m}\right)^2 v_x \tag{1-15}$$

$$\ddot{v}_y = -\frac{qB}{m}\dot{v}_x = -\left(\frac{qB}{m}\right)^2 v_y \tag{1-16}$$

The motion described by these equations is mathematically equivalent to that of a simple harmonic oscillator operating at the cyclotron frequency of that species, defined as:

$$\omega_{c,s} \equiv \frac{|q_s|B}{m_s} \tag{1-17}$$

With $v_\perp$ denoting the speed of the particle in the $x-y$ plane (perpendicular to $\vec{B}$), the x and y velocities are then determined as:

$$v_x = v_\perp e^{i\omega_c t} \tag{1-18}$$

$$v_y = iv_\perp e^{i\omega_c t} \tag{1-19}$$

so that the particle's speed perpendicular to $\vec{B}$ remains constant:

$$v_\perp = \sqrt{v_x^2 + v_y^2} = constant \tag{1-20}$$

and the x and y positions as a function of time are expressed:

$$x(t) = x_0 - i\frac{v_\perp}{\omega_c}e^{i\omega_c t} \tag{1-21}$$

$$y(t) = y_0 + \frac{v_\perp}{\omega_c} e^{i\omega_c t} \tag{1-22}$$

We may define the Larmor radius (also referred to as the gyroradius) as:

$$r_L \equiv \frac{v_\perp}{\omega_c} = \frac{m v_\perp}{|q|B} \tag{1-23}$$

A charged particle in the presence of an external magnetic field will thus exhibit so-called gyromotion, orbiting around a magnetic field line at a radius r_L and at a frequency ω_c.

d. E x B Drift

The motion of a charged particle is further modified in the presence of combined magnetic and electric fields when there is a component of the electric field that is perpendicular to the magnetic field. Using the complete Lorentz force equation, i.e., by adding the electric force to Eq. 1-11, it is possible to investigate the resulting particle transport:

$$m\frac{d\vec{v}}{dt} = q\left(\vec{E} + \vec{v} \times \vec{B}\right) \tag{1-24}$$

Taking for simplicity the portion of the electric field which is perpendicular to the magnetic field to lie on the x-axis, so that $\vec{E} = E_x\hat{x} + E_z\hat{z}$ and $E_y = 0$, the x, y, and z components of this equation are now:

$$\frac{dv_x}{dt} = \frac{q}{m}E_x + \omega_c v_y \tag{1-25}$$

$$\frac{dv_y}{dt} = -\omega_c v_x \tag{1-26}$$

$$\frac{dv_z}{dt} = \frac{q}{m}E_z \tag{1-27}$$

Differentiating these equations to solve for the velocities, the solutions are:

$$v_x = v_\perp e^{i\omega_c t} \tag{1-28}$$

$$v_y = v_\perp e^{i\omega_c t} - \frac{E_x}{B} \tag{1-29 }$$

$$v_z = v_{z0} + \frac{qE_z}{m}t \tag{1-30}$$

The general effect of the electric field, therefore, is twofold: the linear acceleration in the z direction (or more generally, along the axis parallel to the magnetic field), and the drift of the guiding center of gyromotion in the $\vec{E} \times \vec{B}$ direction, expressed most simply as:

$$\vec{v}_{E\times B} = \frac{\vec{E} \times \vec{B}}{B^2} \tag{1-31}$$

e. Hall Parameter

The Hall parameter is a frequently used dimensionless quantity to describe the degree of magnetization of a low-temperature plasma in which the electrons and ions are subject to collisions with neutral atoms. The Hall parameter is expressed as the ratio of the cyclotron frequency to the neutral collision frequency:

$$H_s = \frac{\omega_{c,s}}{\nu_{n,s}} \tag{1-32}$$

where $\omega_{c,s}$ represents the cyclotron frequency

$$\omega_{c,s} = \frac{q_s B}{m_s} \tag{1-33}$$

with q_s the species electric charge, B the external magnetic field, and m_s the species mass. $\nu_{n,s}$ represents the frequency of collisions between the species s and background neutral atoms,

$$\nu_{n,s} = \frac{\upsilon_{th,s}}{\lambda_{mfp,n-s}} \tag{1-34}$$

where $\upsilon_{th,s}$ represents the thermal velocity of species s:

$$\upsilon_{th,s} = \sqrt{\frac{8k_B T_s}{\pi m_s}} \tag{1-35}$$

with k_B representing the Boltzmann constant and T_s the species temperature. $\lambda_{mfp,n-s}$ refers to the s-neutral collision mean free path

$$\lambda_{mfp,n-s} = (n_n \sigma_{s-n})^{-1} \tag{1-36}$$

with n_n the neutral atom number density and σ_{s-n} the scattering cross section between the species s and the neutrals.

The Hall parameter represents a comparison of how much a species' motion is affected by gyromotion due to the external magnetic field or by random collisions with background neutral atoms. When the Hall parameter for a particular plasma species is high ($H_s \gg 10$), that species is said to be strongly magnetized. Fig. (1-1) shows both the ion and electron Hall parameter across a range of neutral pressures and magnetic field strengths.

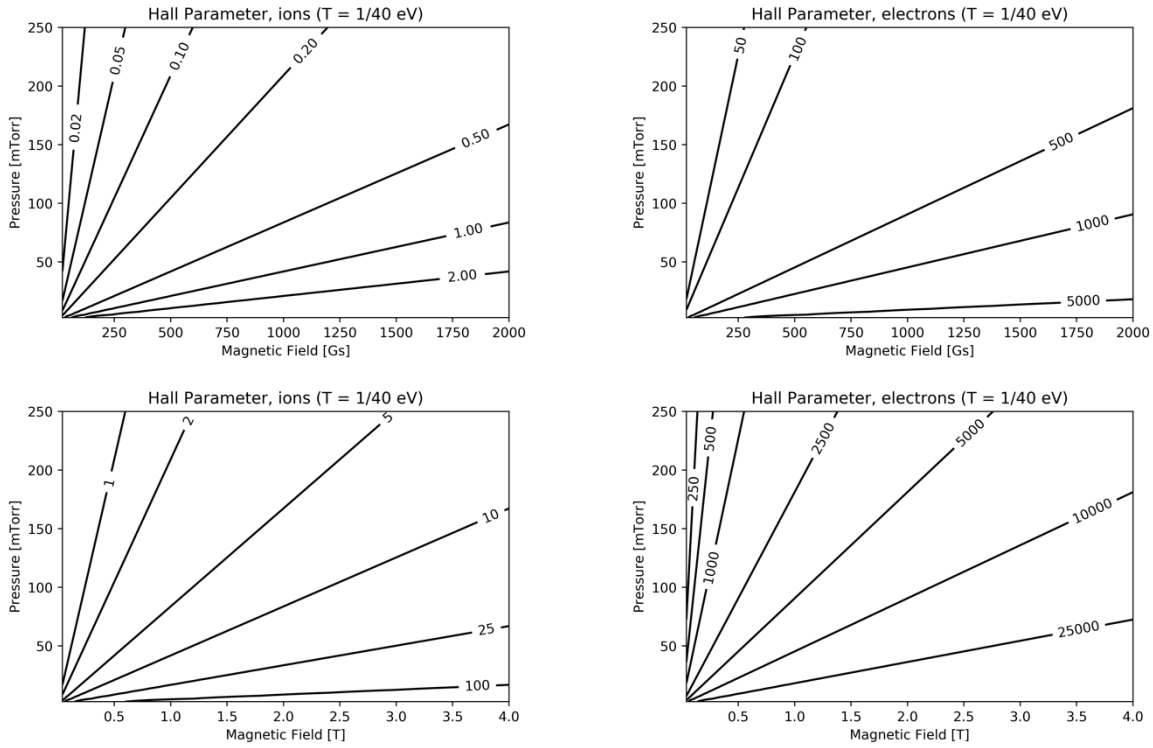

Figure 1-1: The Hall parameter of a plasma species indicates its degree of magnetization. The higher a species' Hall parameter, the more its motion is dominated by the effect of the magnetic field. A species is said to be magnetized if its Hall parameter is greater than unity ($H_s > 1$), and at very large values ($H_s \gg 10$) is referred to as strongly magnetized. The top two figures represent the ion and electron (respectively) Hall parameters across a range of pressures and magnetic field strengths typical of the 3DPX chamber (see Ch. 3), and therefore will be relevant to most of the experimental data presented in this work. The lower two figures are at much higher field strengths, such as those found in the MDPX device (see #-#), where the very large fields allow access to strongly magnetized states of both ions and electrons.

3. Dusty Plasmas

Dusty plasmas, also referred to as complex plasmas, are plasma systems which contain the usual species of positively charged ions, negatively charged electrons, and neutral atoms, with the addition of a fourth component of dust particles. These dust particles, or dust grains, typically have a radius of hundreds of nanometers to tens of microns. By interacting with the background plasma environment, these dust grains can collect ions and electrons and acquire a net electric charge, allowing the grains to respond to the plasma environment around them. In most systems, the dust grains will collect more electrons than ions (due to the higher mobility of the electrons) and thus reach a net negative electric charge.

One of the most attractive qualities of dusty plasmas as a topic of scientific inquiry is the fact that these charged dust grains are large enough to be seen with the naked eye and, more significantly, photographed using traditional (visible light) optics methods. With the use of monochromatic light from a laser, dust grains can be illuminated within the plasma environment and the light scattered from their surfaces can be collected with inexpensive, off-the-shelf optics and camera systems. This data can yield great insight into the background plasma in which the grains are located, as well as about the dynamics and processes of the dust grains themselves.

The motivations which drive scientific investigations of dusty plasma systems are varied and complex, but largely they can be sorted into three broad categories. Researchers may study the properties of the dust grains themselves, such as their charging process[9–14], interactions with background plasma species and one another[15–19], kinetic effects, etc. ("dust as dust" studies). Other investigations make use of a dusty plasma system as an approximation for another physical system which is either more difficult to study directly or more difficult to diagnose ("dust as analogue" studies), such as the work of Feng and Goree[20] using a dusty plasma to measure temperature

gradients in the vicinity of shear flows, an investigation ultimately more directly relevant to fluid mechanics. Finally, researchers may use the dust as an *in-situ* diagnostic method with which to better understand the characteristics of the background plasma, for instance as "plasma buoys" to observe ion flows ("dust as diagnostic" studies).[21–27]

The work presented here will fall largely into this third "dust as diagnostic" category, making use of dust grains (specifically suspended in a dust void) to infer information about the flows of ions and electrons in a dusty plasma. There will also be some discussion of the dust charging process within a magnetic field ("dust as dust").

In addition to those introduced above, there are additional concepts and physical quantities specific to dusty plasmas which will now be described.

a. Coulomb Coupling Parameter

Plasma systems are often described by the so-called Coulomb coupling parameter[8,28], which represents the ratio of the electrostatic potential energy of of a plasma species to its thermal (kinetic) energy.

$$\Gamma = \frac{E_{electric}}{E_{thermal}} \tag{1-37}$$

For (singly-ionized) ions and electrons, this can be written:

$$\Gamma = \left. \frac{e^2}{4\pi\epsilon_0 \langle r_s \rangle} \right/ kT_s \tag{1-38}$$

with $\langle r_s \rangle$ representing the average inter-particle distance. For ions and electrons, this expression becomes:

$$\Gamma = \frac{e^2}{4\pi\epsilon_0 kT_s} \sqrt[3]{\frac{4\pi}{3} n_s} \tag{1-39}$$

For typical values in a low-temperature plasma system, with ion and electron temperatures of $kT_i = 0.025$ eV and $kT_e = 3$ eV, and densities of $n_i = n_e \equiv n \sim 10^{15}$ m^{-3}, the coupling parameters are $\Gamma_i = 9.27 \times 10^{-3}$, and $\Gamma_e = 7.73 \times 10^{-5}$. Even at these very low temperatures, the relatively low density of these plasma systems means that the ions and electrons will always be very weakly coupled. That is to say, their motion is dominated by their thermal energy, rather than the inter-particle interactions among them.

Because dust grains can carry much higher charges, they can exist in strongly coupled regimes even in low-temperature plasma systems, with the dust grains at room temperature. The Coulomb coupling parameter for the dust grains is written:

$$\Gamma = \left(\frac{Q_d^2 / 4\pi\epsilon_o \Delta_d}{k_B T_d} \right) e^{-\Delta_d / \lambda_{Dd}} \tag{1-40}$$

$$\Gamma = \frac{Z^2 e^2}{4\pi\epsilon_0 \Delta_d k_B T_d} e^{-\Delta_d / \lambda_{Dd}} \tag{1-41}$$

Here, Δ_d is the average inter-particle distance between dust grains. For dust grains that are on average 5 μm apart and have a charge of 4000 electron charges, the dust coupling parameter is $\Gamma_d = 230$. By introducing the dust into the system, researchers gain access to a component that is quite strongly coupled, allowing for investigations of new physical regimes.

When the dust has a low coupling parameter and is primarily governed by the kinetic energy term, the grains will exhibit phenomena typical of ions and electrons: wave effects[29–34], flows[12,22,35–39], instabilities[21,40–44], etc. Such a dusty plasma is said to be "weakly coupled." When the electric energy among dust grains dominates, however, the system is said to be "strongly coupled," and the dust will undergo phase transitions, ultimately self-organizing into a hexagonal

structure referred to as a Coulomb crystal.[45–48] These crystal structures are observed to form when the coupling parameter has exceeded a critical value $\Gamma_c = 170$.[49]

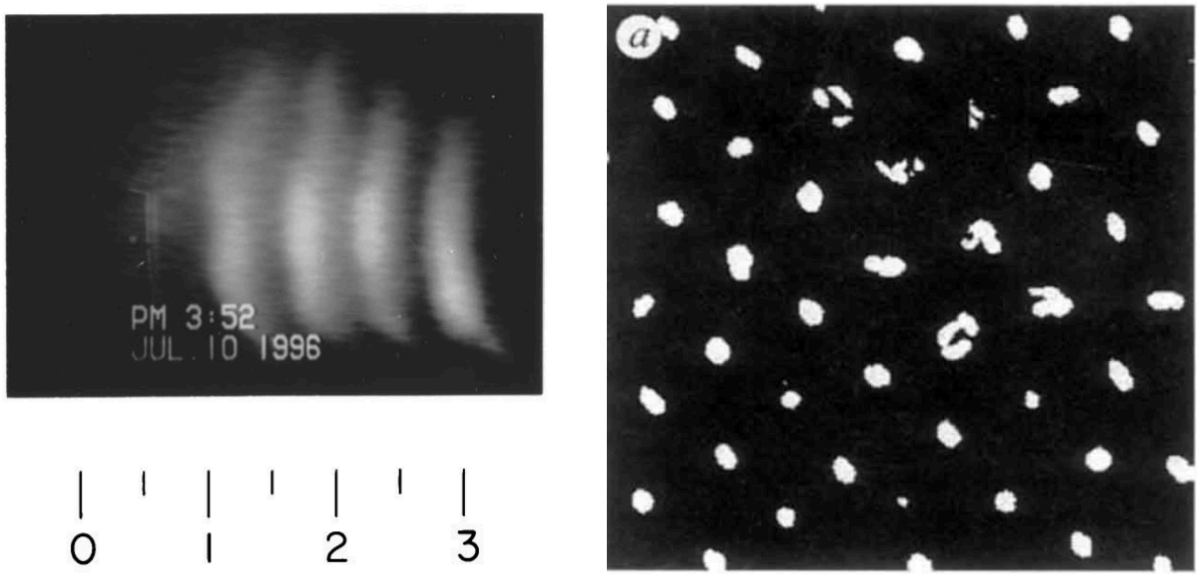

(a) **(b)**

Figure 1-2: An example of the difference between a weakly (a) and strongly (b) dusty plasma system. The dust coupling parameter indicates the degree to which the behavior of the dust is governed predominantly by its thermal energy (weakly coupled) or electric energy (strongly coupled). (a) — First published image of a dust-acoustic wave (DAW) in a dusty plasma system.[30] First theorized in 1990,[29] DAWs are formed when an external electric field causes a relative drift between the ions and dust grains. DAWs occur on length scales visible to the human eye and recordable with cameras operating in the visible spectrum, and for propagating at frequencies which can be resolved visually (a few tens of Hz). (b) — First-published image of a Coulomb crystal in a dusty plasma.[45] These crystal structures are formed when the combination of the inter-dust electrostatic force and the damping force of the surrounding neutral atoms dominate the thermal motion of the dust grains, and the particles form rigid, static hexagonal structures.

b. Dust Charging

Dust grains suspended in a plasma will accumulate an electric charge by collecting charges from the surrounding environment. In estimating the net charge of an individual dust grain, consider the flux of ions and electrons from the background plasma to the surface of the grain. We

will refer to the total current to a dust grain as I_t, which is composed of the ion and electron currents, I_i and I_e, respectively. We can relate these currents simply as

$$I_t = \frac{dQ_d}{dt} = I_i + I_e \tag{1-42}$$

To estimate the particle charge, the approach that is presented in the textbook of Shukla and Mamun[8] is used as the framework for this discussion. It is assumed that the ions and electrons are described by Maxwellian velocity distributions, and that the zero order ion and electron densities are the same, due to the quasineutrality condition (Eq #-#):

$$n_{i0} = n_{e0} \equiv n_0 \tag{1-43}$$

The full derivation of the ion and electron charging currents to the dust grain is beyond the scope of this work, but can be found in Shukla and Mamun's text, as well as in Piel's.[50] Integrating the contributions of all velocities over the full solid angle 4π across the collection cross section, the collection currents are calculated as:

$$I_i = 4\pi a^2 e n_0 \left(\frac{8k_B T_i}{\pi m_i}\right)^{1/2} \exp\left(1 - \frac{e\varphi_d}{k_B T_i}\right) \tag{1-44}$$

$$I_e = -4\pi a^2 e n_0 \left(\frac{8k_B T_e}{\pi m_e}\right)^{1/2} \exp\left(\frac{e\varphi_d}{k_B T_e}\right) \tag{1-45}$$

where a is the dust grain radius and φ_d is the dust grain surface potential (measured relative to the plasma space potential, taken here to be 0 for simplicity).

When exposed to a typical plasma, a dust grain will immediately begin collecting both ions and electrons due to the random thermal motion of both species. However, because the electrons are generally much more energetic (often having a temperature three orders of magnitude higher

than the ions), the dust grain will gather electrons much more quickly, and begin to develop a negative charge. At a certain point, the resulting negative electric potential of the dust grain will cause the ion current to increase and the electron current to decrease, until an equilibrium point is reached at which

$$\frac{dQ_d}{dt} = I_i + I_e = 0 \tag{1-46}$$

Noting that (for negatively charged dust) $Q_d = -4\pi\varepsilon_0 a|\varphi_d|$, Eqs. (1-44) and (1-45) can be combined with Eq. (1-46), yielding:

$$\left(\frac{m_i T_i}{m_e T_e}\right)^{1/2}(1-P)\exp\left(\frac{e\varphi_d}{k_B T_e}\right) + \left(1 - \frac{e\varphi_d}{k_B T_i}\right) = 0 \tag{1-47}$$

where P is the Havnes parameter:

$$P \equiv \frac{Z_d n_{d0}}{n_{i0}} \tag{1-48}$$

or, substituting the definition of ion Debye length:

$$P = \frac{4\pi n_{d0} a \lambda_{Di}^2 e\varphi_d}{k_B T_i} \tag{1-49}$$

Eq. (1-47) can be solved numerically for the dust surface potential φ_d (Fig. (1-3)) and, via the Havnes parameter, for the dust charge $Z_d$as well Fig. (1-4). In essence, the $(1-P)$ term in Eq. (1-47) is a way to account for depletion of ion and electron densities as the dust grains collect them, using quasineutrality. This depletion means that the dust grains do not accumulate as high a magnitude of charge as they would in an environment with an effectively unlimited supply of particles to draw from. The effect of this depletion can be seen in Fig. (1-4).

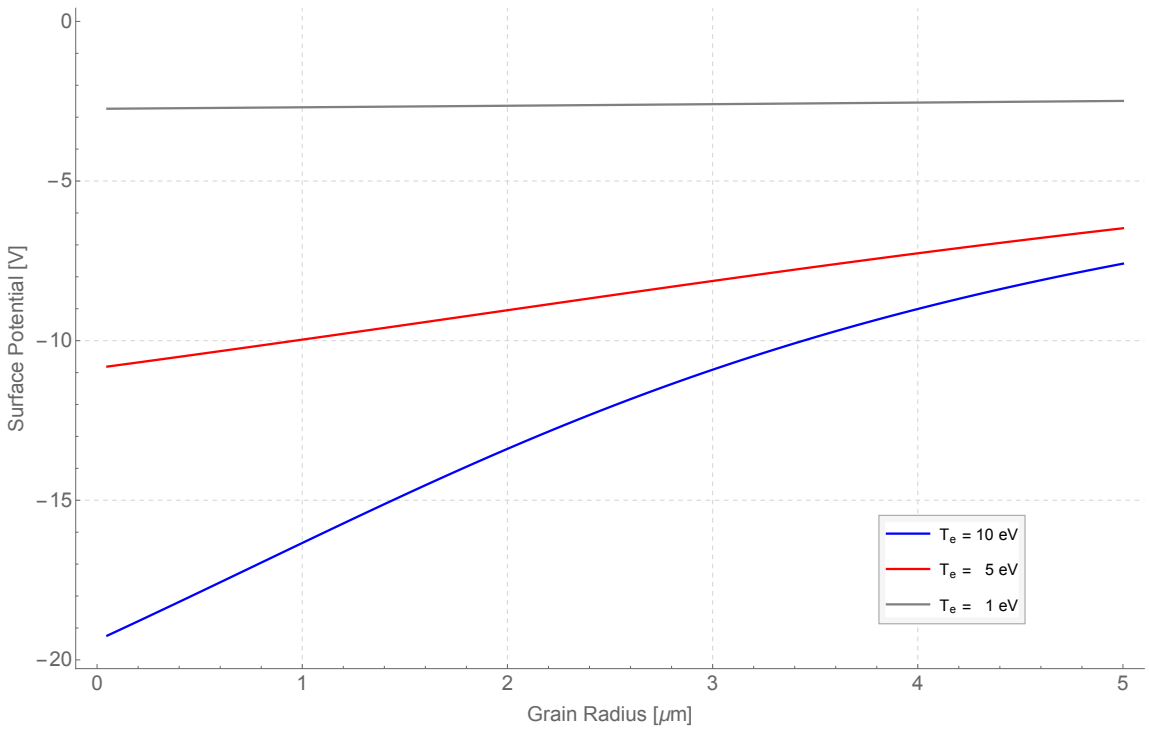

Figure 1-3: Surface potential of dust grains, in Volts, as a function of the grain radius, across a range of electron temperatures. These calculations assume room temperature ions ($T_i = 0.025\ eV$).

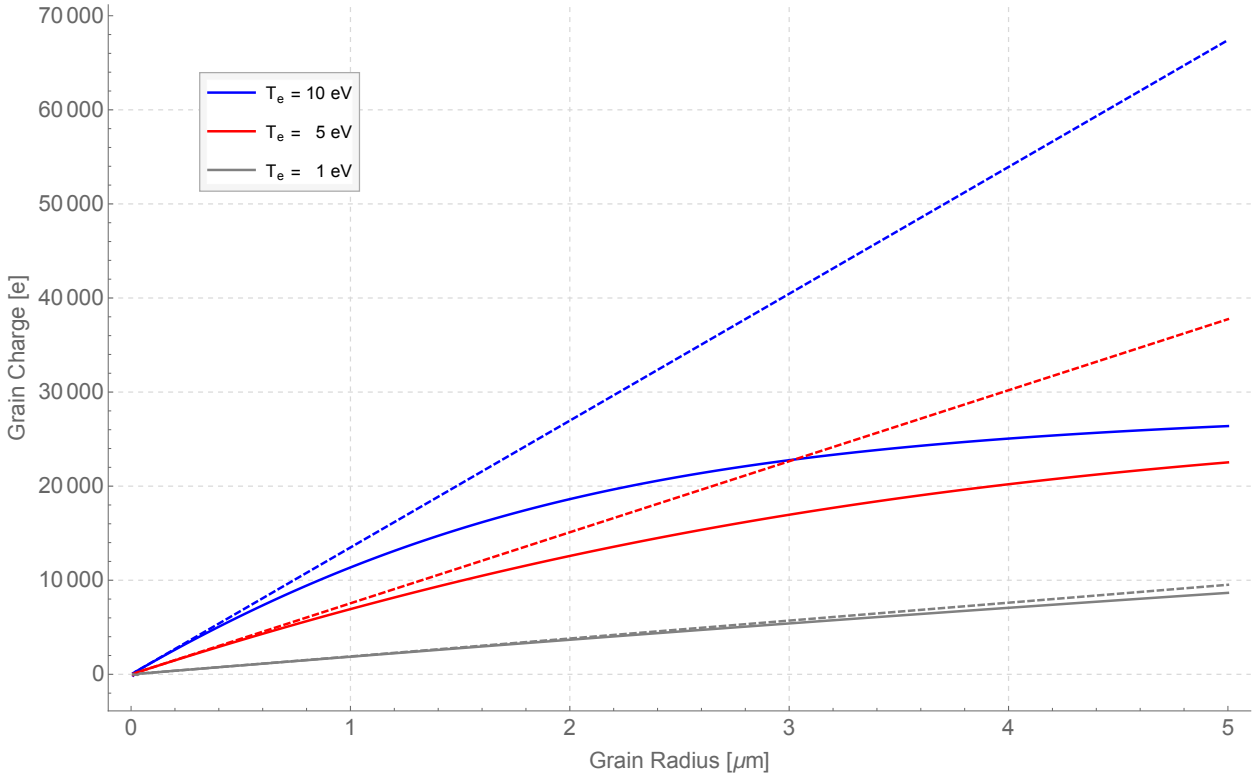

Figure 1-4: Dust grain equilibrium charge, in units of elementary charges [e]. The dashed lines indicate the calculated values without accounting for charge depletion via the Havnes parameter, while the solid lines indicate modification to the dust grain charge accounting for charge depletion. For warm electron populations, the effect of charge depletion can be quite significant, especially for larger dust grains.

c. Ion Drag Force

In the presence of a background ion current driven by an electric field, dust grains in a plasma will receive a transfer of momentum from the ions. This ion drag force consists of two components, one arising from the direct collection of ions on the surface of dust grains, and one arising from the effect of Coulomb collisions. The framework for this derivation is based upon the treatment of the topic in the plasma physics textbook by Piel,[50] as well as the dusty plasma physics textbook by Shukla and Mamun.[8]

The collection term of the ion drag force encompasses the momentum transferred to the dust grain by all ions which land on the particle surface and are thus collected. Each ion impacting the

dust grain carries an amount of momentum $m_i v_0$, where v_0 represents the velocity of an ion far away from the dust grain. The total force is calculated from the momentum flux over the collection cross-section:

$$F_{coll} = n_i(m_i v_0)v_0\sigma_{coll} \tag{1-50}$$

For ion collection, the cross-section may be calculated from Orbit Motion Limited (OML) theory:

$$\sigma_{coll} = \pi b_{coll}^2 = \pi a^2\left(1 - \frac{2e\Phi_d}{m_i v_0^2}\right) \tag{1-51}$$

The full collection term of the ion drag force is thus:

$$F_{coll} = n_i m_i v_0^2 \pi a^2\left(1 - \frac{2e\Phi_d}{m_i v_0^2}\right) \tag{1-52}$$

The Coulomb drag (also called the orbital drag) results from an ion being deflected by the electrostatic field that is generated by the charges on the grain surface, but not being collected by the grain. This term of the ion drag force is expressed similarly to the collection term:

$$F_{Coul} = n_i(m_i v_0)v_0\sigma_{Coul} \tag{1-53}$$

The Coulomb collision cross-section is:

$$\sigma_{Coul} = 4\pi b_{\pi/2}^2\Gamma \tag{1-54}$$

where $b_{\pi/2}^2$ is the impact parameter of an incoming ion whose scattering angle is $\pi/2$:

$$b_{\pi/2} = \frac{eQ_d}{4\pi\epsilon_0 m_i v_0^2} \tag{1-55}$$

and Γ is the Coulomb logarithm integrated from the collection impact parameter b_c to the electron Debye length λ_{De}. There is some contention within the literature with regards to the proper upper

boundary of this integral, but for ion velocities much smaller than the Bohm velocity $v_B = \sqrt{\frac{kT_e}{m_i}}$, the electron Debye length is appropriate.

The remainder of this work will be organized as follows. Chapter 2 will provide a more in-depth explanation of the current theories of dust voids and the effects of a magnetic field on a dusty plasma. Chapter 3 will detail the experimental systems and diagnostic methods used in this investigation. Chapter 4 will present experimental results, explain how they are processed and analyzed, and reconcile these results with the theory. Chapter 5 will summarize the findings of this dissertation and discuss potential future work to be undertaken in the field of magnetized dusty plasmas.

Chapter 2 - Theory

For nearly 25 years now, dusty plasma investigators have reported on the presence of dust voids within dusty plasmas. Dust voids are sustained regions of the plasma in which no dust grains are present, and these regions are often partially or entirely surrounded by regions containing a high density of dust grains. In general, it is assumed that the dust voids are formed as a result of the competition between an electric force on the grains and a second force, often ion drag, that acts in the opposite direction of the electric force.

Void regions in dusty plasmas have been observed under a wide variety of experimental conditions, from ground-based experiments involving particle growth to microgravity experiments using rf generated plasmas. This chapter will provide a brief overview of experimental configurations under which voids have been observed and provide a theoretical description for void formation.

1. Dust Void History

In 1996 Praburam and Goree reported on the dynamics of a system in which nanometer-scale dust particles were grown within a plasma environment. Among the observed effects, the authors described the growth and subsequent collapse of a region within the dusty plasma bulk in which no dust was present, referred to in subsequent publications as the “great void mode.” This great void mode can be seen in Fig. (2-1).

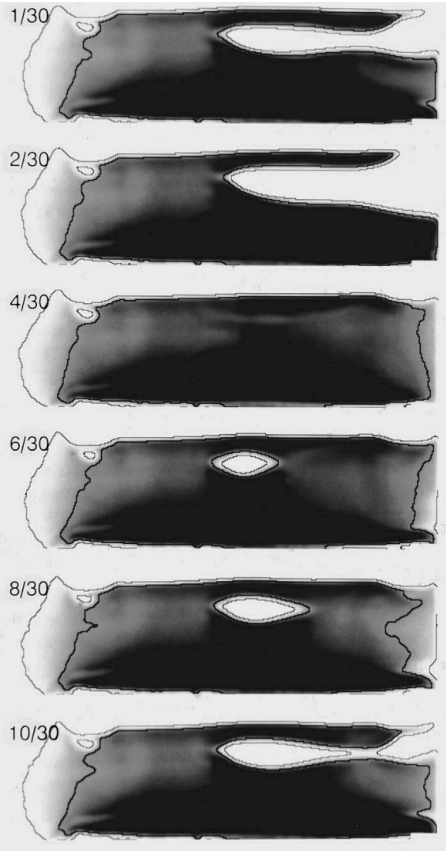

Figure 2-1: The "great void mode" was the first published example of a dust-free region within the volume of a dusty plasma.[51] This 3-dimensional void rotated in place with a period of ~9/30 s (3.3 Hz). Viewed within the horizontal observation plane of the experiment, this rotation created the illusion that is volume was changing over time. (Figure 5 in the original publication.)

The authors proposed that the dust voids were created by two opposing forces. The first was an electrostatic force driving the dust grains away from the electrodes and towards the plasma center. The other opposing force was an ion drag force away from the center, where ionization was most prevalent and thus created a maximum in the plasma potential. It was noted that the plasma glow within the void region was particularly bright, suggesting a denser, hotter local electron population.[51]

In the following years, dust voids were reported in a variety of experimental configurations. "Self-induced" voids, as those reported by Praburam and Goree, were observed in additional

particulate growth experiments[21,52], in microgravity environments[53–55], and in earth-based experiments in which the dust grains were arranged both in a 3-dimensional cloud[56] and in a 2-dimensional monolayer.[57]

In 1999, Morfill et. al. observed a large, centralized void within the 3-dimensional dust cloud created in a microgravity experiment carried out both on parabolic flights and sounding rockets. The researchers concluded that the dominant forces creating the force equilibrium in this case were the inward electrostatic force drawing the dust grains toward the region of highest potential, and the outward thermophoretic force. This conclusion was supported by the fact that reducing the rf power (and therefore the heating) to the plasma caused the void to decrease in size.[53] An image of this microgravity dust void can be seen in Fig. (2-2).

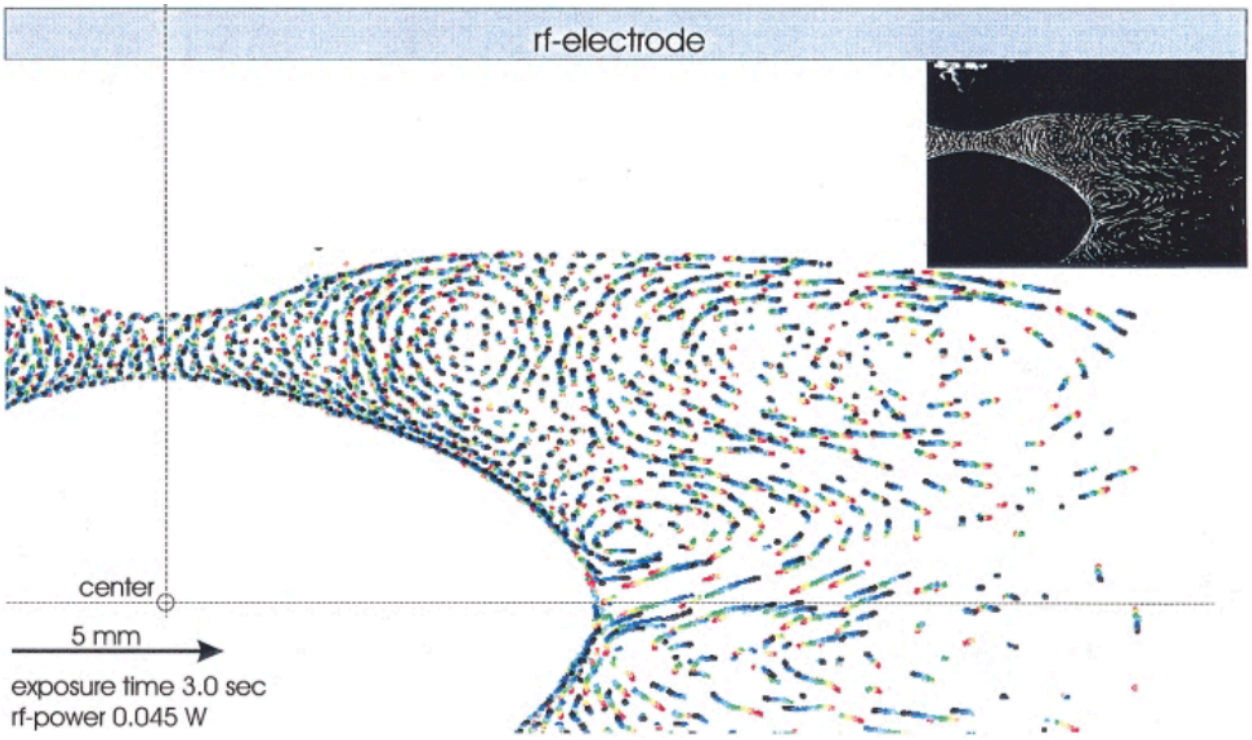

Figure 2-2: A self-induced dust void observed under microgravity. As opposed to the conditions of Praburam and Goree's "great void mode," the ion drag force was calculated to be negligibly small in this system, and the void's volume was maintained instead by an outward thermophoretic force.[53] (Figure 2 in the original publication.)

In 2002, Dahiya et. al. published a study on dust voids in 2-dimensional dust monolayers. The researchers observed the void region to grow both with increasing rf power and with increasing neutral pressure. Based on calculations of the electrostatic potential energy of the system, they concluded that the dust void could be accounted for physically as a result of the dust Yukawa potential, which determines the optimal inter-particle distance of the dust grains, as well as the total volume occupied by the particles.[57] An image of their dust void, as well as a plot of the dust void diameter as a function of both the neutral pressure and rf power, can be seen in Fig. (2-3).

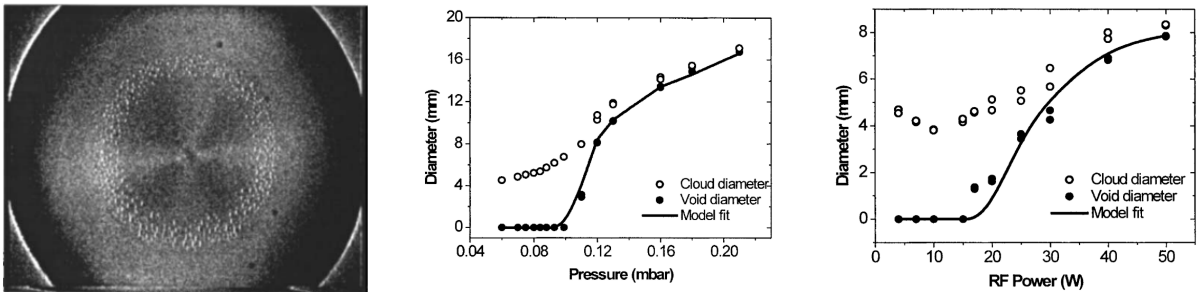

Figure 2-3: A self-induced dust void formed in a 2-dimensional dust monolayer. The void's diameter was observed to increase as a function both of neutral pressure and of rf power. The researchers calculated the void to be a result of the dust Yukawa potential.[57] (Figures 2(b) – 4 in the original publication.)

While all formed within differing geometries and under different experimental conditions, all of the dust voids observed as late as 2002 had shared the common trait of being "self-induced." That is, they formed as a result of internal plasma processes, and the void region contained only dust-free plasma and a population of neutral atoms. In 2004, void studies were published by Klindworth et. al.[58] and Thomas et. al.[59] in which the dust void was created via the introduction of an electrically biased probe tip into the dusty plasma. This allowed researchers to directly measure the response of the dust void as the probe bias was changed.

Klindworth et. al. reported the formation of a dust void under microgravity conditions within the Plasma Kristall Experiment (PKE) during a parabolic flight microgravity campaign. When a Langmuir probe was introduced to the dust plasma environment for diagnostic purposes, the dust

grains were seen to form a shell structure around the probe tip. The researchers noted that the probe was biased negatively relative to the surrounding plasma potential and was collecting a positive ion current while maintaining the surrounding dust void. It was concluded that this void was created, as with that of Praburam and Goree[51], by an equilibrium of the ion drag force and the electrostatic force on the dust grains.[58] This dust void notably differed from Praburam and Goree's self-induced void in that the predominant forces were now in the opposite directions; the ion drag force directed inward, while the electric force on the negatively-charged dust grains was outward (due to the probe being biased negatively relative to the plasma potential). While a direct comparison of the void's size to the probe's bias potential was not recorded, researchers noted that it was necessary to keep the probe bias lower than the plasma potential to avoid contamination of the probe tip by dust deposition. A photograph, as well as a schematic diagram, of this probe-induced dust void can be seen in Fig. (2-4).

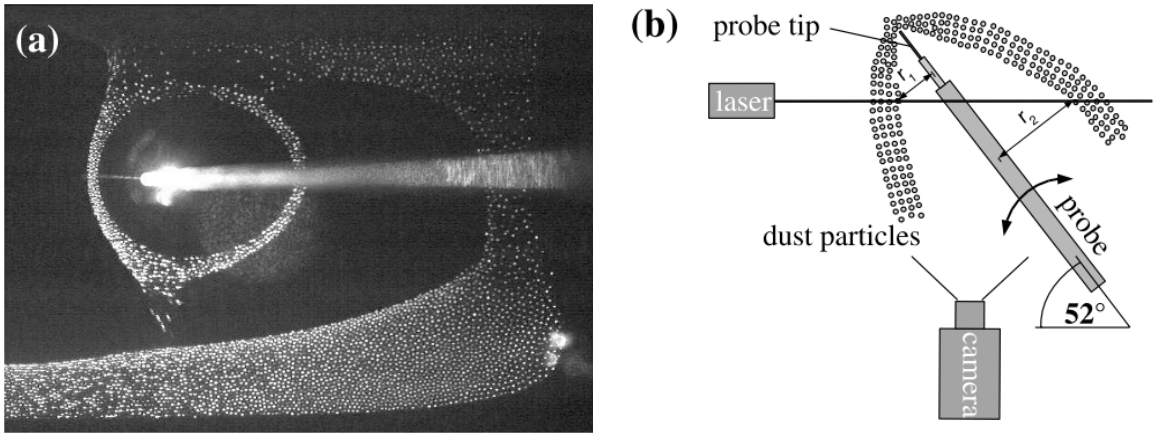

Figure 2-4: A probe-induced dust void formed under microgravity conditions. As opposed to previously reported "self-induced" voids, this void was maintained by an outward electrostatic repulsion of the dust grains, opposed by an inward drag force as ions were collected by the probe tip.[58] (Figures 2 (a) and (b) in the original publication.)

Also in 2004, Thomas et. al. published a similar result from a ground-based experiment in which a Langmuir probe was inserted into a 3-dimensional dust cloud within a plasma with the

explicit goal of forming a dust void. The void was photographed over a range of probe bias potentials and was observed to decrease in size as the probe approached the surrounding plasma potential. The researchers not only described the void as a result of opposed ion drag and electrostatic forces on the dust grains, but also developed and presented a physical model to account for the dependence of void size on probe voltage (see Sec. #-#). The difference between ion-collecting and ion-source voids was explicitly noted in this publication: "It is important to note that in the voids generated by a negatively biased probe described here, the roles of the electric and ion drag forces are reversed compared to voids formed under microgravity conditions."[59] (Quote found on page 1 in the original publication.) An example of a dust void from this investigation and the relation of void radius to probe voltage can be seen in Figure 2-5.

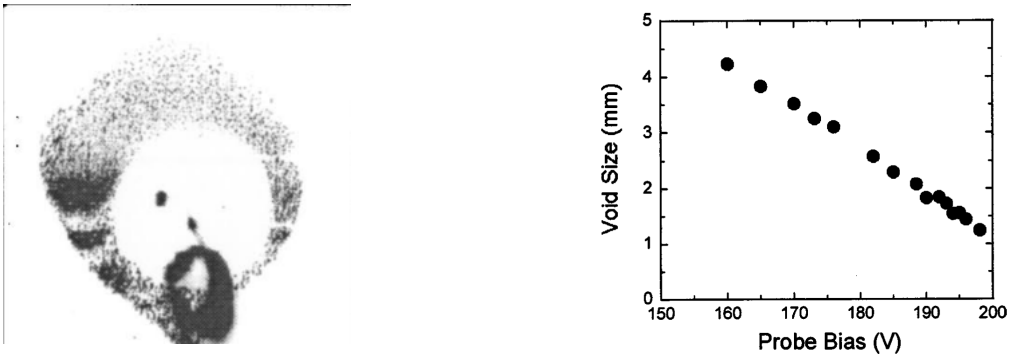

Figure 2-5: A probe-induced dust void formed in a 3-dimensional dust cloud. The relation of the radius of the void to the bias of the probe was measured and showed that the void decreased in size as the bias became more positive. The void collapsed entirely when the probe bias reached the plasma potential. The researchers also developed a physical model to explain the dependence of the void's size on the probe bias. (Figures 1 (c) and 4 in the original publication.)

One further example of a probe-induced dust void experiment, and one particularly similar to the experiments presented here, was that of Bailung et. al. in 2018.[60] Following up on several years of investigations of probe-induced dust voids, the researchers created a 2-dimensional monolayer of dust grains in an rf discharge plasma, and created circular dust voids within this monolayer

using a vertically oriented Langmuir probe. As in previous probe-induced dust voids, the void was seen to contract as the probe bias approached the plasma potential. A sample dust void from this experiment as well as a plot of the relationship between probe voltage and void radius is shown in Figure 2-6.

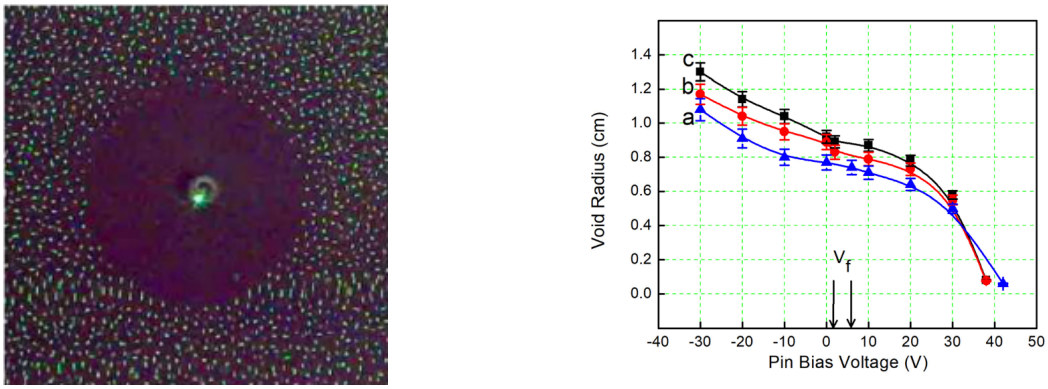

Figure 2-6: Probe-induced dust void created in a 2-dimensional dust monolayer.[60] As in previous investigations of probe-induced voids, these voids were maintained by an outward electrostatic force, opposed by an inward drag force as ions are collected by the probe tip. Just as was noted by Klindworth et. al. and Thomas et. al., the dust void fully collapsed when the probe tip was biased to the plasma potential.[58,59] (Figures 1 (b) and 3 in the original publication.)

The common trait of the dust voids reported across these (and other) investigations is that they are maintained by an equilibrium of opposing forces. A defining characteristic of most self-induced voids is that they are driven by a drag force created by an outward stream of ions, from a central ion source (usually due to rf ionization in the center of the plasma bulk). In every investigation published to-date of probe-induced voids, however, the ion drag force is oriented inwards as ions are collected by the probe tip which is biased negatively relative to the plasma potential.

This categorization of dust voids can be generalized into ion-source and ion-collecting voids. Because these two categories of dust voids require ion streams in opposite directions, most experiments fall squarely into one of the two varieties and are incapable of creating a dust void of

the opposite category using the same experimental configuration. As will be shown in Chapters 3 and 4, the apparatus used for the experiments described in this work is uniquely suited to creating both ion-source and ion-collecting dust voids. Further, this configuration is capable of transitioning from one category to the other without the dust void collapsing or dissipating. This novel configuration offers unique insights into the nature of dust voids and ion flows within a plasma system, both with and without an externally applied magnetic field.

2. Dust Void Theory

A theoretical model for probe-induced voids in the absence of external magnetic fields was been developed by Avinash, et al.[59] The goal of this model is to determine the dependence of a dust void radius on the probe voltage. Because this model provides the critical framework for interpreting the experimental results presented in this work, a detailed description of this model is presented here.

First, consider negatively charged dust grains that are suspended in a background plasma. The system will for now be considered in one dimension (r), with the probe located at $r = 0$ and biased at Φ_P and the void boundary located at $r = r_0$.

As stated above, a dust void is formed by a balance of two primary forces on the dust grains: the Coulomb (electrostatic) force F_E and the ion drag force F_D. In the case of a probe-induced void, the void boundary exists at the location r_0 where $F_E = F_D$. Inside the void region $(r < r_0)$ the Coulomb force exceeds the ion drag force, $F_E > F_D$, therefore the dust grains are expelled out beyond the void boundary. A visualization of this force balance is shown in Fig. (2-9).

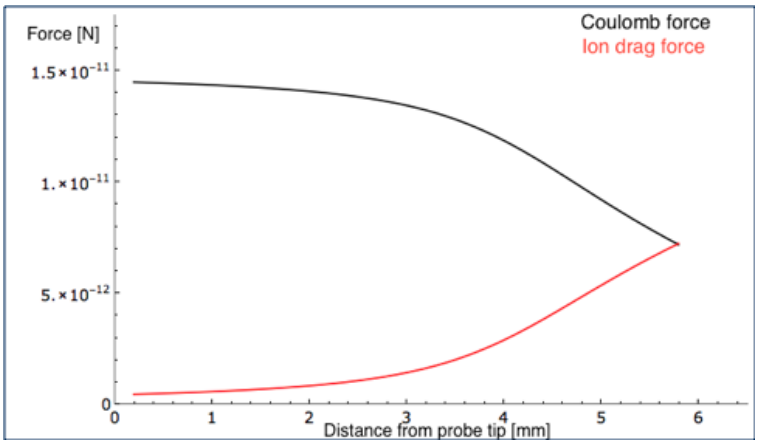

Figure 2-7: An illustration of the balance between the outward Coulomb repulsion force and the inward ion drag force on a dust grain, as functions of distance from the center of the void structure (in this case, an electrically biased probe tip). For clarity only the magnitudes of the forces are represented here, but it should be noted that their directions are opposed to one another. The equilibrium point occurs when the two forces

are equal, which is the location at which the void border is formed. Grains outside this radius will experience a net force inwards toward the void, and grains inside this radius will be expelled outwards.

The Coulomb force is given by $\overrightarrow{F_E} = Q_D\vec{E}$, where $\vec{E}$ is the radial electric field due to the probe. For the probe bias Φ_P being negative relative to the plasma space potential V_S, this electric field is directed inward toward the probe. For $Q_D < 0$, which is typical in a dusty plasma, due to the higher electron mobility, the resultant Coulomb force $\overrightarrow{F_E}$ on the dust grains is therefore directed outwards, with the negatively charged dust being drawn away from the probe and towards the more positive surrounding plasma.

To estimate the ion drag force, the ions are assumed to be mobility limited, so that the ion flow velocity is expressed as

$$u_i = \mu_i E \tag{2-1}$$

with the ion mobility $\mu_i = e/m_i\nu_{i,n}$ where $\nu_{i,n}$ is the ion-neutral collision frequency $\left(\nu_{i,n} = N\sigma_{i,n}v_{T,i}\right)$, N is the background neutral density, $v_{T,i}$ the ion thermal velocity, and $\sigma_{i,n}$ the ion-neutral collision cross-section.

Applying the continuity equation for the ions:

$$\frac{\partial}{\partial r}(n_i u_i) = 0 \tag{2-2}$$

we can equate the ion conditions at an arbitrary point within the dust void to the conditions at the void boundary:

$$n_i u_i = n_{i0}u_{i0} = constant \tag{2-3}$$

and in fact this constant can be measured:

$$n_i u_i = n_{i0}u_{i0} = {}^{I}/_{eA_P} \tag{2-4}$$

with I being the current collected by the probe and A_P the probe's collection area.

Applying the Poisson equation for the region within the void:

$$\frac{d^2}{dr^2}\varphi(r) = -{}^{e}/_{\varepsilon_0}\,(n_i - n_e - Z_D n_D) \tag{2-5}$$

noting that within the dust void $n_D = 0$ and that the electrons are taken to be in Boltzmann equilibrium:

$$\frac{d^2}{dr^2}\varphi(r) = -{}^{e}/_{\varepsilon_0}\,(n_i - n_e) \tag{2-6}$$

$$n_e = n_{e0} e^{{}^{e\varphi(r)}/_{kT_e}} \tag{2-7}$$

Expressing the electric field $\vec{E} = -|E|\hat{r} = -\left|\frac{d}{dr}\varphi(r)\right|\hat{r}$ and denoting the electric field at the void edge as $E(r_0) = E_0$, we combine Eqs. (2-1) and (2-4), yielding

$$\frac{n_i}{n_{i0}} = \frac{E_0}{|\varphi'(r)|} \tag{2-8}$$

Substituting Eqs. (2-6) and (2-7) into (2-8), we obtain the principal differential equation for the potential within the void:

$$\varphi''(r) + \frac{e n_{i0}}{\varepsilon_0}\left(\frac{E_0}{|\varphi'(r)|} - \frac{n_{e0}}{n_{io}} e^{{}^{e\varphi(r)}/_{kT_e}}\right) = 0 \tag{2-9}$$

Eq. (2-9) can be solved numerically in order to obtain the dependence of the radial dimension of the void edge r_o on the potential V_b of the probe.

An evaluation of Eq. (2-9) is shown in Fig. (2-8). Here, a typical plot of the solution for the normalized potential in the void. For this calculation, it is assumed that the equilibrium plasma density $n_0 = 3.0 \times 10^{15}\ m^{-3}$, an electron temperature $T_e = 2.7\ eV$, a space potential $V_s = 40\ V$,

and a neutral pressure $P = 95\ mTorr$. The x-axis shows the distance from a probe edge in mm. The y-axis shows the potential difference between the probe, V_b, and the space potential, V_s, normalized to the electron temperature.

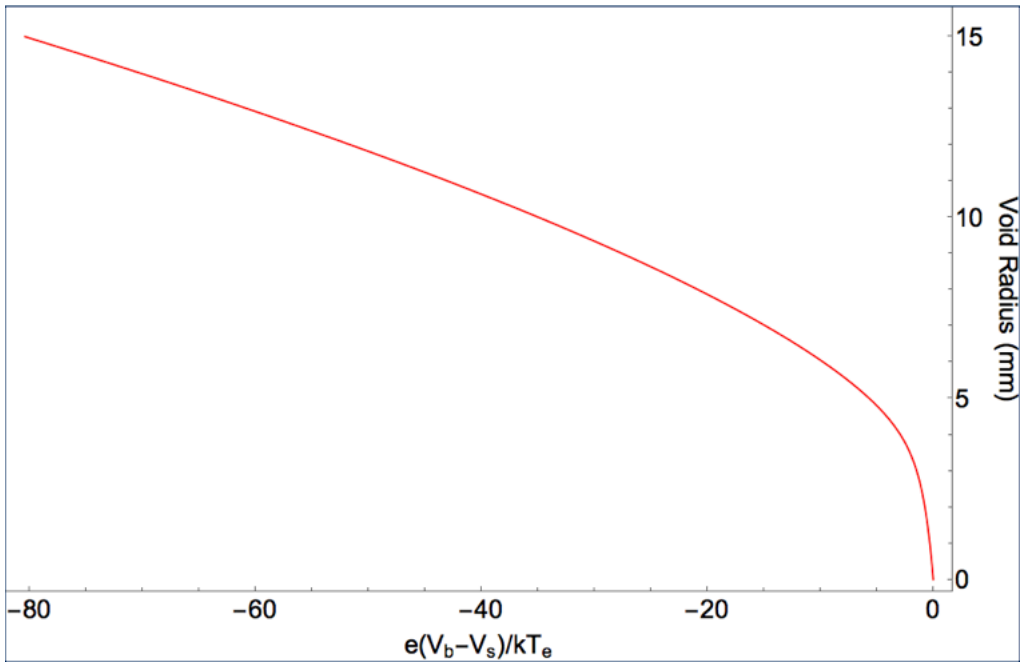

Figure 2-8: Eq. (2-9) expressed as the distance in mm from the probe tip at the center of the void structure to the equilibrium point at the edge, expressed in terms of the probe bias potential as compared to the bulk plasma space potential, normalized to the electron temperature. As observed experimentally, the general linearity and sudden collapse as the bias potential approaches the space potential is evident.

3. Magnetic Field Effect on Dust Grain Charge

A topic of much recent discussion in the dusty plasma community is the range and extent of effects of an applied external field on a dusty plasma system, and specifically the influence on the dust grains themselves.[61,62] There are direct effects to consider, such as the influence of the magnetic field on the trajectories of the charged dust grains. There are also indirect effects due to modification of the background plasma conditions. Because the ions and electrons have charge-to-mass ratios several orders of magnitude larger than that of the dust grains, their properties can be dramatically affected by even a relatively small magnetic field. This can significantly impact the dynamics of the interactions between these background species and the dust grains.

Electrons, for instance, can become strongly magnetized even at low magnetic fields. If the electron Larmor radius is small enough to be on the order of a single dust grain's diameter, dust grains may no longer collect as many charges as in non-magnetized cases, and this can decrease the average dust charge.

Of particular interest in this study is whether and how much the electric charge of the dust grains is altered in an environment with an external magnetic field. Because the dust particles acquire their charge via ion- and electron-currents from the surrounding plasma a small magnetic field that modifies the charging currents may result in significant changes to the dust charge and, by extension, the dynamics of the dust grains within the plasma.

In dusty plasma experiments performed in devices capable of creating steady state magnetic fields, observations have consistently suggested that at high magnetic fields, the maximum steady state dust charge is decreased, sometimes dramatically so.[14,63] At the magnetic field strengths used in the experiments described here, the dust charge is unlikely to vary by a significant percentage of its baseline charge. Even at these fields though, a very small change in the net electric charge

of the grains would need to be taken into consideration and accounted for in the analysis of these experimental results.

In simple terms, the charging effects mentioned above could be caused by two basic changes to the dust charging process: the decrease in magnitude of the electron current to the dust grain surface I_e, or the increase in that of the ion current I_i. Because the ions will not become strongly magnetized at the pressures and magnetic fields in 3DPX ($H_{i,max}$~0.84), we will instead focus on the electrons ($H_{e,max} \approx 82$).

At a typical operational configuration in 3DPX, the peak magnetic field may be approximately 800 Gauss (80 mT), and the neutral pressure approximately 100 mTorr (13.3 Pa). At these parameters, the electrons will have a Larmor radius $r_{L,e} = 8.16\ \mu m$, a mean free path between collisions with neutral atoms of $\lambda_{mfp,e-n} = 2.73\ mm$, and a Hall parameter $H_e = 33.08$. The dust grains primarily used in 3DPX have a radius $a = 4.0\ \mu m$, less than the electron Larmor radius. The combination of the electrons' high level of magnetization (averaging ~5.3 full gyro-orbits per collision with a neutral atom) and small Larmor radius on the order of the dust grain radius means that an individual dust grain is very unlikely to be able to collect electrons from further than a few electron Larmor radii away perpendicular to the magnetic field.

As such, experimental attention will be paid to potential changes in the dust charge as the field is increased. Because the radius of the dust void is dependent on the dust charge, this experiment will provide a novel method of investigating the charge of a dust grain with regards to a changing magnetic field.

Chapter 3 - Experimental Design

1. Vacuum Vessel

The experiments described were performed in the Three-Dimensional Dusty Plasma Experiment (3DPX) vacuum. The 3DPX chamber has been used for a variety of dusty plasma experiments over the last 15 years - particularly for the study of the thermodynamic properties of dust particles in dc glow discharge plasmas as reported in papers by Thomas, et al,[64] Williams, et al,[33,65] and Fisher, et al.[66] The 3DPX chamber was also used as a preliminary test chamber for dust deflection studies in the work by Lynch, et al.[63] While the 3DPX vacuum chamber has been described in detail in previous works,[64,66,67] it has been modified for use in the work reported here. This section will provide an overview of the experimental configuration used for these studies.

The vacuum vessel is a custom-manufactured six-way cross made of stainless steel, approximately 17 inches (~43 cm) in length and with an interior volume that is nominally cylindrical, with an inner diameter of approximately 4 inches (~10 cm). One side of the vessel is fitted with a large (10 inches by 3 inches, or approximately 25 cm by 8 cm) glass window. In the configuration used throughout the experiments described here, this chamber was mounted on a frame of aluminum extrusion, with this large window aligned on the side to allow optical access to the experimental volume. A schematic drawing of the 3DPX vacuum vessel design is shown in Fig. 3-1.

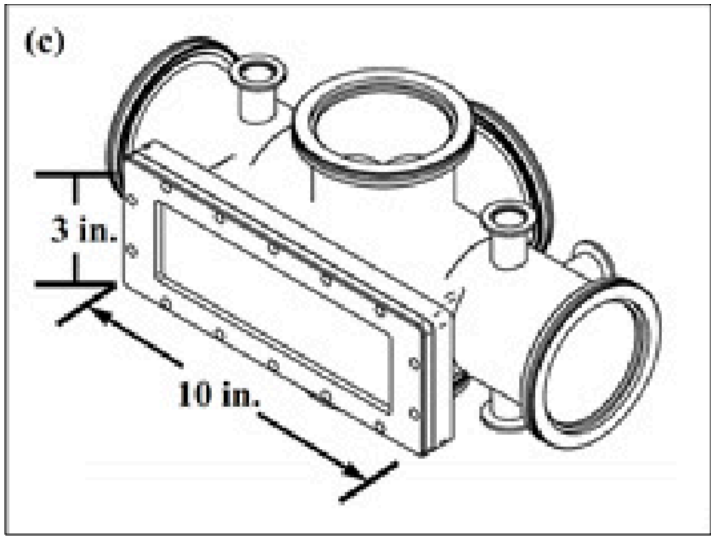

Figure 3-1: Schematic drawing the 3DPX vacuum vessel. This custom-designed chamber has been used in several previous dusty plasma experiments and is of particular use due to its wide area viewing port and large number of access ports. The primary experiments described in this work were carried out in the 3DPX vacuum chamber.

In the arrangement used for these experiments, the top and bottom of the vessel (as well as the side opposite the large window) are standard ISO-100 vacuum ports. The port opposite the window was attached to a pump (see gas flow section) to bring the interior pressure of the chamber down to pressures well below 10 mTorr (1.3 Pa). The bottom port was used to insert the plasma generation and void systems (see plasma generation and void creation section). The top port was connected to a stainless steel ISO-100 three-way "T-junction" with one port oriented upwards and fitted with an ISO-100 glass viewport (see optics section) and the frontward-facing port was fitted to the dust shaker via a QF-40 adaptor (see dust section). The ports on the long ends of the primary chamber were fitted either with permanent magnets on QF-40 quick-connect couplings or, in the case on non-magnetized ($B = 0$) experiments, with stainless steel ISO-100 blanks. Photographs of the 3DPX device in the configuration used for this experiment are shown in Fig. 3-2.

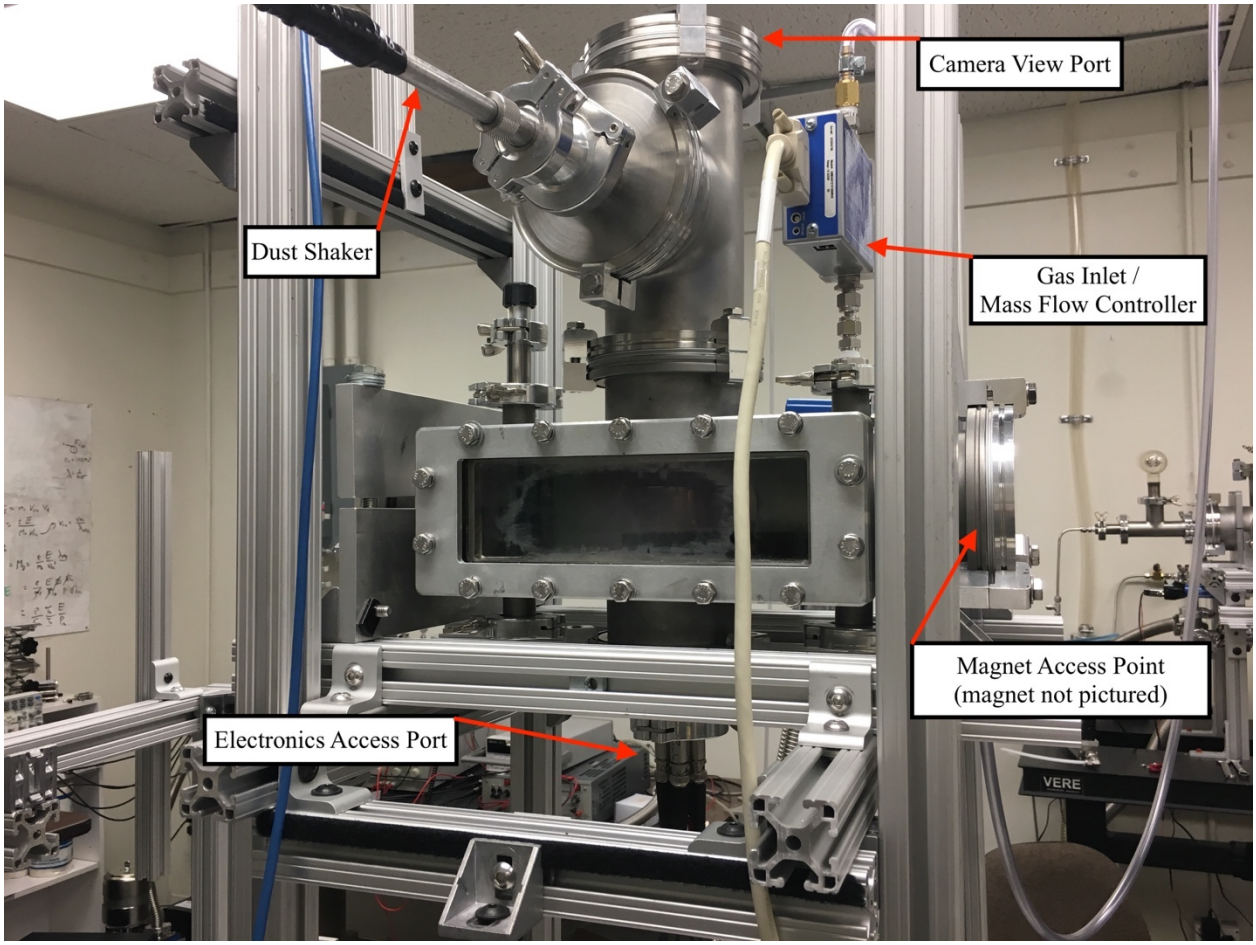

Figure 3-2: Annotated view of the 3DPX vacuum vessel as configured for the experiments described in this work. The camera is mounted out of frame, directly above the camera view port. While not attached in this photo, the permanent magnets were attached through the magnet access points on opposite sides of the chamber. The laser and optical configuration were mounted facing the large front-facing window. The roughing pump is not visible in this photo but is attached via an ISO-100 port directly opposite the large rectangular window (on the far side of the chamber in this photo). The rf-power, as well as the electrical connections to the probe tip and the tray, go upwards through a 4-port BNC feedthrough attached to the electronics access port on the bottom of the chamber.

2. Gas Flow

Argon gas flow into the vacuum vessel was maintained using a MKS 1179 series mass flow controller. This allowed a range of gas flow from 0 to 10 standard cubic centimeters per minute (sccm), and was controlled by a MKS type 246 benchtop power supply. Neutral pressure was monitored using a Kurt J. Lesker 275i series pressure gauge, attached to the chamber via a KF-16 vacuum port on the top side of the chamber. In conjunction with the roughing pump, this configuration allowed neutral pressures to be dialed in from ~10 mTorr to ~225 mTorr.

3. Plasma Generation and Void Creation

The plasmas generated in this experiment were primarily capacitively-coupled radio frequency (rf) plasmas. Plasmas were generated inside a cylindrical glass tube with an outer diameter of 2.5 inches (6.4 cm), an inner diameter of $2\frac{1}{8}$ inches (5.4 cm), and a height of approximately $2\frac{1}{4}$ inches (5.7 cm). A photograph of this arrangement is shown in Fig. (3-3).

This glass tube allowed for optical access from outside of the experimental volume, while also helping to confine the plasma and dust grains within the region of investigation. The glass cylinder was set on a square electrode of thin aluminum, 3 inches on a side (7.6 cm). This aluminum electrode was connected through a 4-port BNC vacuum feedthrough plate through the bottom ISO-100 port of the vacuum vessel.

The inside surfaces of the glass cylinder were lined with strips of copper conducting tape, 1.5 inches wide (3.8 cm) and roughly 1.5 inches long (3.8 cm). Two strips were placed on opposite surfaces of the cylinder and connected through two ports of the 4-way BNC vacuum feedthrough. In most experiments described here, both strips were connected to an RF-VII Model 3 rf-generator that provides power to the plasma at a fixed frequency of 13.56 MHz at power levels up to 100 W. Most of the experiments described here were performed at power levels of 20 W. The rf generator

is connected to the electrodes via an RF-VII ATN-20/30 auto-matching network. The addition of the rf plasma generation is a new capability for the 3DPX system and was specifically added to carry out these studies.

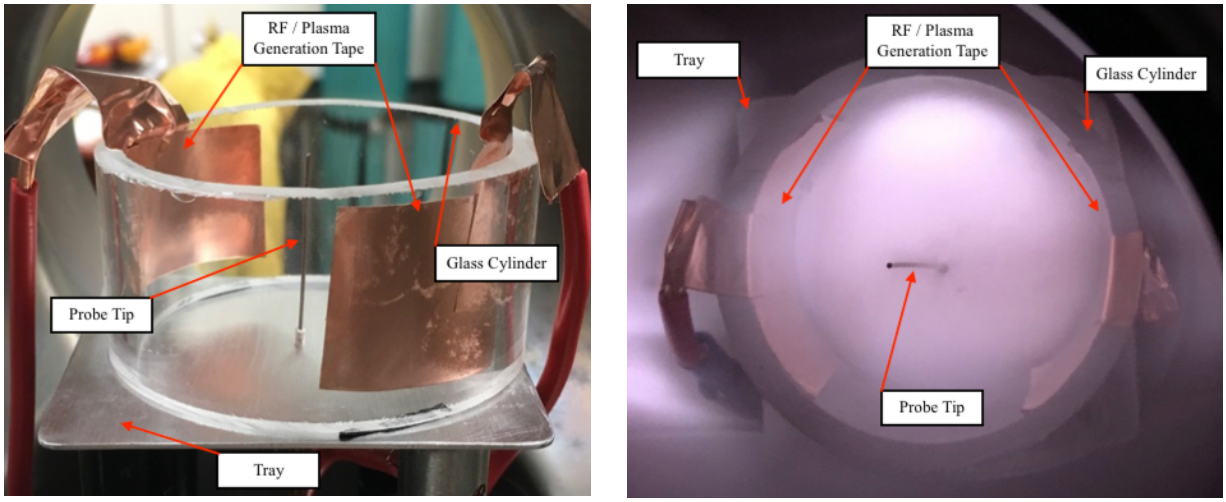

Figure 3-3: The plasma creation and confinement system, and the probe tip used to create dust voids within the 3DPX vacuum vessel. The conducting copper tape strips served as opposing rf electrodes. The probe tip was isolated from the tray by a thin ceramic tube. The tray was electrically grounded to the chamber. The glass cylinder both served to hold the conducting tape strips in place, as well as to confine both the plasma and the dust grains.

The center of the square aluminum electrode contained a small hole through which a Tungsten wire with a diameter of 0.025 inches (635 μm) was inserted, electrically isolated from the electrode by a thin ceramic tube. Because the different operational modes for this probe tip required dramatically different sizes, a different length of wire was used for dust void creation than was used for Langmuir probe measurements.

This length of wire served as the Langmuir probe tip which would act both to drive the void structures, and as one of the central diagnostic methods for characterizing the plasma environment. (Results from this diagnostic can be found in Ch. 4. When used for creating dust voids, the wire extended ~1.5 inches (3.8 cm) upwards from the surface of the aluminum electrode. When used to

measure current as a Langmuir probe, the tip was merely 3.23 mm long (see Ch. 4). The probe tip was connected through the final port of the 4-way BNC feedthrough.

4. Langmuir Probe

One of the earliest diagnostic methods for characterizing plasmas in a laboratory environment, and to this day perhaps the simplest, is the use of a single-tipped Langmuir probe. First described by Irving Langmuir nearly a century ago,[3] the Langmuir probe can be used to extract several parameters about a plasma, notably the electron temperature, space potential, floating potential, and electron density.[68]

While there have been many advancements in the engineering, implementation, data collection, and data analysis methods involved, the essential components of Langmuir probes are unchanged from their earliest days: a conducting surface of some shape (often a cylindrical length of wire or a flat disc-shaped surface) is inserted into the bulk of a plasma, electrically isolated from the vacuum vessel in which the plasma is contained, and the current collected by the surface is recorded as a function of a bias voltage applied to the probe relative to ground (referenced to the vacuum vessel). The resulting current-voltage curve can then be used to ascertain diagnostic information about the plasma.[69]

Typical Langmuir probe analysis relies on the assumption that the plasma is quasi-neutral, which is to say that the sum of positive and negative charges over a characteristic length of the plasma is neutral:

$$\sum q = q_i n_i - e n_e = 0 \tag{3-1}$$

or, for singly-ionized species:

$$\sum q = e n_i - e n_e = 0 \tag{3-2}$$

$$n_i = n_e \tag{3-3}$$

It is also taken as a prior assumption that the ions and electrons are at thermal equilibrium and can be described by a Maxwell-Boltzmann energy distribution with ion temperature T_i and electron temperature T_e. In ordinary laboratory "low temperature" plasma experiments, the ions are safely assumed to be room temperature, or $T_i = {}^{1}/_{40}\ eV$, and the electron temperature is usually a few to several eV.

The analysis of the current to the probe begins with separating the total current to the probe into the contribution of the collected ions (taken to be positive current) and electrons (taken to be negative).

$$I = I_i + I_e \tag{3-4}$$

When the probe is held to a bias potential that is highly negative with respect to the surrounding plasma potential ($V_b \ll V_p$), the electron current I_e goes to zero as the electrons are repelled from the probe, and the current collected is a constant value known as the ion-saturation current. For a plasma with similar ion and electron currents, this current can be expressed as

$$I_{i,sat} = 0.6en_i\sqrt{\frac{kT_e}{m_i}}A_{probe} \tag{3-5}$$

where A_{probe} is the surface area of the probe's collecting surface. As the bias potential is increased, the ion current drops off exponentially:

$$I_i = I_{i,sat}e^{\frac{e(V_p - V_b)}{kT_i}} \tag{3-6}$$

If the probe is instead held to a very high potential relative to the plasma potential, the ions will be repelled and instead the probe will collect an electron-saturation current, express as:

$$I_{e,sat} = \frac{1}{4} e n_e v_{e,th} A_{probe} \tag{3-7}$$

where $v_{e,th}$ is the electron thermal velocity:

$$v_{e,th} = \sqrt{\frac{8kT_e}{\pi m_e}} \tag{3-8}$$

Eqs. (3-7) and (3-8) can be rearranged to solve for the electron temperature:

$$kT_e = \left(\frac{I_{e,sat}}{e n_e A_{probe}} \right)^2 (2\pi m_e) \tag{3-9}$$

Just as the ion current, the electron current will drop off exponentially away from electron-saturation:

$$I_e = I_{e,sat} e^{\frac{-e(V_p - V_b)}{kT_e}} \tag{3-10}$$

At a certain bias potential, the number of ions and electrons collected by the probe will be even ($I_i = I_e$), and (for singly-ionized ions), the collected current will go to 0. This is known as the floating potential, the electric potential at which a conductive body will "float" when fully surrounded by a plasma. In low temperature plasmas, this will occur when the ion current is still in ion saturation, so we may substitute Eq. (3-10) into (Eq. 3-4) at the floating potential, yielding:

$$I_{e,sat} e^{\frac{-e(V_p - V_b)}{kT_e}} = I_{i,sat} \tag{3-11}$$

and, using Eq. (3-5), we may solve for the plasma potential:

$$V_p = V_f - \left(\frac{kT_e}{e} \right) \ln \left(0.6 \sqrt{\frac{2\pi m_e}{m_i}} \right) \tag{3-12}$$

Thus, a Langmuir probe, while a comparatively very simple device, can be used to acquire a great deal of information about a plasma with relatively little effort.

5. Dust Grains

The dust used in this experiment is comprised of $4.0 \pm 0.4\ \mu m$ radius silica particles. The particles are nominally spherical and have a mass density of 2100 $^{kg}/_{m^3}$, giving each grain a nominal mass of 5.63×10^{-13} kg. The grains were purchased from Fiber Optic Center Inc. They are introduced into the plasma system via a cylindrical dust shaker mounted on a QF-25 quick-connect coupling directly above the plasma generation area. By lightly tapping the end of the shaker outside of the vacuum vessel, a small number of particles are released and fall straight down. While a majority of grains dropped from a single shake will fail to accumulate sufficient charge to levitate and land on the tray, many will begin floating immediately, forming the layer of dust used in the experiment.

The dust which accumulates sufficient charge will levitate above the tray indefinitely, supported against gravity by an electrostatic force created by the sheath electric field that is formed between the electrically grounded tray and the surrounding plasma. The electric field will point from the plasma to the tray, providing an upward force on the negatively charged dust grains that can balance the gravitational force on the grains. The magnitude of this electric field can be estimated by using the dust grain mass value above and estimating an average charge of ~20,000 electron charges. (This charge value is obtained from the dust grain charging model presented in Ch. 1.) Setting the electric and gravitational forces even to one another:

$$m_d g = Q_d E \tag{3-13}$$

$$E = \frac{m_d g}{Q_d} \tag{3-14}$$

This suggests a vertical electric field of ~1725 $^{\mathrm{V}}/_{\mathrm{m}}$, or ~17.25 $^{\mathrm{V}}/_{\mathrm{cm}}$.

6. Creation and Mapping of the Magnetic Field

The background magnetic field within the plasma chamber was created via a pair of powerful permanent rare earth ring magnets. Each of these magnets was 2" long, with a 2" OD and a $^1/_4$" ID. The bulk material of the magnets was a neodymium, iron boron composite $Nd_2Fe_{14}B$. These magnets were installed within the vacuum area through QF-40 quick-connect couplings attached to the ISO-100 ports on the far ends of the vacuum chamber. This allowed a large range of axial motion for each magnet without breaking vacuum, so that the magnetic field configuration of the experiment could be changed quickly several times within a single experimental session. The magnets were oriented so that the north poles were pointed in the same direction, to combine for an axial field in the center of the chamber. One permanent magnet is shown in Figure 3-4.

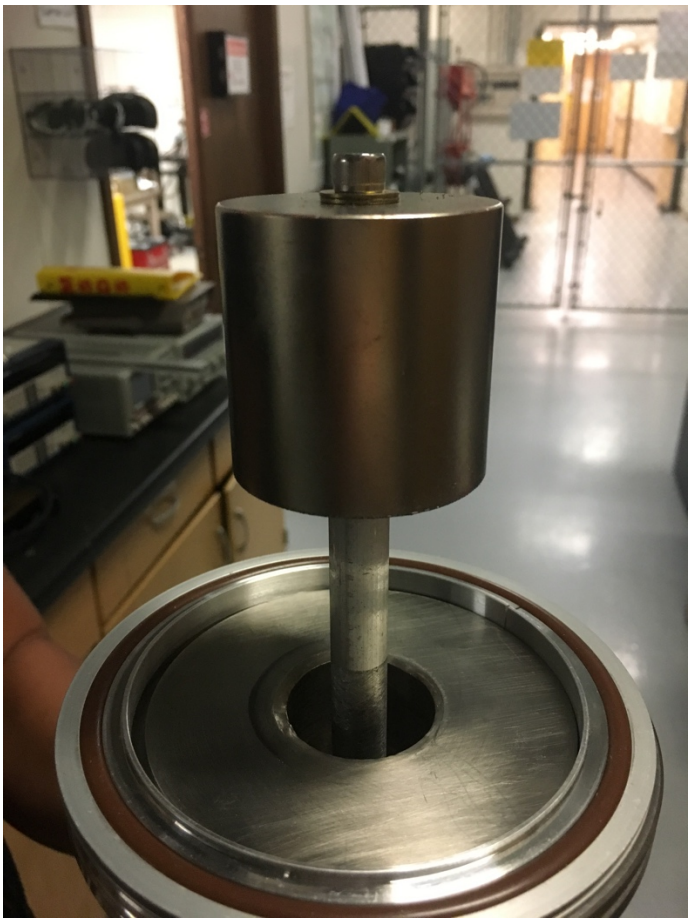

Figure 3-4: One of two permanent magnets used for the creation of the axial magnetic field in the 3DPX vacuum chamber. The magnet is secured to a ½" rod, which is mounted to the chamber through a QF-40 quick-connect coupling. This coupling is attached with an adaptor to the ISO-100 port on the end of the chamber and allows for easy linear movement of the magnets while still holding them in place without breaking the vacuum of the chamber.

With the magnets installed on the vacuum chamber, a 3-axis gaussmeter was mounted at the axial and radial center of the chamber to measure the magnetic field at that location across a range of separation distances for the permanent magnets. To obtain a precise map of the magnetic field not only at the center, but at all locations across the width of the plasma region of interest (~5 cm), measurements were made not only with the magnets arranged equal distances from the gaussmeter detector, but also offset by as much as 2.5 cm in each direction.

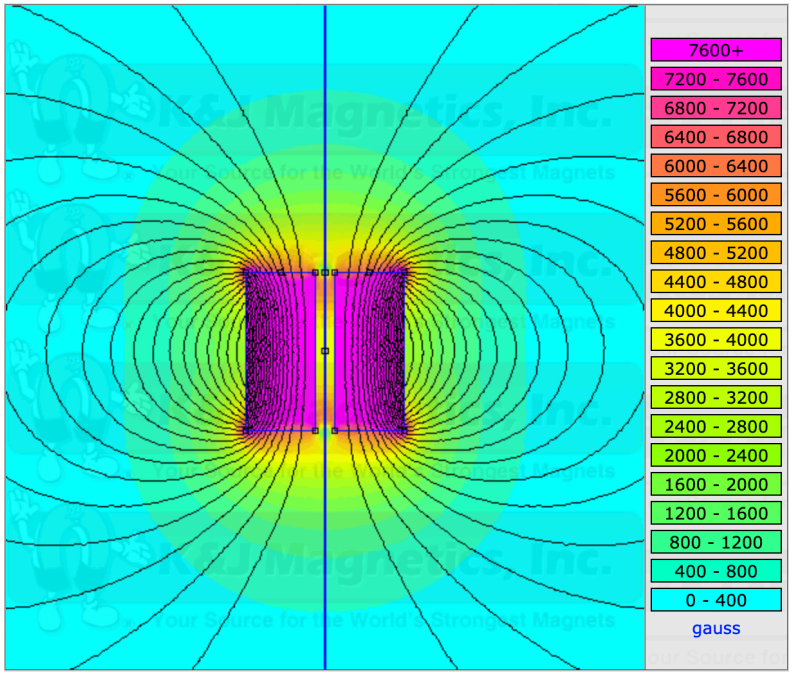

Figure 3-5: Magnetic field map of a single permanent magnet, courtesy of the manufacturer, K&J Magnetics.

The magnetic field was measured to be dominated by the axial component B_z, with the magnitudes of the B_x and B_y components generally being less than 10% (and often less than 5%) that of B_z. With the magnets held at any particular separation distance, the field B_z was measured to be very close to parabolic in relation to axial distance, or $B_z \propto z^2$, with the maximum values at the surfaces of the permanent magnets and the minimum value very near to the center of the chamber. Linear regression analysis was applied to the B_z measurements made at each value for magnet separation distance d, assuming a solution in the form of a 2nd order polynomial, or:

$$B(z) = k_2 z^2 + k_1 z + k_0 \tag{3-15}$$

where k_n refers to the n^{th} order coefficient. For all values of magnet separation distance d, the linear regression analysis yielded a solution in strong agreement with the magnetic field measurements.

With a sufficient sample of magnetic field measurements at varying magnet separation distances and their associated 2nd order polynomial solutions, the coefficients of those polynomial solutions k_n can be compiled and assessed. These k_n coefficients were fit to an exponential solution of the form:

$$k_n(d) = A_n e^{-b_n d} \tag{3-16}$$

The axial magnetic field at any particular distance along the chamber, for any particular magnet separation distance, can now be easily calculated:

$$B(z,d) = (A_2 e^{-b_2 d})z^2 + (A_1 e^{-b_1 d})z + (A_0 e^{-b_0 d}) \tag{3-17}$$

$A_2 = 759.96 \pm 52.00\ T$	$b_2 = 25.839 \pm 0.616\ m^{-1}$
$A_1 = -7.5896 \pm 1.8600\ T$	$b_1 = 34.884 \pm 2.170\ m^{-1}$
$A_0 = 0.31407 \pm 0.00700\ T$	$b_0 = 16.404 \pm 0.223\ m^{-1}$

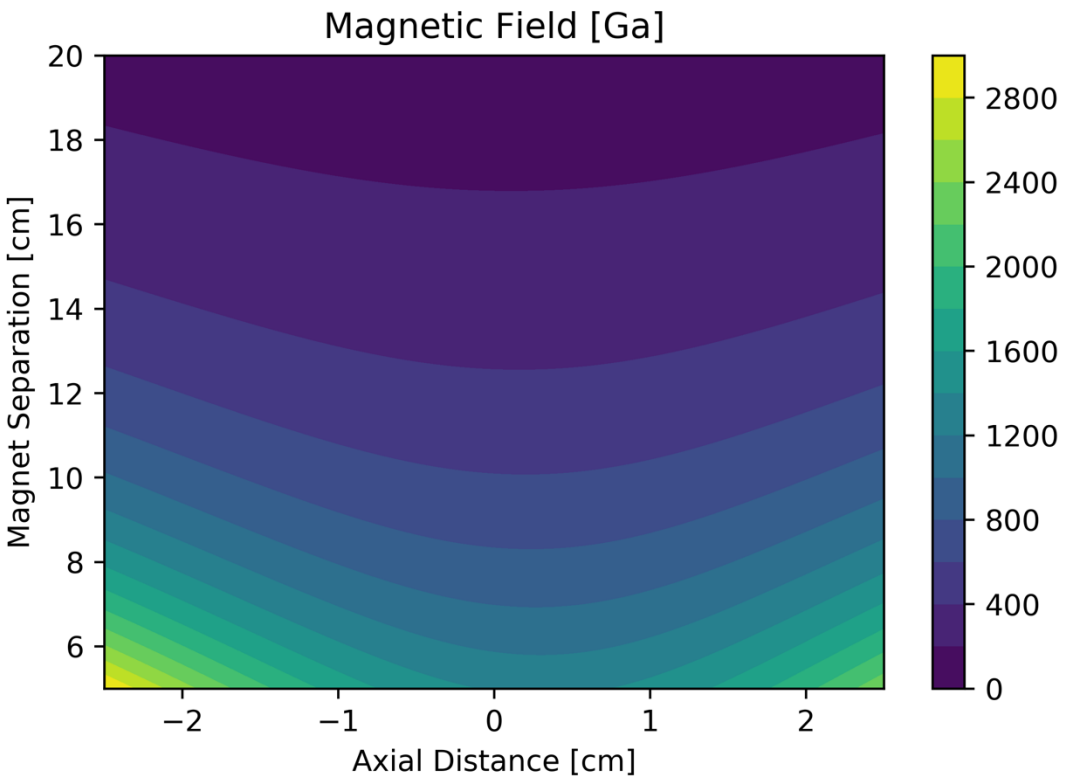

Figure 3-6: Visualization of the magnetic field strength, in Gauss, on the center axis of the 3DPX chamber, as a function of separation between the permanent magnets and distance from the midpoint between the magnets.

Chapter 4 - Results and Analysis

In this chapter, the results of the experiments will be presented. First, the initial observations will be described, along with preliminary speculation as to their significance. Next, an explanation will be provided of the various methods of processing raw data (primarily in the form of videos) into a more useful, quantifiable form. This will then be interpreted in context of various current relevant theories of dusty plasmas and dust voids, particularly the Avinash model of dust voids. In scenarios in which the experimental results differ from accepted theory, or in which the experimental parameters exist outside the regime of the theory, variations on the existing theory will be suggested and justified physically.

1. Langmuir Probe Results – Plasma Characterization

As described in Ch. 2, a Langmuir probe is a simplistic yet reliable method of characterizing a plasma environment. The plasmas used in the dust void experiments within the 3PDX chamber were scanned with a single-tipped Langmuir probe to gain insight into the background conditions in which the dust voids were being created. The Langmuir probe was attached in the same manner as the probe tip used to create the dust voids, but was *not* the same probe tip.

Using a probe tip as long as the one used to create the dust voids as a Langmuir probe introduces several complications, most notably the very large currents collected by such a big surface area, which make it much more difficult to properly evaluate the results. For this reason, the void-producing probe tip was removed and replaced with a similar, but much smaller, length of wire for taking Langmuir probe data. The new probe tip was made of Tungsten wire, with a diameter of 0.025" (635 μm), and a length of 3.23 mm.

Measurements were taken using a Keithley 2400 series sourcemeter, controlled by a LabView virtual instrument environment. At each set of operating conditions, the probe tip was swept from

a voltage of -100 V to +75 V, in steps of 1 V. At each voltage, the current to the probe from the surrounding plasma was recorded. The resulting I-V traces were processed as described in Ch. 2 to yield background plasma conditions, which can be seen in Table #-#. At each neutral pressure, and for each value of the applied axial magnetic field, the electron and ion Hall parameters (H_e and H_i, respectively), the plasma space potential (V_p), the floating potential (V_f), the electron temperature (T_e), and the plasma density (n) are provided.

B [Ga]	H_e	H_i	V_p [V]	V_f [V]	T_e [eV]	n [m^{-3}]
0	0	0	22	-9	4.3	4.90×10^{15}
60.2	2.606	0.0342	27	-19	5.2	1.50×10^{15}
70.0	3.031	0.0397	28	-19	5.4	1.43×10^{15}
83.0	3.594	0.0471	28	-19	5.4	1.30×10^{15}
98.4	4.260	0.0558	32	-20	6.2	1.34×10^{15}
119.0	5.152	0.0675	23	-22	4.5	9.51×10^{14}

(a) – 74 mTorr

B [Ga]	H_e	H_i	V_p [V]	V_f [V]	T_e [eV]	n [m^{-3}]
0	0	0	28	-5	5.4	4.92×10^{15}
60.2	1.929	0.0253	23	-18	4.5	1.34×10^{15}
70.0	2.243	0.0294	24	-19	4.6	1.43×10^{15}
83.0	2.659	0.0349	23	-20	4.5	1.35×10^{15}
98.4	3.153	0.0413	26	-21	5.0	1.35×10^{15}
119.0	3.813	0.0500	28	-21	5.4	1.27×10^{15}

(b) – 100 mTorr

B [Ga]	H_e	H_i	V_p [V]	V_f [V]	T_e [eV]	n [m^{-3}]
0	0	0	33	-3	6.3	5.25×10^{15}
60.2	1.286	0.0169	23	-22	4.5	1.21×10^{15}
70.0	1.495	0.0196	21	-25	4.1	1.18×10^{15}
83.0	1.773	0.0232	21	-26	4.1	1.20×10^{15}
98.4	2.102	0.0275	22	-27	4.3	1.23×10^{15}
119.0	2.542	0.0333	24	-26	4.6	1.18×10^{15}

(c) – 150 mTorr

Table 1: Langmuir Probe results for dust void operating conditions in the 3DPX chamber. Measurements were taken via single-tipped Langmuir probe without dust grains introduced into the plasma environment. Ion Hall parameter is calculated using an ion temperature value of $T_i = 0.025$ eV (room temperature).

There are a few details worth mentioning regarding these values. The first is that all of these measurements were, by necessity, taken without any dust grains present in the plasma environment. This is because of the fact that dust grains impacting the probe tip will very quickly leave residue on its surface which can significantly impact the reliability of future measurements made with the tip, and cleaning the tip can be quite time-consuming. At the applied voltages required to record a proper I-V sweep, it is a certainty that many dust grains would impact the probe tip. Therefore, the dust grains were not introduced into the plasma for these measurements, but it is fairly safe to say that at the dust number densities used in these experiments, there is unlikely to be any significant change to these values.

There may be some question regarding the validity of the Langmuir probe results under the influence of the applied magnetic field. The exact effect of magnetic fields on I-V traces is not yet fully understood, but it is widely agreed that results are valid so long as the Larmor radius is larger than the sheath thickness[70,71] (for our purposes, the Debye length). When the Larmor radius becomes small enough to be on the order of the Debye length, there is a substantial chance of magnetized particles failing to be collected by the probe, even within the sheath. This will always happen with electrons first, because their mass is much lower than that of the ions.

Using the electron temperature and density values measured without a magnetic field, the applicable range of electron Debye lengths can be calculated to be from 245-400 μm. At 60.0 Ga, the electron Larmor radius is 1.09 mm, and at 119.0 Ga, it is 554 μm. The fact that the electron Larmor radius is on the order of the sheath thickness indicates that, especially at higher fields, the Langmuir probe values may not be reliable. Still, the values are fairly reasonable, and so they may still be used going forward, with caution.

2. Video Processing Method

Videos captured via the camera setup described in Chapter 3 can be of limited use in their raw, unprocessed format, because of several issues. First, the contrast between the particles and the background can make it difficult to identify the particles, so that some image processing is needed. More importantly, in order to more completely understand the dust particle dynamics, creating aggregate images from sums of video frames can provide greater insight than individual video frames. Therefore, in order to properly analyze the results quantitatively, they must be converted into a more directly useful format from which numerical results may be easily extracted. Due to the large number of videos taken across many different varying operational conditions, it is not practical to process each video individually, so the processing technique also must be automated and easily applied to many different sets of videos.

ImageJ is an open-source image processing program, originally developed at the National Institutes of Health (NIH), with a wide array of flexible and robust tools for handling large quantities of images and videos quickly.[72] Using Fiji ("Fiji Is Just ImageJ"), a distribution of ImageJ with several additional capabilities[73], a macro was developed to process dust void videos quickly and then provide an output useable values, most notably the distance from the probe tip creating the void to the edge of the void (that is, the nearest dust grains) in each direction. The full text of the code can be found in Appendix 1. An example of this process is presented here.

Raw videos are recorded of a dust void at a frame rate of 30 frames/second for 300 frames (thus a single video lasts 10 seconds) at a size of 1280 x 1024 pixels and saved as an Audio Video Interleave (.avi) file. These videos are filmed in grayscale, rather than in 3-color RGB format, to lower the physical memory required without losing any significant information. It is helpful then

to think of a single video as a 300 x 1280 x 1024 matrix, in which each element is a single scalar gray value from 0-255. An example of a single frame of one such video is shown in Fig. (4-1).

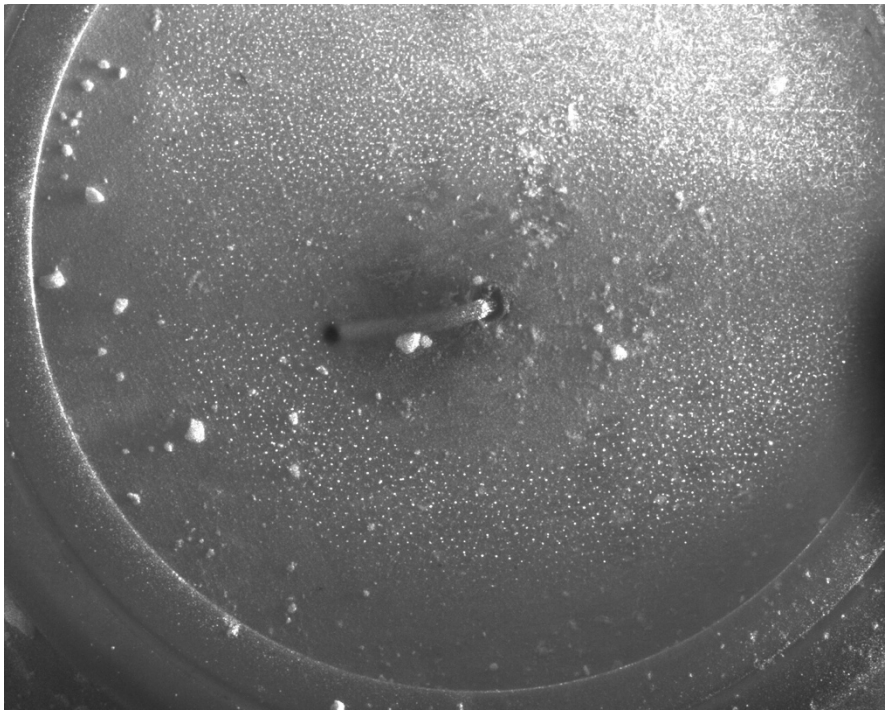

Figure 4-1: A single frame (out of 300) from a typical dust void experiment, as performed on the 3DPX experimental setup. The operating parameters were $P = 200\ mTorr, B = 60.2\ Ga, V_b = 0\ V$. The perspective in this image is aligned straight downwards (the direction of gravitational acceleration is into the page), and dust grains are visible floating above the tray. The dust grains are illuminated by a laser light sheet which is incident from the right side of the photo. The confining ring is also visible along the edges of the image. The probe tip can be seen extending upwards from the tray. Although the probe appears to lean significantly to the left in this image, this is primarily an optical illusion due to the scale of the image. In actuality the probe is very near to perfectly vertical, perpendicular to the plane of the tray. The dust grains can be seen as white dots in this image, particularly in the lower half of the image. In this "raw" snapshot, the dust particles are difficult to distinguish from the background in the upper part of the image.

Other than the floating dust grains, the elements within the frame will change very little over the course of a single video. This makes is a simple task to remove these elements from the frame entirely, leaving only the dust grains. Each pixel's minimum value is recorded over the course of

all 300 frames, and these minimum pixels are then assembled into a single frame, representing the constant background elements of the video. An example of a background image generated in such a way can be seen in Fig. (4-2).

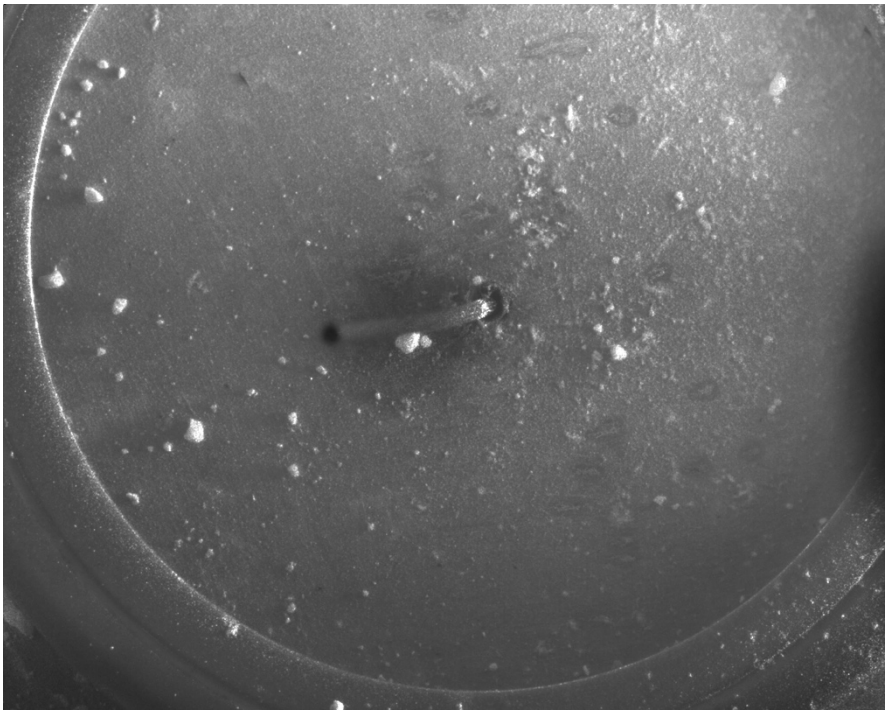

Figure 4-2: The background frame, as generated from the video from which Figure 4-1 was taken. Note that other than the disappearance of the floating dust grains, the other elements of the frame are overwhelmingly unchanged. It is worth emphasizing that this is not a photo of the same system without any floating dust grains, but a generated background image from the video in which the floating dust grains were visible.

With the background image generated, the background elements can effectively be removed from the original video, leaving only the floating dust grains in the frame. Over all 300 frames of the original video, each pixel has its associated minimum value subtracted, resulting in a new video featuring the floating dust grains over a dark background. A single frame from such a background-removed video can be seen in Fig. (4-3).

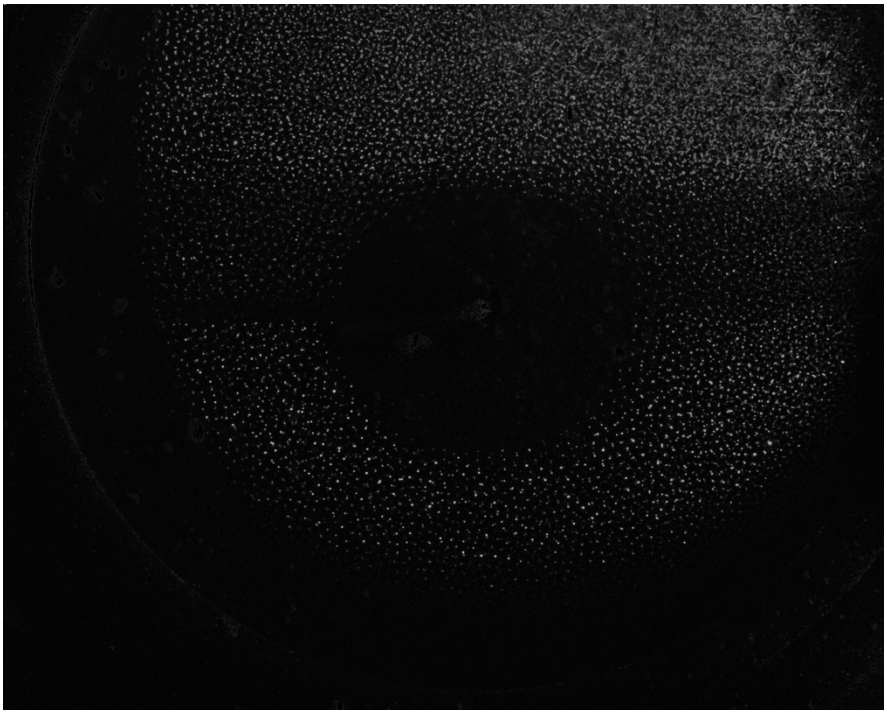

Figure 4-3: A single frame (out of 300) of a background-removed video. Other than a few very minimal artifacts (for instance, slight reflections from the base of the probe and the confining ring), only the floating dust grains remain. The shadow of the probe tip in the laser light sheet can be seen to the left of the dust ring (at the approximately 9:00 position). The structure of the dust void is now much more plainly visible to the naked eye. Additionally, the dust particles that were originally obscured by the background in the upper half of the original image can now be clearly identified in this image.

Now that the particles can be clearly identified, an additional analysis is performed to determine the overall dynamics of the particles over the 300 video frames. This is done in a manner similar to the construction of the background image. Here, the maximum pixel intensity is recorded at each location in each video frame and assembled into a new, single composite image, revealing the full range of all floating dust grains over the course of the video. This image displays the dust void very clearly and is very useful for making measurements. An example is shown in Fig. (4-4).

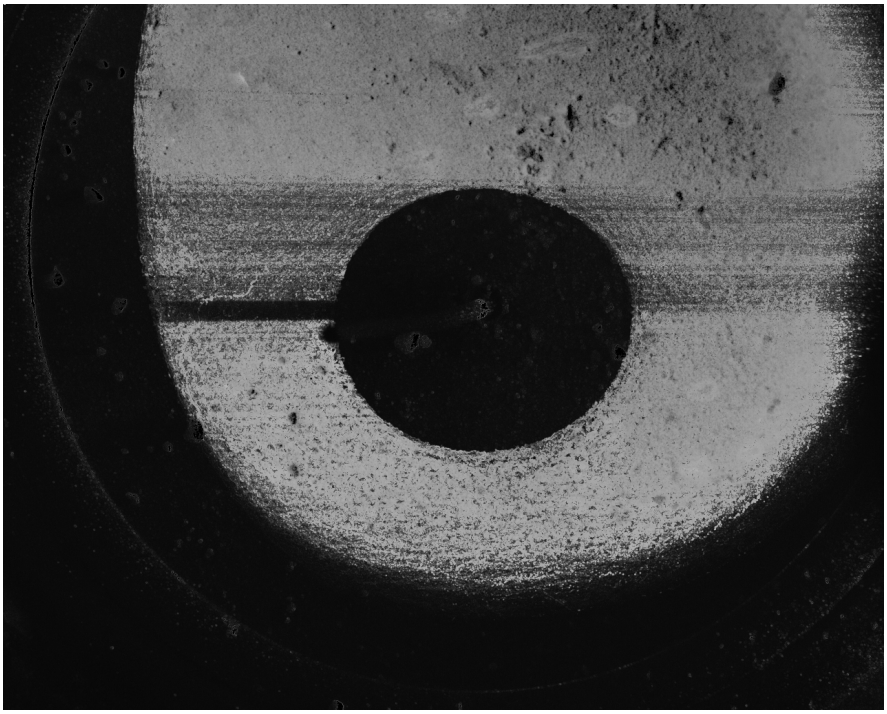

Figure 4-4: The resultant image consisting of the maximum value of each pixel over all 300 frames. This image clearly shows the exact extent of the floating dust grains, and the boundary of the dust void is clear and sharply defined. The shadow of the probe tip in the laser light sheet can be seen as a dark band on the left side of the void. The end of the probe tip can also be seen slightly below this band, a very small dark spot blocking the floating dust from the camera's view.

To minimize the spatial errors that could arise from very small variations (on the scale of a few dust grains) within the image, a Gaussian blur filter is applied to this image, with a rolling 5 pixel radius. The location of the probe tip within the image is also marked at this point in the process. Because the probe is not perfectly vertical for its entire length, the probe tip's location at the height even to the dust grains and the laser light sheet must be measured and entered manually. This is a simple task however, as both the camera system and the probe/laser system remain completely stationary over the entire course of an experiment, which means that only one measurement is needed for several sets of videos. If the camera is moved even slightly, these small deviations can significantly impact the location of the probe within the frame of the videos.

Therefore, a new location must be measured and entered. This occurred only once over the course of all of the videos recorded for this work, and the probe location was properly measured and adjusted within the analysis software for the appropriate videos. An example of a blurred and marked frame can be seen in Fig. (4-5).

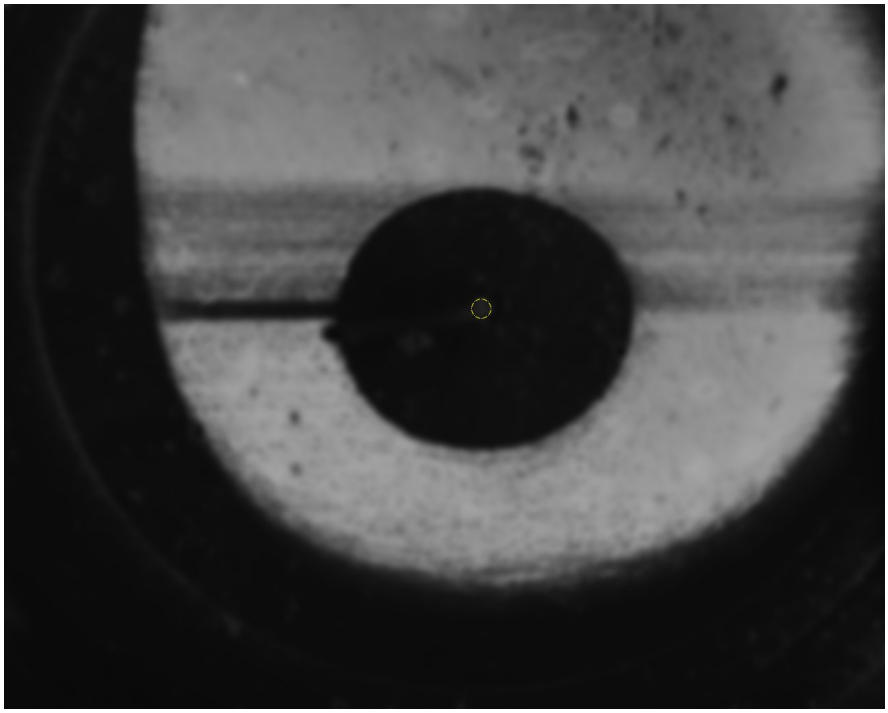

Figure 4-5: The Gaussian blur applied over the frame has the twofold benefit of reducing the risk of introducing an error due to very small variations at the void edge, as well as washing out most of the undesired background reflections that were not fully subtracted out previously. The location of the probe tip is marked with a yellow circle in the center of the dust void.

With the processing of the video file now completed, a method for determining analyzing the spatial properties of the probe induced voids is now developed. Because variations are expected in the radius of the dust void based on the angle between the measured radius and the magnetic field vector (downward, from top to bottom in these images), it is important to measure the void radius not in just one direction, but in four: namely, the $+\vec{B}$ (downward), $-\vec{B}$ (upward), $+\overrightarrow{E_{sh}} \times \vec{B}$ (leftward), and $-\overrightarrow{E_{sh}} \times \vec{B}$ (rightward) directions. The electric field $\overrightarrow{E_{sh}}$ here refers to the downward

sheath electric field from the bulk plasma (with a positive space potential) to the tray, which is electrically grounded.

In order to obtain these radius measurements, the grayscale values of individual pixels must be analyzed. For a given direction, grayscale values are compared, moving in a straight line outwards from the edge of the probe tip. At each length, the grayscale values are averaged over a linear range of 5-11 pixels, centered on the radial line from the probe tip to the void's edge. This average grayscale value is compared to the same measurement taken 20 pixels (~450 μm) nearer to the probe tip. This difference is compared to a threshold value, and when it meets or exceeds that value, the iterative process ends and the current length is recorded. This process is repeated for the up, down, and right directions.

Because of the shadow of the probe tip (which is effectively indistinguishable from the background, although there are dust grains in the region), the leftward direction requires a slightly more complicated modification of this process. Rather than being centered on the radial line, the same process is repeated with a slight offset from this line, just enough to be outside the range of the probe tip's shadow. Because of the curvature of the dust void's boundary, this process will typically yield a value slightly smaller than the actual radius, by a difference on the order of 5-10 pixels (~100-200 μm). This difference can be mitigated by slightly adjusting the threshold value of the pixel comparison process.

After the measurements are made, line segments are drawn at these lengths from the probe tip's surface. This allows large sets of processed videos to be quickly visually inspected, and any discrepancies (measurements that are too long or too short to accurately represent the specified void radius) can be amended with slight adjustments to the threshold value for that particular measurement. In some extreme cases (for instance, if the lighting from the laser was inconsistent,

causing difficulties comparing pixel values to find a clear edge), the boundary was measured and the length inputted manually. These cases accounted for 267 individual measurements out of 1672 (~16.0%).

With the lines drawn and confirmed visually, the radii measurements in each direction are exported in a comma separated value (.csv) format file, allowing them to be easily organized, sorted, and analyzed. The final result of this process, with the measured radii overlaid, can be seen in Fig. (4-6).

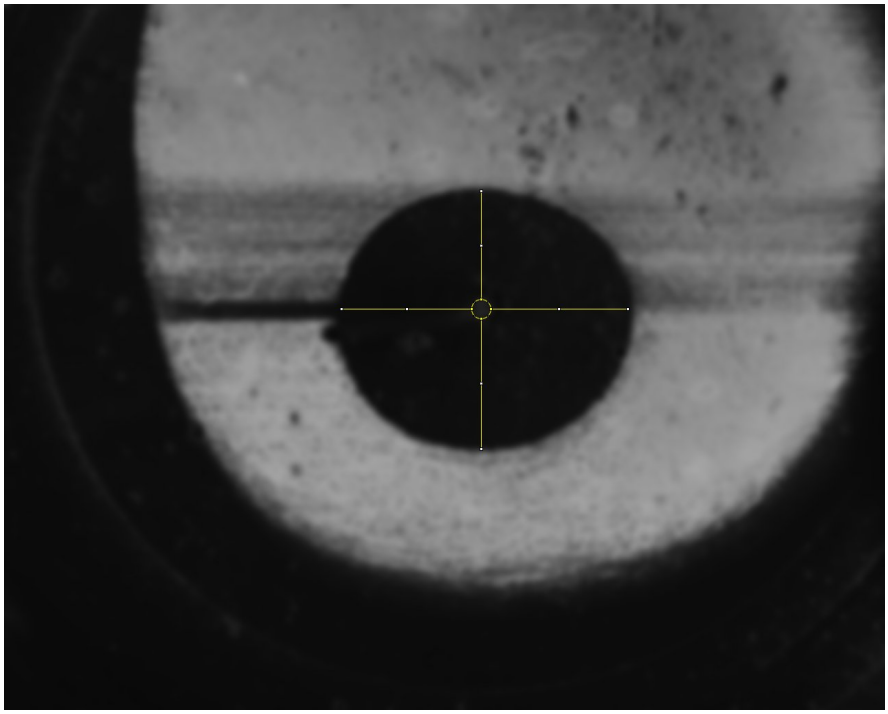

Figure 4-6: Final processed and measured image from the original 300 frame video. The probe tip's location can be seen in the center, and the radii, as measured programmatically with Fiji, can be seen extending to the void boundary in each direction. These measurements are outputted as a .csv file to be analyzed.

3. Initial Results (No Magnetic Field)

In order to properly evaluate the influence of the applied magnetic field on the formation of dust voids, it is necessary first to establish a baseline of results without a magnetic field. Dust voids were formed in the 3DPX chamber using 8 μm diameter dust grains, in argon plasmas generated by 20 W of rf power at 13.56 MHz. The central probe tip was swept from -40 V to +40 V in steps of 5 V, and at each step the void was filmed at 30 fps for 300 frames (10 seconds total). This was repeated for voids formed at neutral pressures of 74 mTorr, 100 mTorr, and 150 mTorr ($\pm$ 0.5 mTorr). A sample of these dust voids after being processed for measurement can be seen in figure 4-7. The relation between the probe bias potential and the void size, both in the vertical and horizontal directions (which, for later experimental cases with the permanent magnets attached, will correspond to the directions parallel to the magnetic field ($\parallel \vec{B}$) and perpendicular ($\perp \vec{B}$)), can be seen in Fig. (4-8).

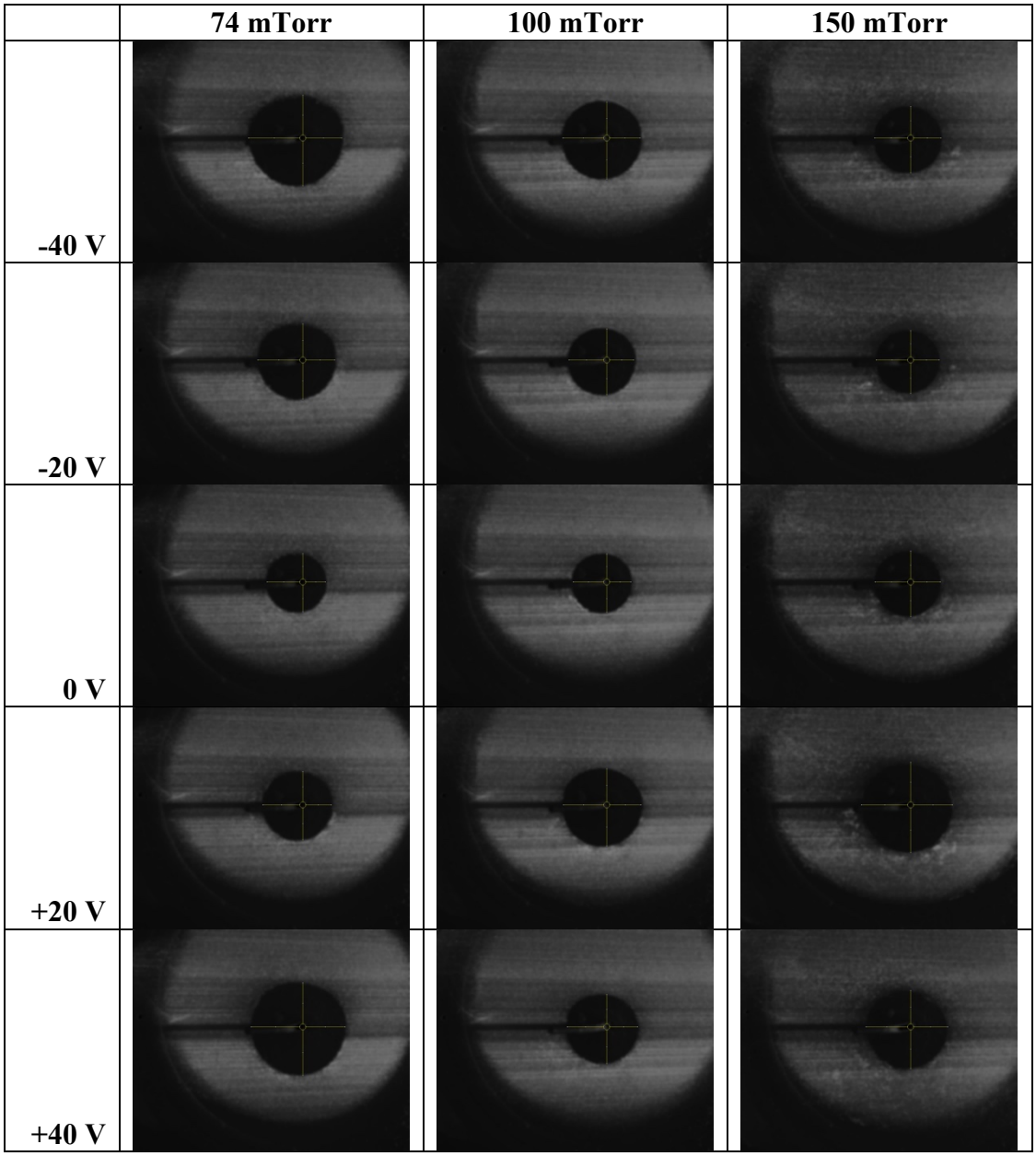

Figure 4-7: Sample images from processed videos of dust voids without an externally applied magnetic field. The size of the dust void can be seen to change size with as the probe bias voltage is changed. The effect of neutral pressure is also evident. The yellow markings indicate the dimensions of the dust voids as measured by the automated analysis code in ImageJ.

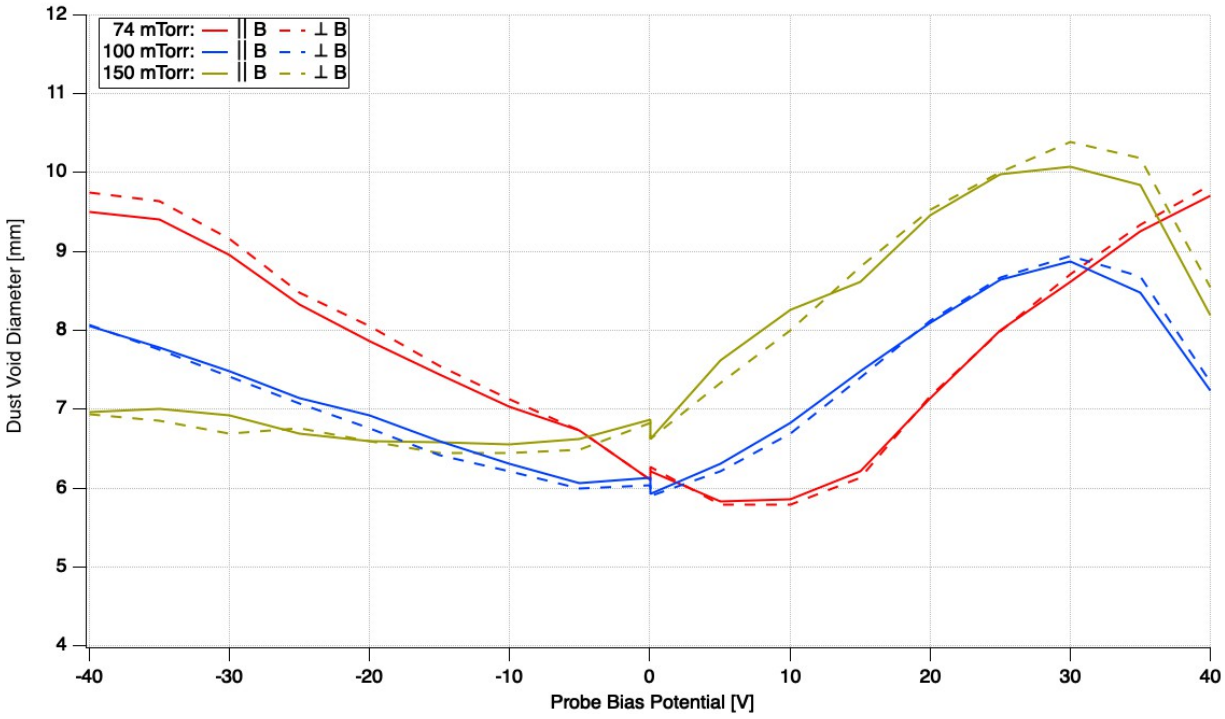

Figure 4-8: Relationship of probe bias potential to dust void diameter, in both the vertical and horizontal directions. While there is no externally applied magnetic field in these cases, the vertical dimension will, in later experiments, correspond to the direction parallel to the magnetic field vector ($\parallel \vec{B}$), and the horizontal dimension to the direction perpendicular ($\perp \vec{B}$). The differences between the horizontal and vertical measurements are a result of the probe tip having a very slight lean. This lean is consistent across all experiments on this apparatus, however, so we may use the non-magnetized cases to adjust the magnetized cases for this small difference. The discontinuity at the point where the probe bias is 0 V is due to the switching effect when the probe's power supply crosses over from negative to positive potentials.

When the probe was negatively biased, the dust voids tended to be fairly large, and they decreased in size as the bias potential was increased, minimizing close to a bias of $V_B = 0$ V. After this, the voids increased in size again as the bias potential became more positive. In the case of the 100 and 150 mTorr dust voids, the voids once again began to decrease in size once the bias potential crossed the plasma space potential. This did not occur in the 74 mTorr case, although it is quite possible that the same downturn in void radius would occur at a probe bias voltage some

amount higher than the maximum voltage used in these experiments (+40 V). The physical significance of these results will be discussed in much greater detail in Section #-#.

Without any externally-applied magnetic field, the differences between the void's size when measured vertically as opposed to horizontally are attributed to the slight angular deviation of the probe tip. Were the probe tip perfectly perpendicular to the tray, and the entire apparatus perfectly level, the dust void should appear perfectly circular. These differences will be utilized in magnetized cases to adjust for the effect of this deviation so that the true effect of the magnetic field in making the dust void's shape non-symmetric may be determined.

Because the dust voids are nominally circular, a simple way to measure and compare the extent of this non-symmetric property is to calculate the geometric eccentricity. The eccentricity of a conic section is a non-negative real number which uniquely characterizes the shape of the conic section. The eccentricity ε of an ellipse is calculated:

$$\varepsilon = \sqrt{1 - \frac{b^2}{a^2}} \qquad (---)$$

where a and b are the semi-major and semi-minor axes, respectively. The semi-major axis of an ellipse is defined as half of the major axis, that is the line segment running through the foci of the ellipse and reach the perimeter on both ends. In other words, the semi-major axis is the longest straight segment from the center of the ellipse to the perimeter.

For ellipses, the geometric eccentricity is confined to be less than 1, or $0 \leq \varepsilon < 1$. An eccentricity of exactly 0 indicates a perfect circle, with a constant radius in all directions. The higher an ellipse's eccentricity, the more it deviates from being perfectly circular. An illustration of various ellipses and their associated eccentricities can be seen in Fig. (4-9).

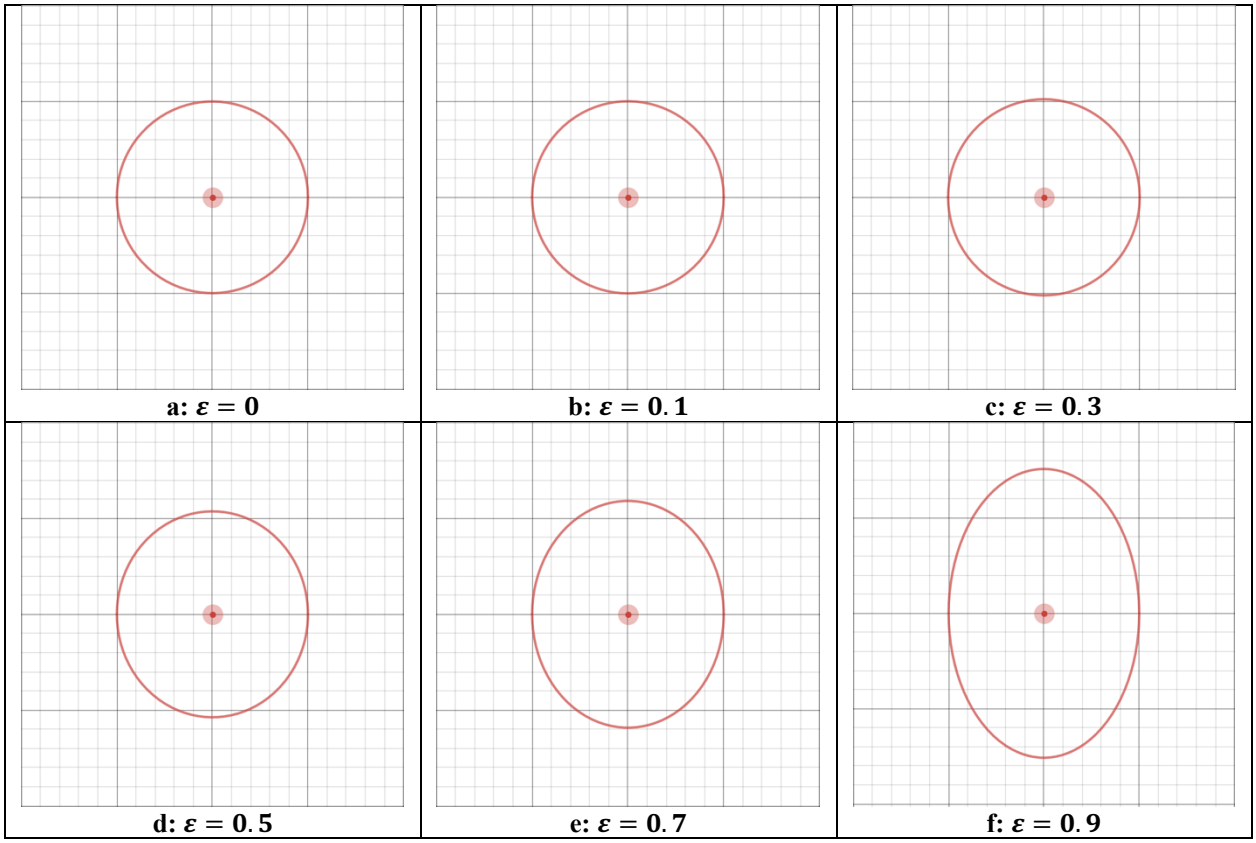

Figure 4-9: An illustration of various ellipses, with their associated geometric eccentricities displayed. Ellipse (a) has an eccentricity of 0, indicating that it is a perfect circle (that is, it has a single constant radius). The higher the eccentricity, the more the ellipse deviates from being circular, indicating that the minor and major axes are more and more different from one another. These images were generated at www.desmos.com.

The vertical axis is calculated as the sum of the "up" and "down" measured radii as well as the diameter of the probe tip (since the automated measurements are made starting from the surface of the probe, rather than the "true" center of the void), and likewise the horizontal axis is calculated similarly with the "left" and "right" measured radii. Defining the semi-major and semi-minor axes as half of the larger and smaller of the two axes, respectively, the eccentricities of the dust voids at each probe bias value can be calculated. These values for the non-magnetized dust voids can be seen in Fig. (4-10).

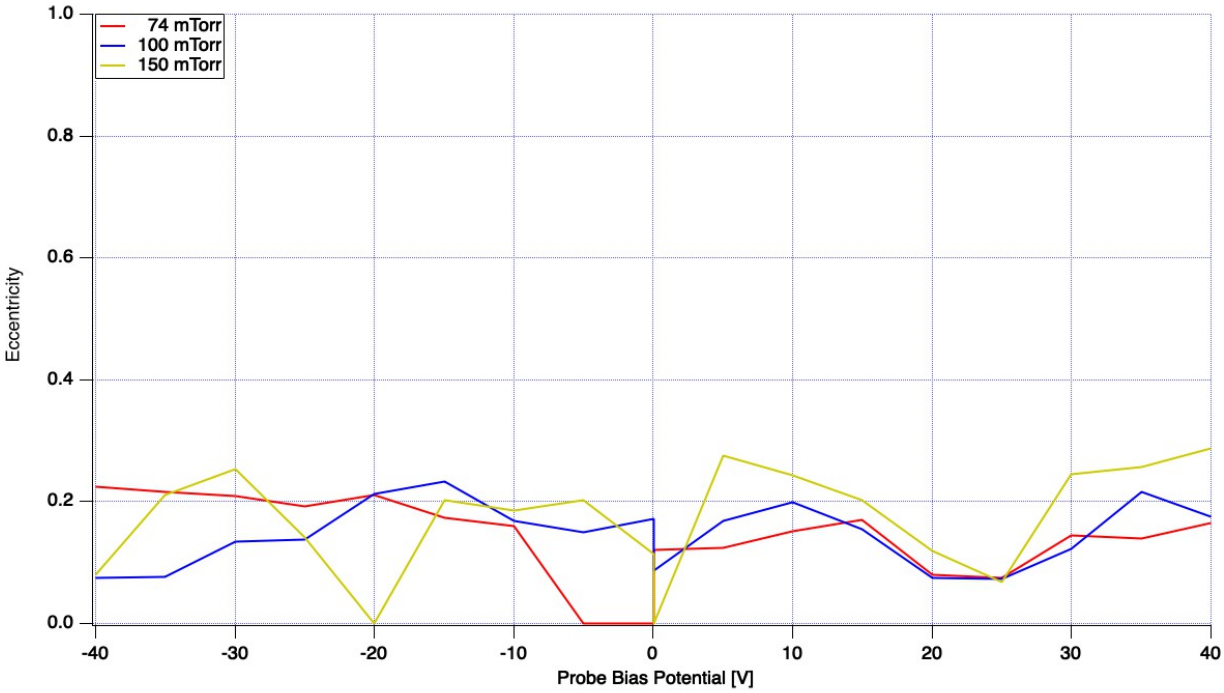

Figure 4-10: Measured geometric eccentricity of dust voids without an external magnetic field as a function of probe bias potential. In these cases without the addition of an external magnetic field, the eccentricity tends to be quite low, indicating a nearly perfectly circular dust void. The small non-zero values for eccentricity will be essential in characterizing the effect of the magnetic field on dust void shape in later experiments.

While the dust voids created without the external magnetic field are not perfectly circular, they are very nearly circular, as is evident from their relatively low geometric eccentricities. The average value of the eccentricity for all three cases was ~0.175 ± 0.077, as calculated from the average and standard deviation of the B = 0 data.

4. Magnetized Results

With the addition of the externally applied magnetic field via the permanent magnets, the same conditions were examined as in the previous (no magnetic field) cases. The dust voids were created with 8 μm diameter dust grains in plasmas generated with 20 W of rf power, and the probe bias potential was swept from -40 V to +40 V in steps of 5 V. Once again, this was repeated at neutral pressures of 74, 100, and 150 mTorr. Additionally, at each neutral pressure, this series of sweeps

was performed first with the permanent magnets mounted as far away from the plasma-generation / probe apparatus as physically possible within the confines of the experimental apparatus (approximately 16.1 cm from the probe tip, which was at the center of the chamber), and then performed again with the permanent magnets each moved in 1 cm (so that the magnets remained evenly spaced around the probe tip and the dust voids). This was repeated until the magnetic field became strong enough that the plasma was no longer capable of confining the dust grains in a stable manner, typically when the magnets were each ~11 cm from the center. Using the magnetic field characteristic from Section (3-6), it may be calculated that at the largest separation of the magnets (16.1 cm), this will produce an axial magnetic field of 60.2 Gauss at the location of the probe and 66.1 Gauss 1 cm away from the probe tip along the axis. At the smallest separation (12.1 cm), this will produce an axial magnetic field of 119.0 Gauss at the location of the probe and 121.4 Gauss 1 cm away from the probe tip along the axis. A sample of dust voids at various values of the axial magnetic field can be seen in Fig. (4-11).

	74 mTorr	100 mTorr	150 mTorr
B = 60.2 Ga	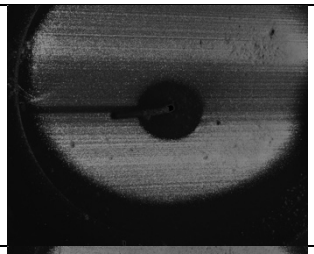	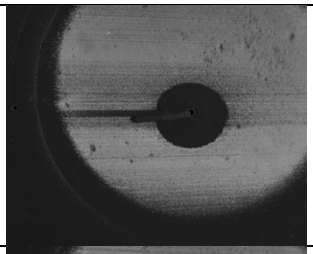	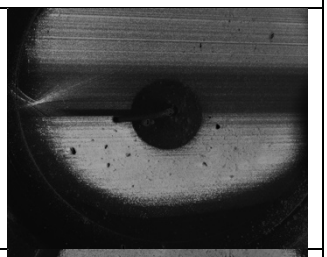
B = 70.0 Ga	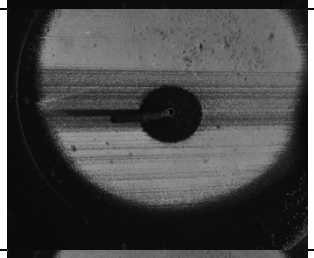	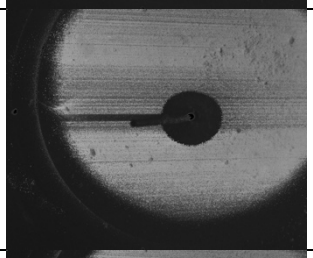	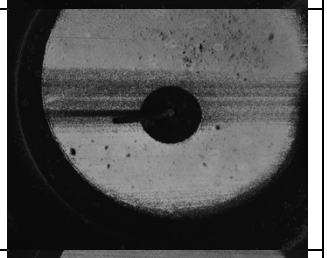
B = 83.0 Ga	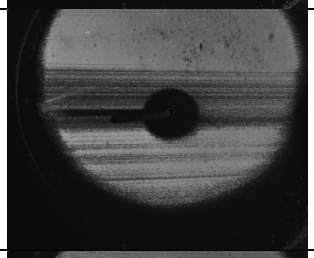	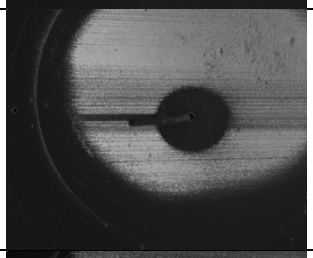	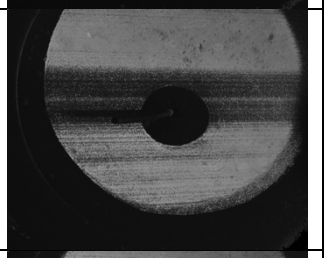
B = 98.4 Ga	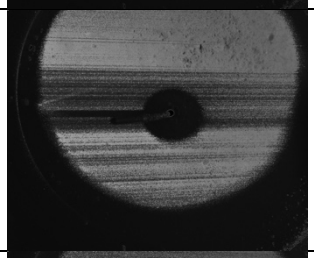	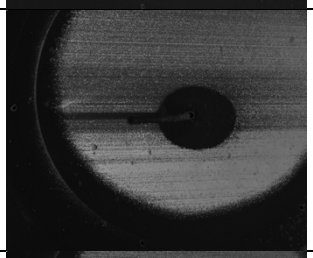	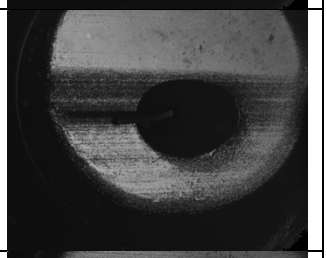
B = 119.0 Ga	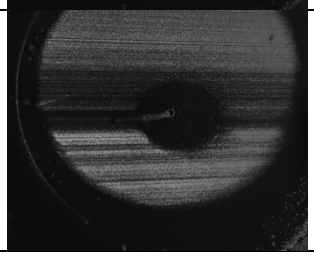	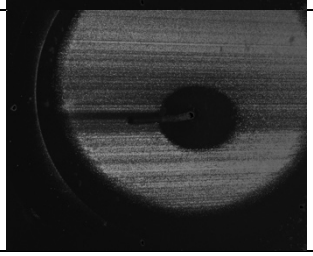	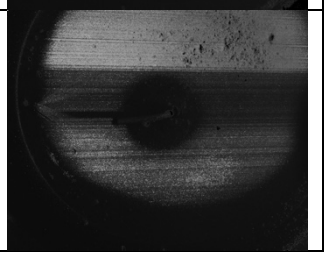

Figure 4-11: Sample images of dust voids at various magnetic field strengths. The magnetic field values listed in the table refer to the axial field $\vec{B}_z$, which in the perspective of these images points in the downward (top-to-bottom) direction. All of the voids in this table were filmed with the probe bias potential at 0 V. Multiple effects of the magnetic field are evident from these images, including the general size dimensions of the void becoming larger and an increasing asymmetry of the void shapes.

Some of the effects of the magnetic field are visually evident from the series of images in Fig. (4-12). Perhaps the most immediately obvious is the increasing asymmetry of the dust voids as the field is increased. As the background plasma becomes increasingly magnetized, the velocity distributions of the ions and electrons become much less isotropic and increasingly directional. The ions in particular alter the shape of the dust void as their paths become more dominated by magnetic field effects, which in turn changes the magnitude of the ion drag force on the dust grains and moves the location of the void boundary.

Examining the 74 mTorr case, specifically the dust void dimension in the $\vec{E} \times \vec{B}$ (leftwards) direction (see Fig. (4-13)), there is a significant increase in the void's size at the highest level of the magnetic field when the probe is positively biased. This trend indicates a great increase in the ion flow (and therefore the ion drag force) in the $\vec{E} \times \vec{B}$ direction when the ions are being repelled away from the probe, even at a relatively low magnetization. The quantitative aspects of this increased ion flow, as well as the associated magnetization levels, will be discussed in Section (#-#).

Also noteworthy in Fig. (4-13) is the overall decrease in the void size at negative probe bias potentials. Because voids generated by a negatively biased probe are driven by the Coulomb repulsion of negatively charged dust grains from the probe tip, this trend indicates that even small increases in the magnetic field are enough to begin affecting the dust grain charge. Because electrons magnetize at much lower fields than ions, it is reasonable to expect that the dust-charging process would diminish even at very low fields.

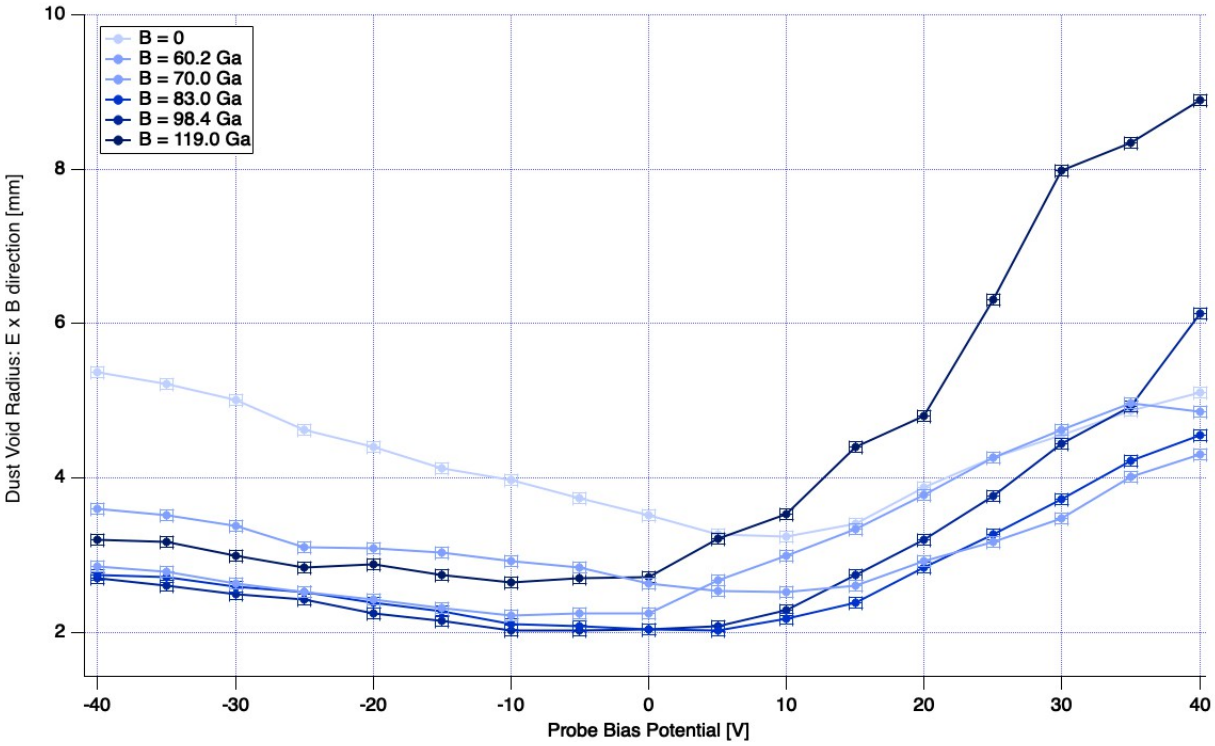

Figure 4-12: Void dimension in the $\overrightarrow{E_{sh}} \times \vec{B}$ (leftward) direction as a function of probe bias potential. Values here are from voids created at 74 mTorr of background pressure. The dramatic increase when the probe is biased positively indicates that the ion drag force has become quite strong in this direction as the magnetic field's effect on the ion trajectory is increased.

Observing the same dust voids but with an emphasis on the $+\vec{B}$ (downward) direction (Fig. (4-14)), there is no such trend when the probe is biased positively, further stressing the significance of the trend in the $\vec{E} \times \vec{B}$ direction. The fact that these measurements are taken simultaneously from the same dust voids eliminates any differences in operating conditions as an alternative explanation for this discrepancy. Once again, the effect of decreased dust charge is evident as the electrons become magnetized, as indicated by the decrease in the void dimension at negative biases where the dust is repelled.

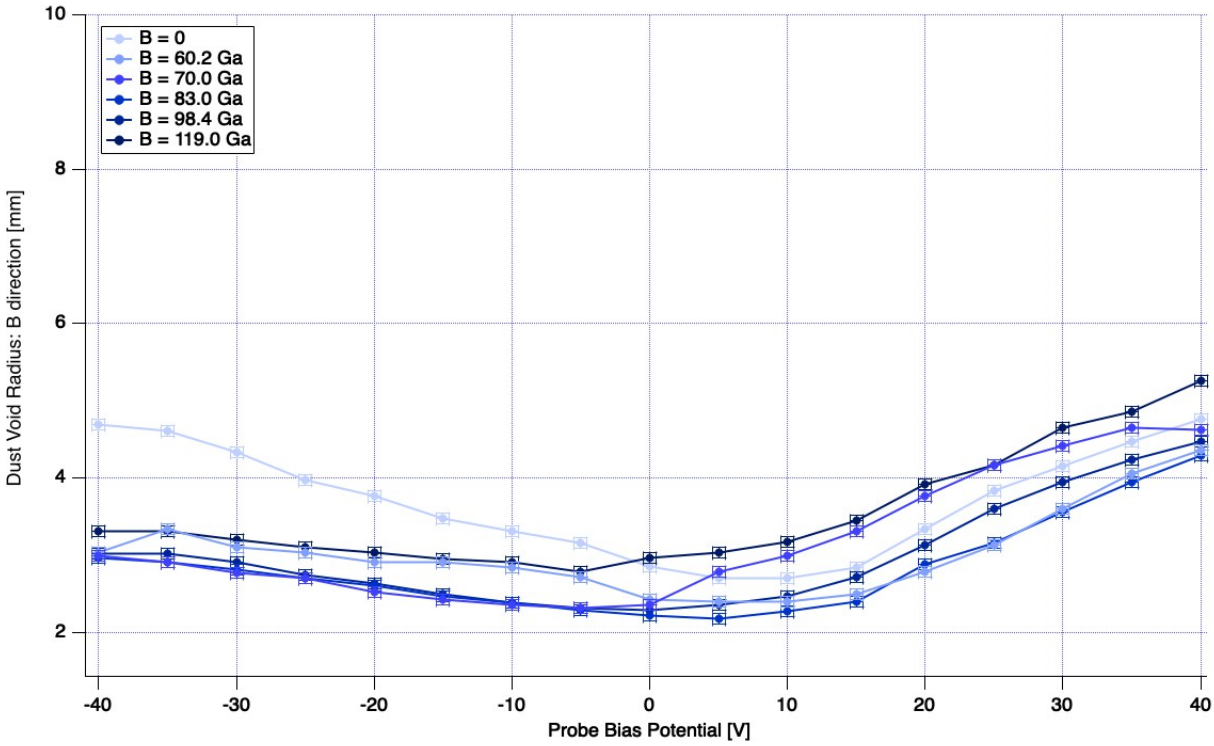

Figure 4-13: Void dimension in the $\vec{B}$ (downward) direction as a function of probe bias potential. Values here are from voids created at 74 mTorr of background pressure. As opposed to measurements made in the $\vec{E} \times \vec{B}$ direction, there is no significant trend here as the magnetic field is increased. This observation supports the conclusion that ion flow is increased in the $\vec{E} \times \vec{B}$ direction, causing asymmetry in the void geometry. Notably, the same trend exists here in the negatively biased region, again suggesting that the dust charge is affected even at low magnetic fields.

The geometric eccentricity of the dust voids can also be examined as a function of magnetic field and probe bias potential (see Fig. (4-15)). It should be noted once again that, especially at larger fields where the void's shape is more distorted, this is not a "true" eccentricity, as the voids are not true mathematical ellipses, and the $\parallel \vec{B}$ and $\perp \vec{B}$ dimensions of the void are not truly major or minor axes. The "eccentricity" discussed here is using the geometric concept as a means to quantify the degree to which the void's shape has become asymmetric and is quite suitable for our purposes.

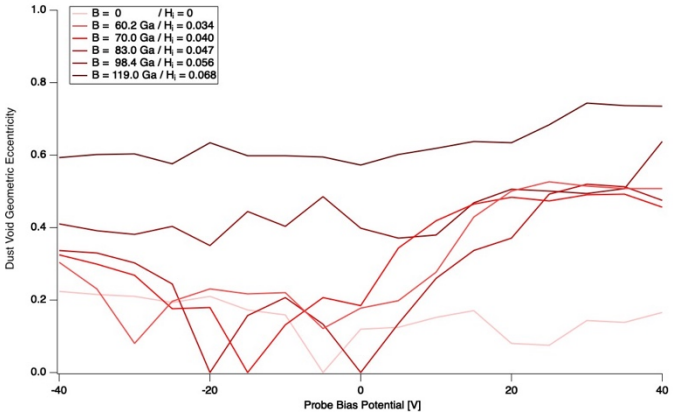

(a) – 74 mTorr

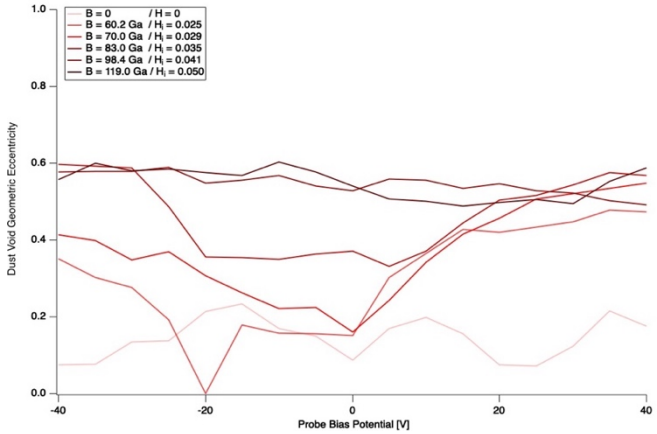

(b) – 100 mTorr

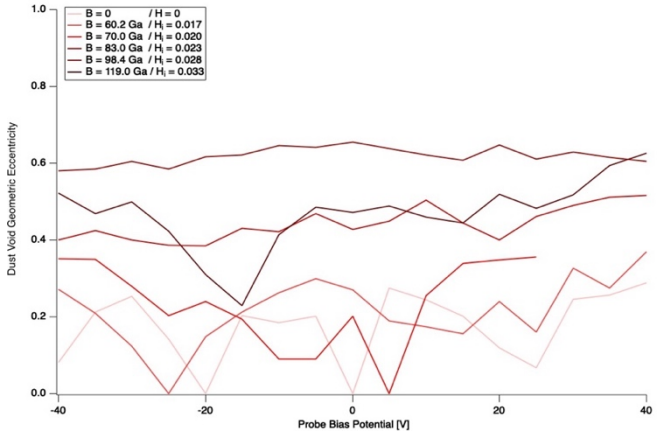

(c) – 150 mTorr

Figure 4-14: Geometric eccentricity of dust voids as a function of probe bias potential. The voids become increasingly deformed as the magnetic field is increased, particularly when the probe is positively biased. This effect is somewhat diminished at higher background pressures, especially 150 mTorr, due to the higher density of neutrals lowering the ion and electron Hall parameters, and thus the effect of the magnetic field.

The eccentricities of the dust voids are consistently higher, indicating that the voids are more elongated, at higher magnetic fields. This effect is particularly strong when the probe is biased positively. As the background pressure is increased, the increased rate of collisions with neutral particles diminishes this effect somewhat, as can be seen in the 150 mTorr case.

It must be noted here that after completing the data collection process, it was discovered that three recorded video files had become irreparably corrupted. Specifically, these were the videos taken with a background pressure of 150 mTorr, with a central magnetic field of 70.0 Ga, at probe bias potentials of +30 V, +35 V, and +40 V. This was unfortunately not discovered until after the experimental apparatus had been partially disassembled in a way that would make it prohibitively difficult and time-consuming to reassemble the experiment and capture these three videos again, and even were this to be done, it is likely that subtle differences in positioning of the various components of the apparatus would affect the results in a way that would make them more difficult to compare realistically with the rest of the data set. This is a relatively very small amount of data lost, but its absence can be noticed in presented results beginning with Fig. (4-14 (c)) and moving forward.

In Fig. (4-15), the geometric eccentricities of the dust voids are plotted as a function of ion Hall parameter, once again sorted by neutral pressure and probe bias potential.

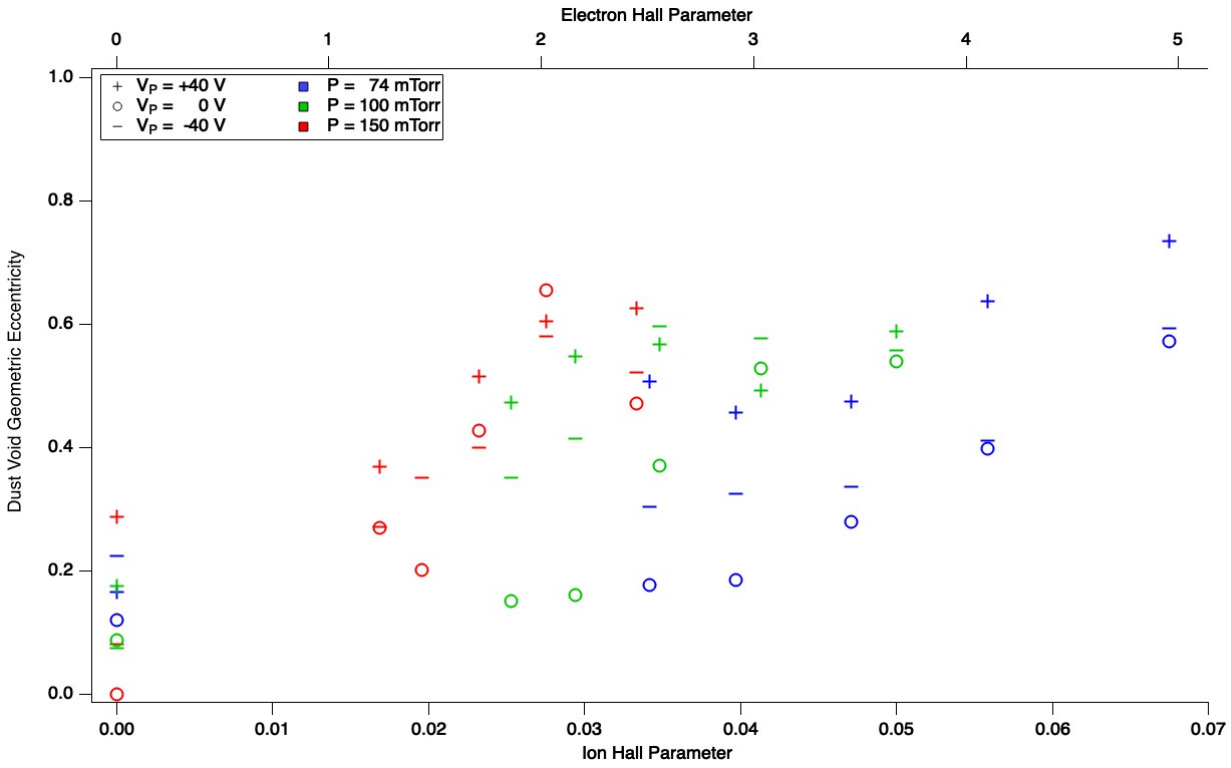

Figure 4-15: Dust void geometric eccentricity as a function of ion and electron Hall parameter. Non-magnetized cases are included ($H_i = 0$). The effect of the magnetic field in deforming the dust voids is quite strong, especially in the 74 mTorr cases. As before, the effects of the magnetic field are most clearly visible at lower pressures, even across similar ion Hall parameters. Even at very low Hall parameters though, the void is significantly deformed as compared to the non-magnetized cases.

The void deformation effect is quite evident visually by looking at the dust voids themselves. A sample of dust voids at 74 mTorr, at a range of probe bias potentials, can be seen in Table 2.

	$V_P = -40\ V$	$V_P = 0\ V$	$V_P = 40\ V$
B = 0, ***H_i = 0,*** ***H_e = 0***	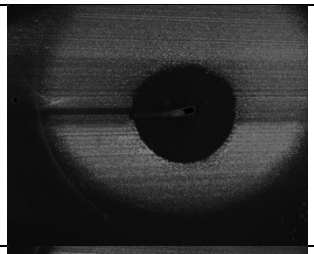	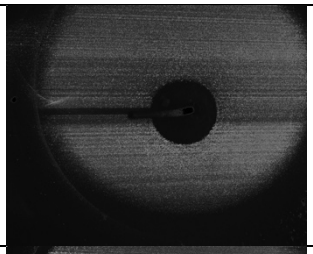	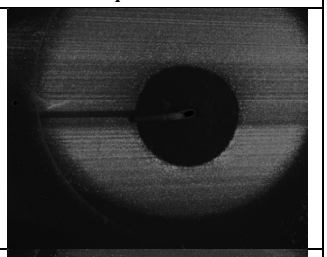
B = 60.2 Ga, ***H_i = 0.034,*** ***H_e = 2.51***	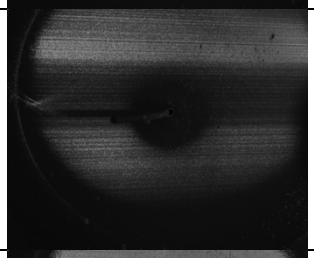	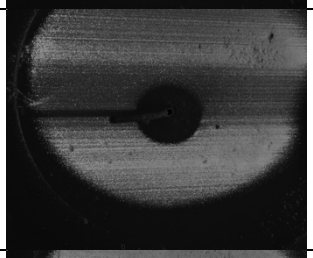	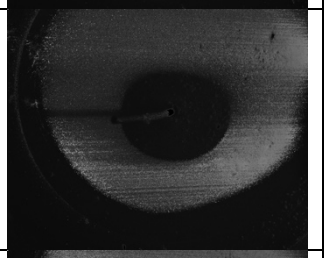
B = 70.0 Ga, ***H_i = 0.040,*** ***H_e = 2.92***	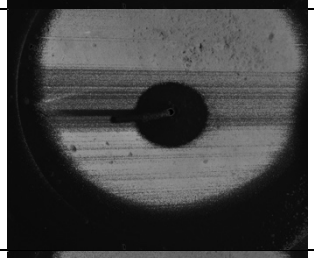	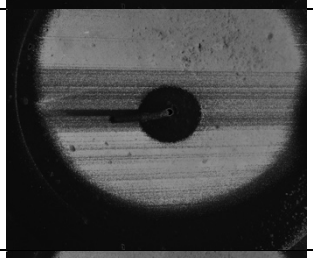	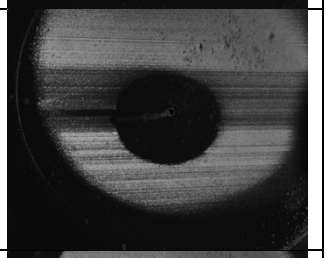
B = 83.0 Ga, ***H_i = 0.047,*** ***H_e = 3.46***	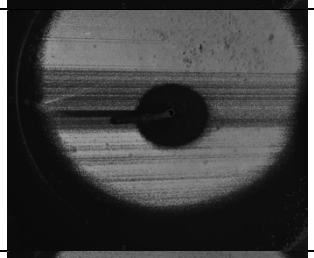	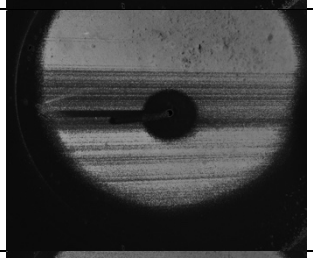	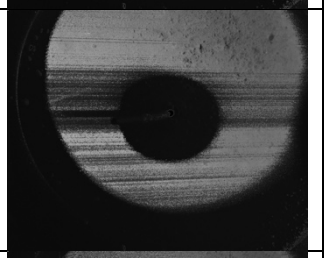
B = 98.4 Ga, ***H_i = 0.056,*** ***H_e = 4.10***	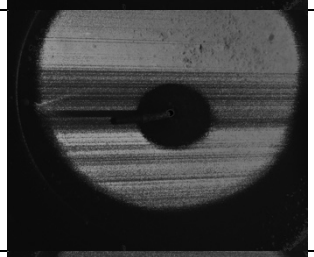	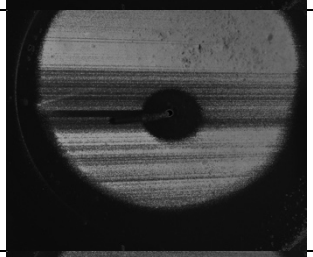	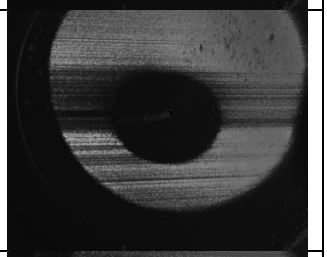
B = 119.0 Ga, ***H_i = 0.068,*** ***H_e = 4.96***	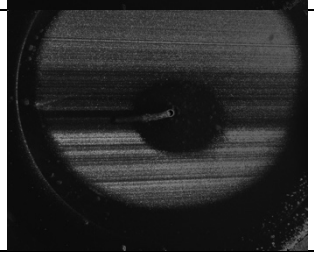	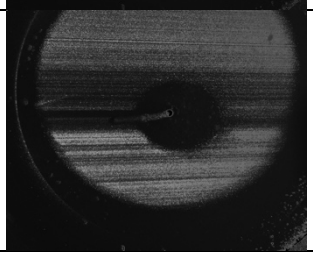	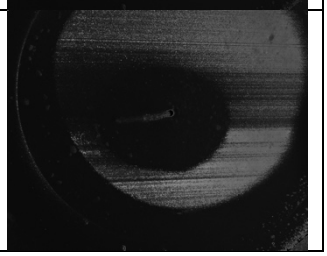

Table 2: Array of dust voids generated at 74 mTorr of background pressure. As the magnetic field (downward in these images) increases, the void's shape can be seen to deform more and more. The net result of this effect can be seen in Figure 4-15.

The degree to which the dust void is centered around the probe tip can also be examined. In order to contextualize the degree to which the magnetic field has affected the radial symmetry of the dust void, the differences between the measured void dimensions in the directions anti-parallel and parallel to the magnetic field (upward and downward, respectively), and between the $-\overrightarrow{E_{sh}} \times \vec{B}$ and $\overrightarrow{E_{sh}} \times \vec{B}$ directions (rightward and leftward, respectively) are calculated. With these two values, the degree to which the body dust void has shifted over the probe tip is represented as a 2-dimensional vector. The farther each point is from the origin, the less symmetric the dust void is over the probe tip. The results of these calculations as a function of magnetic field are shown in Fig. 4-16. Because the magnetic field effects are most pronounced at extreme values of the probe voltage, the offset values are shown for the dust voids formed around probe tips biased to 40 V and -40 V, as well as 0 V for reference.

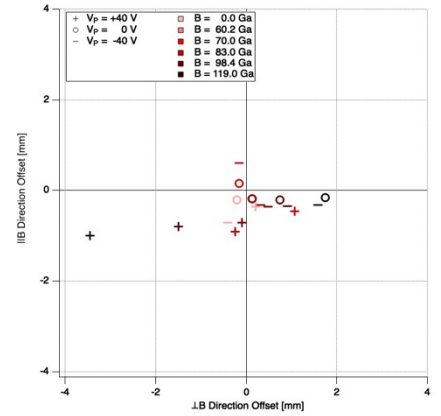

(a) – 74 mTorr

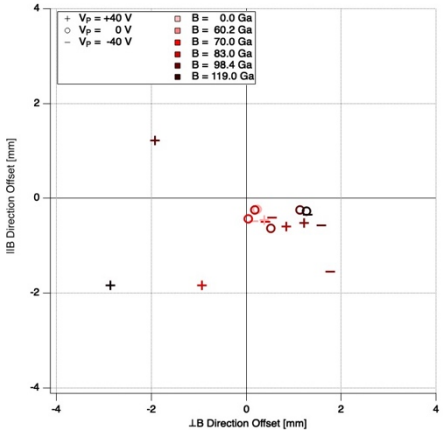

(b) – 100 mTorr

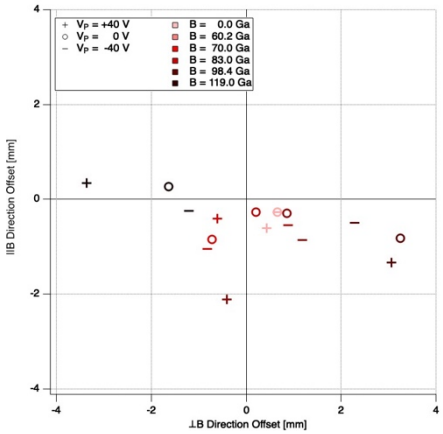

(c) – 150 mTorr

Figure 4-16: The dust void's offset, in mm, from being centered over the probe tip, in both the $\vec{B}$ and $\overrightarrow{E_{sh}} \times \vec{B}$ directions. For a given dust void, at a particular probe voltage and magnetic field strength, the location of the offset in the 2-dimensional coordinate planes above indicates the location of a vector from the probe tip to the geometric center of the void. The tendency to distort much more in the direction perpendicular to $\vec{B}$ than in the parallel direction is emphasized.

The tendency to become distorted as the magnetic field increases is evident from Fig. (4-16). The deformation happens much more significantly in the direction perpendicular to the magnetic field than the parallel direction, as would be expected based on the nature of interactions between magnetic fields and charged particles. Especially noticeable in the lower neutral pressure cases is the tendency for the void to drift in the $-\overrightarrow{E_{sh}} \times \vec{B}$ direction when the probe is biased negatively, and to drift in the $\overrightarrow{E_{sh}} \times \vec{B}$ direction when the probe is biased positively. The nature and physical meaning of this change of direction for the dust void shift will be examined in the Discussion section later in this chapter.

To more effectively separate the specific effects of the magnetic field on the dust void's shape from non-magnetic effects (most notably the slight angular deviation of the probe tip, as mentioned above), it is useful to examine the difference between various void dimensions under the influence of a magnetic field and the same dimension in the baseline non-magnetized case. Rather than the true measurement of the dust void in a particular dimension, the change due to the introduction of the magnetic field will be examined, isolating the field's effects. An example of this, once again using the 74 mTorr case, can be seen in Fig. (4-17).

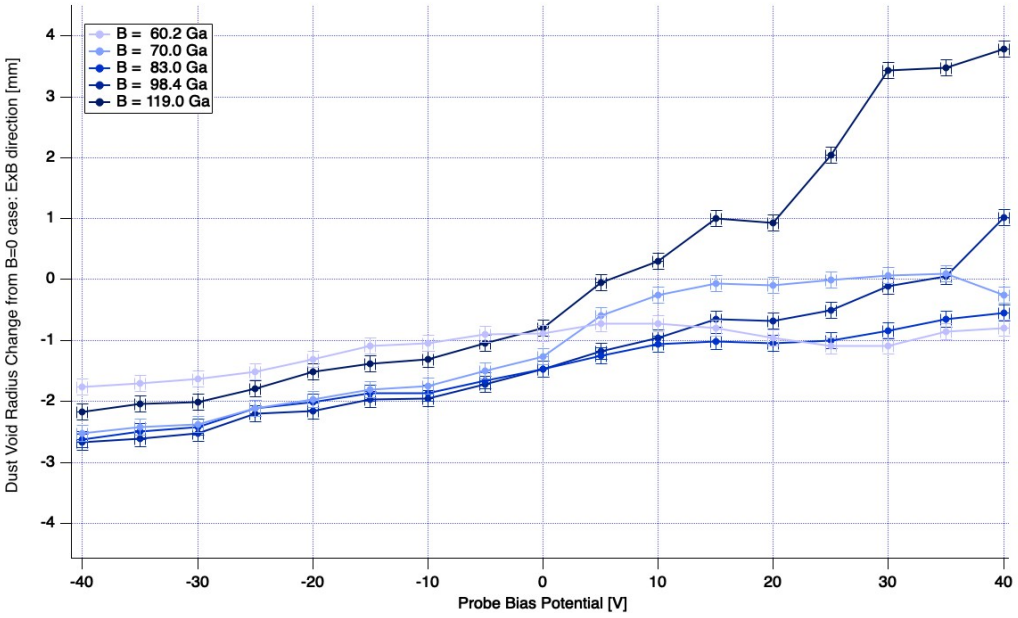

(a) - $\vec{E} \times \vec{B}$ direction

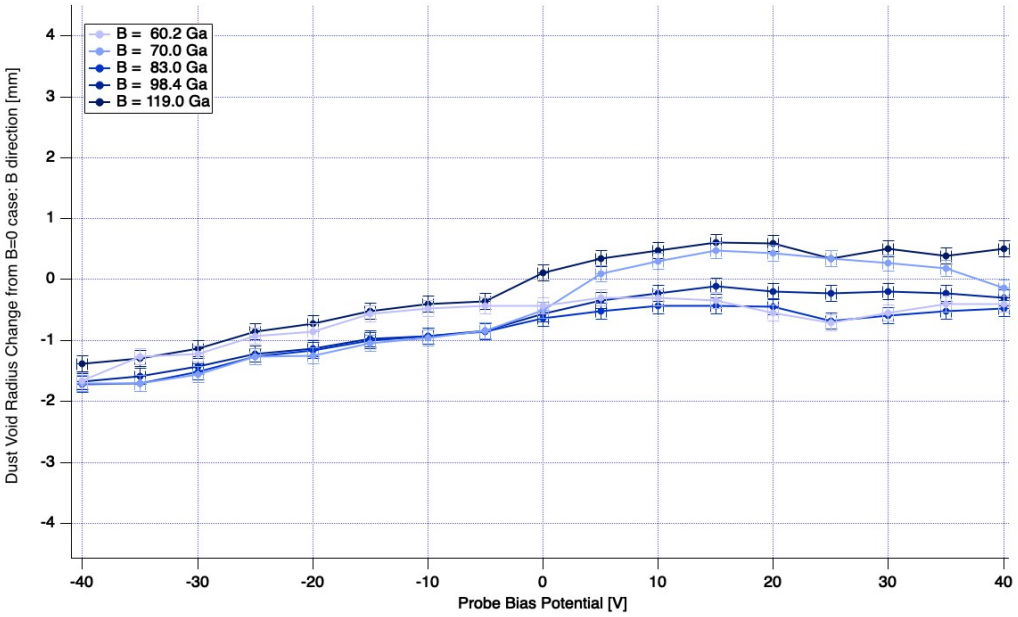

(b) - $\vec{B}$ direction

Figure 4-17: Change in dust void radial dimension with application of external magnetic field (74 mTorr background pressure). As was noted previously, the dust void boundary moves substantially farther away from the probe tip when it is positively biased in the $\vec{E} \times \vec{B}$ direction, while varying by no more than ±0.5 mm in the dimension parallel to the magnetic field. By examining the change relative to the non-magnetized case, rather than the raw measurements, it is possible to isolate the effects of the magnetic field from baseline deformation effects.

Because the most significant deviations from the non-magnetized cases tend to happen at the most extreme values of the probe bias potential, those cases will be emphasized. An overview of the deviation from non-magnetized dust void dimensions across the three main background pressures can be seen in Fig. (4-18). To better sort the data in a way that is relevant across multiple cases, these values are plotted as a function of the ion Hall parameter.

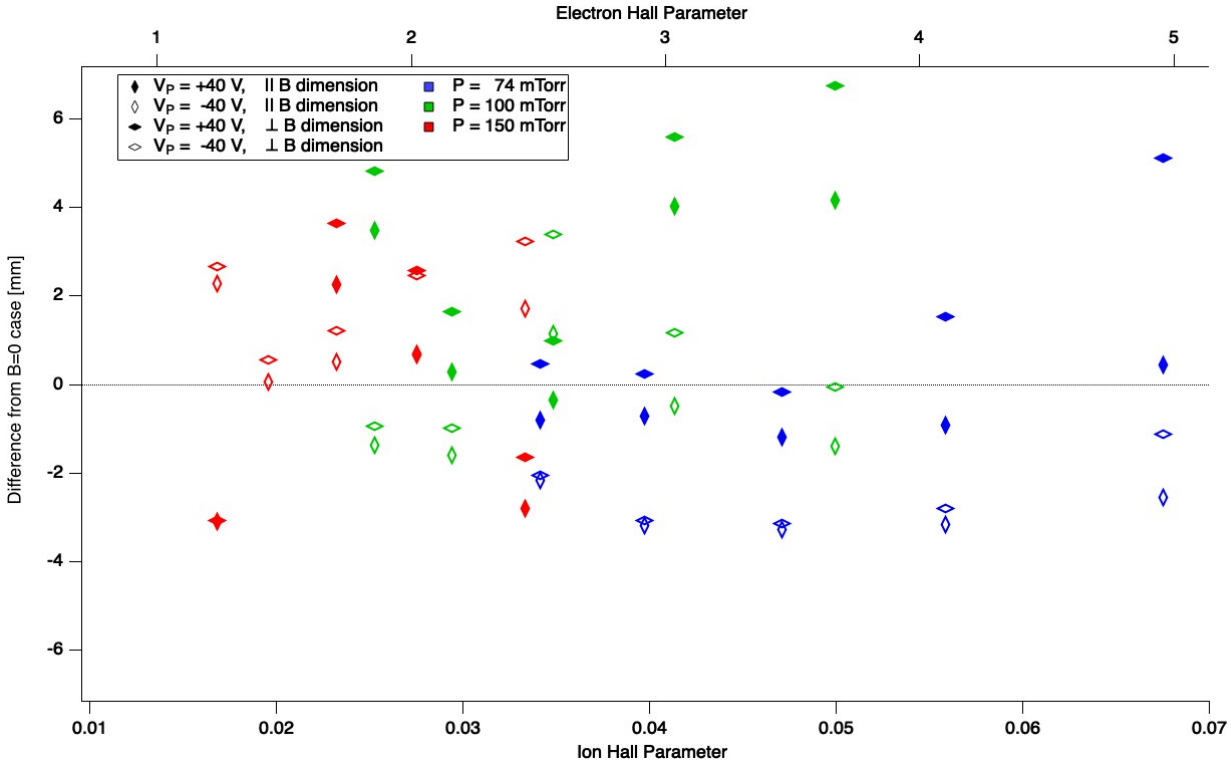

Figure 4-18: Deviation of the dust void diameter in the $\vec{B}$ and $\vec{E} \times \vec{B}$ dimensions as a function of ion and electron Hall parameter. Data is sorted both by neutral pressure (color) and probe bias potential (filled / unfilled markers). The trends are visually clear in the 74 mTorr case, but much less so in the more neutral-dominated 150 mTorr case. In particular, the deformity of the dust void, most extreme in the 74 mTorr, +40 V bias potential case, can be seen by the difference between the ∥ $\vec{B}$ and ⊥ $\vec{B}$ markers at the same neutral pressure and magnetic field strength (indicated by the ion Hall parameter, in this figure).

Examining Fig. (4-18), several trends are immediately clear. The deformity of the void's shape is evident by the difference between the $\parallel \vec{B}$ (or $\vec{B}$) direction's value and that of the $\perp \vec{B}$ (or $\vec{E} \times \vec{B}$) value. This deformity is typically larger for the cases in which the probe is positively biased, when the void's boundary is largely determined by the ion flow and therefore is most susceptible to the effects of the partial magnetization of the ions. Notably, in every single case, the void's deviation in the $\vec{E} \times \vec{B}$ direction is larger than in the $\vec{B}$ direction, confirming that the ions are flowing preferentially in the $\perp \vec{B}$ direction at these magnetic field values. It is likely that were this apparatus capable of creating dust voids at much higher magnetic field values, there would be a shift in the opposite direction when the ion Hall parameter approached unity and the ions became tightly confined to magnetic field lines, giving them preferential drift in the direction parallel to $\vec{B}$. At these fields, however, the ion gyroradii are still large enough that the ion gyromotion is large compared to the other physical length scales (e.g., collision mean free path, Debye length, void dimension, etc.) of the system. (see Table 3).

Magnetic Field	Ion Gyroradius
B = 60.2 Ga	$r_{L,i} = 27.0$ mm
B = 70.0 Ga	$r_{L,i} = 23.2$ mm
B = 83.0 Ga	$r_{L,i} = 19.7$ mm
B = 98.4 Ga	$r_{L,i} = 13.6$ mm
B = 119.0 Ga	$r_{L,i} = 11.2$ mm

Table 3: Ion gyroradius associated with the magnetic field values used in this experiment. Calculated assuming ions at room temperature, i.e. $T_i = {}^{1}/_{40}$ eV. Because the absolute largest voids measured in this experiment have a diameter on the order of the smallest ion gyroradius, there is no measureable effect of ions becoming partially magnetized to the point of preferring drifts in the $\parallel \vec{B}$ direction. This would likely not be observable until the ion gyroradius was small enough that the characteristic length of the system was on the order of several gyro-orbits.

Also noteworthy in Fig. (4-18) is the effect of neutral collisions on the system. When the background pressure is higher, the magnetic field's effects are not so pronounced, and the trend in the measurements is not as clear as at lower pressures, even across similar values of the ion Hall parameter (which is meant to account for the effect of neutral collisions). With decreasing neutral pressure (and increasing ion and electron Hall parameter), even in the presence of a weakly magnetized plasma, the effect of on the void dimensions is still observable. In particular, for the 74 mTorr case, it becomes clear that there is a deviation in the spatial properties of the void parallel and perpendicular to the magnetic field even at modest magnetic fields. This is potentially of interest because even though the voids are believed to driven by ion flows, even weakly magnetized ions and electrons have an impact on the dimensions of the void.

5. Discussion

In order to properly analyze the results of these experiments and their relation to previously established theory of dust voids, a distinction must first be made regarding the unique parameter space of these dust voids and their background plasmas, as well as the experimental configuration, and the way that these conditions allow us to examine multiple models of dust voids within the same experiment.

a. No Magnetic Field

As described in Ch. 2, Avinash (along with Thomas and Merlino) modeled probe-induced dust voids for a probe that was negatively biased relative to the surrounding plasma. This established a radially inward electric field (i.e, towards the probe) that exerted an outward force on the negatively biased dust grains and an inward ion drag force that pulled ions towards the probe.[59]

By contrast, work by Goree and other authors described "self-induced" voids driven by a central positive potential (due to a local accumulation of positive charge), which created an

attractive Coulomb force on the dust grains, opposed by an outward stream of ions.[74] To date, every published account of dust voids in a plasma falls squarely into one of these two archetypes: ion-collecting (Avinash) voids, driven by a central potential which is negative relative to the surrounding plasma; or ion-source (Goree) voids, with a positive central potential.

It is significant to note that in both models, ion-collecting and ion-source, the void exists primarily due to two opposing forces (Coulomb and ion drag), and these forces are fundamentally opposed due to the fact that the dust grains and ions have charges of opposite sign. If the Coulomb force on the dust is one direction, the ions are being streamed in the other direction. Therefore, there will exist a radial distance from the center at which $F_E = -F_{id}$, which defines the boundary of the dust void.

In previous publications regarding dust voids, the voids have been able to exist only in one of these two modes. In all studies of self-induced dust voids[21,43,51,53], the Goree model applies, as they are driven exclusively by local concentrations of positive charges in a region within the plasma bulk. To the best of our knowledge, there have been no experiments proposed or carried out which would examine a self-induced dust void created by means of a negative potential.

In probe-induced void studies, only ion-collecting voids have been observed, for a variety of reasons. In some cases (for instance, in microgravity experiments), the researchers were careful to keep the probe bias negative relative to the space potential, because the risk of dust deposition on the probe tip would have been excessively harmful to the experimental apparatus, with no realistic means to clean or replace it.[58] In experiments in which a void was induced in an earth-based dust cloud, the additional force of gravity on the grains in the direction of the probe tip would be enough to collapse the void before crossing the space potential and entering the regime of ion-source voids.[59] When Bailung et. al. created probe-induced voids in dust monolayers, their voids were

consistently observed to collapse as the probe tip reach the space potential, keeping them restricted to the regime of ion-collecting voids.[60] Without further information regarding their experimental conditions, it is not completely clear why this was the case. It is likely that the vertical arrangement of their rf electrodes caused the bulk of ionization to occur higher than the dust grains, which were levitated in the sheath above the lower electrode. As a result, there may not have been a sufficient ion population within the area of the void to counter the electrostatic force drawing the dust grains in.

Because the plasma generation in the 3DPX chamber was arranged horizontally rather than vertically, with the midpoint between the rf electrodes lying well within the void region, there may have been sufficient plasma production in the immediate region of the dust voids to observe both ion-collecting and ion-source dust voids, driven by a probe biased either positively or negatively with respect to the space potential. A sample plot of dust void (average) radius with these regions specified can be seen in Fig. (4-19).

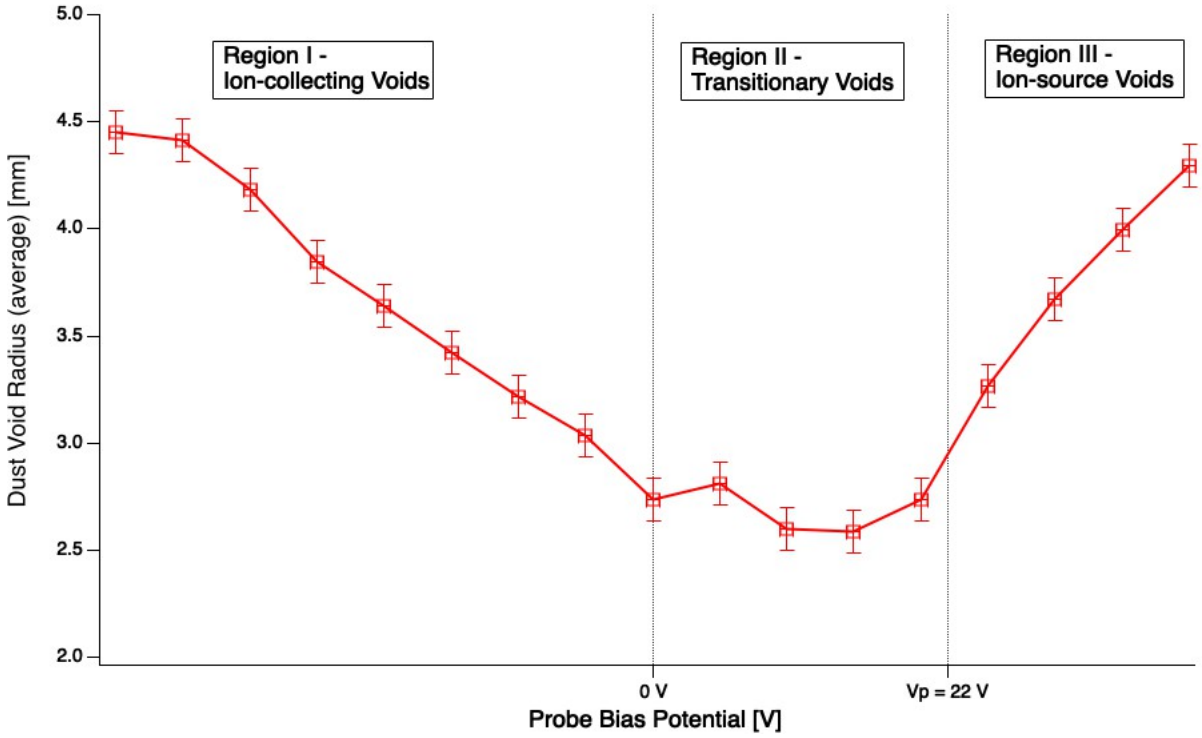

Figure 4-19: Average dust void radius vs. probe bias potential for dust voids formed at 74 mTorr of neutral pressure, with no external magnetic field. The three relevant regions of dust void mechanics are marked, along with their approximate cutoff potentials. Region I – Ion-collecting Voids, is the region in which the voids are driven by an outward Coulomb force, countered by an inward drag force by ions being collected by the probe tip. Region III – Ion-source Voids, is the region in which the voids are driven by the outward drag force due to ions streaming away from the probe tip, countered by the inward Coulomb attraction between the dust grains and the probe tip. Region II – Transitionary Voids, is the regime in between these two different dust void models, in which the directions of the dominant forces reverse.

Region I, which corresponds generally to voids for which the probe bias potential $V_B < 0\ V$, is the regime of ion-collecting voids. These can be thought of as the "typical" probe-induced dust voids, and behave very similarly to previously published probe-induced voids.[58–60] The dust grains are kept outside of the void region via Coulomb repulsion, opposed by the drag force of inward-streaming ions being collected by the probe tip. The electric potential structure between the probe

tip and the void boundary can be found by solving the Avinash Equation (Eq. 2-9), which allows for theoretical values of dust void radius to be calculated for given probe bias potentials.

$$\varphi''(r) + \frac{en_{i0}}{\varepsilon_0}\left(\frac{E_0}{|\varphi'(r)|} - \frac{n_{e0}}{n_{io}} e^{e\varphi(r)/kT_e}\right) = 0 \tag{2-9}$$

The solution to the Avinash Equation was calculated using plasma parameters as measured by the Langmuir probe (see Table 1). The dust charge Q_D was calculated using the dust charging model presented in Section (1-3 (b)), using the electron temperatures measured by the Langmuir probe. The dust grain charges used as calculated were:

$$74 \text{ mTorr} : Z = 18849\, e$$

$$100 \text{ mTorr} : Z = 20865\, e$$

$$150 \text{ mTorr} : Z = 22111\, e$$

The ratio of electron to ion densities in the void region was taken to be unity (via the quasi-neutrality condition Eqn. (1-2), and was estimated to be 0.9 in the dust region, due to electron depletion by dust grains.

The radial ion drift velocity u_i was calculated from the current as measured by the Langmuir probe in the Region I dust voids (I_P) using Eqn. (2-4). With the ion drift velocity, the force balance equation $F_E = F_D$ could be solved, and the radial electric field at the void boundary was calculated as:

$$E_0 = F_D(u_i)/Q_D \tag{4-1}$$

For probe currents in the range of 0.5-2.0 μA, this yielded a radial electric field at the void boundary of ~800-3800 V/m across all cases.

The experimental results within Region I, for data without an external magnetic field, are shown in Fig. (4-20), as compared with the numerical solution to the Avinash Equation (Eq. 2-9).

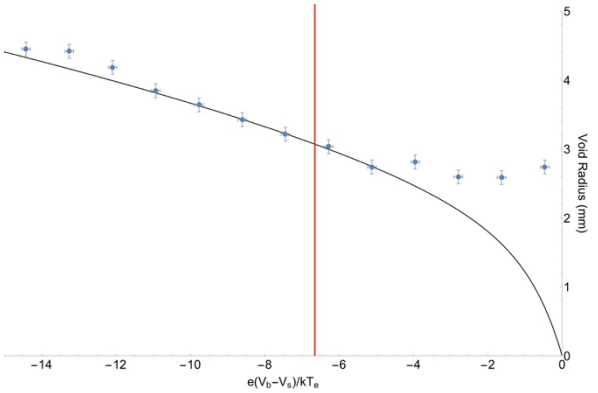

(a) – 74 mTorr

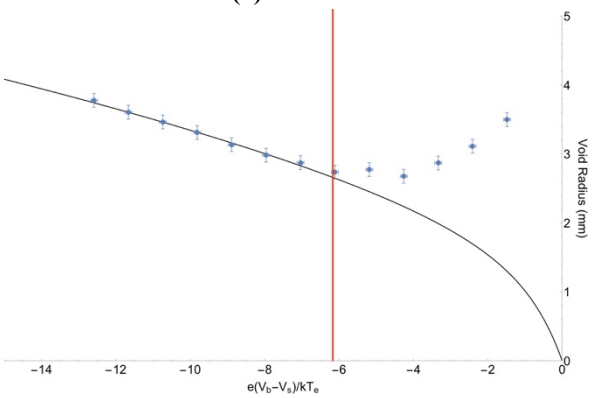

(b) – 100 mTorr

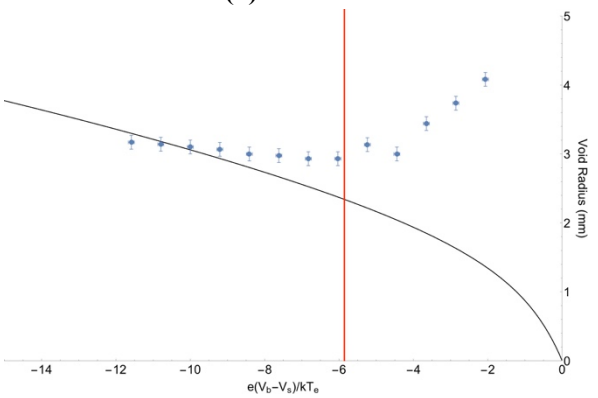

(c)– 150 mTorr

Figure 4-20: Void radius results plotted vs the Avinash Equation (Eq. 2-9). The vertical red line in each graph indicates the point at which the probe bias potential is equal to the floating potential $V_b = V_f$, when the results diverge from the theory and the dust voids enter the region of Transitionary Voids. Plasma parameters used, as measured by Langmuir probe (Table 1): (a) - $T_e = 4.3\ eV$, $n_0 = 4.9 \times 10^{15} m^{-3}$, $V_P = 22\ V$, $V_F = -9\ V$. (b) - $T_e = 5.4\ eV$, $n_0 = 4.92 \times 10^{15} m^{-3}$, $V_P = 28\ V$, $V_F = -5\ V$. (c) - $T_e = 6.3\ eV$, $n_0 = 5.25 \times 10^{15} m^{-3}$, $V_P = 33\ V$, $V_F = -3\ V$.

To illustrate the difference between this experimental geometry, in which the rf electrodes are arranged horizontally, and more traditional geometries with vertically arranged electrodes, a sample of processed data from a previous dust void experiment carried out on the Magnetized Dusty Plasma Experiment (MDPX) is shown in Fig. (4-21). For more on this, see Section 4-4.

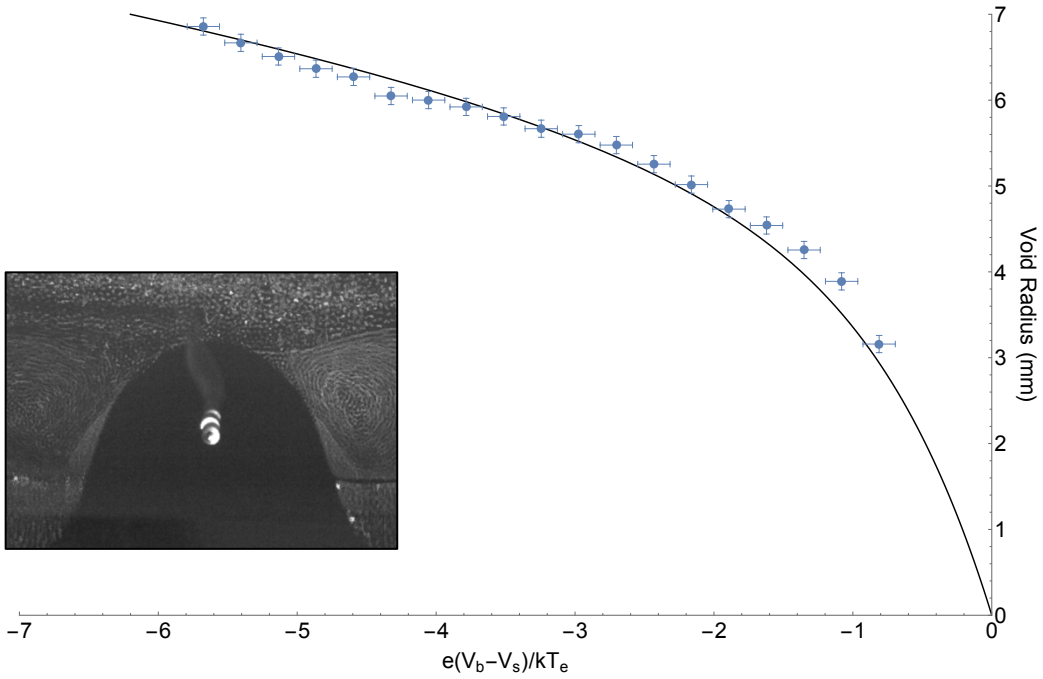

Figure 4-21: Sample from a previously conducted dust void investigation on the MDPX device. The experimental parameters were $V_s = 35\ V, T_e = 3.4\ eV, P = 95\ mTorr$, and the voids were created using dust grains that were 2 μm in diameter. As opposed to the new results presented in this work, the MDPX data was collected in a plasma generated with vertically arranged rf electrodes. As a result, the bulk of ionization occurred several centimeters above the dust void, as the grains were levitating on the sheath of the lower electrode. The dust void in this scenario collapsed as the probe bias potential approached the plasma potential, as in the probe-induced dust voids of previous publications. This system is capable of producing ion-collecting dust voids only, as there is not a sufficient repopulation of ions within the region of the dust void to create an ion-source dust void. Inset: Sample image of a dust void created in this experimental configuration.

In order to account for the ion-source mode of the dust voids observed in 3DPX, a modified version of the Avinash model must be applied. By inverting the directions of the ion velocity and setting the reference point for the potentials to $V_b = 0$, Eq. (2-9) can be solved numerically for dust voids operating in the ion-source mode. The full dust void results plotted against both the ion-source and ion-collecting regimes is shown in Fig. (4-22).

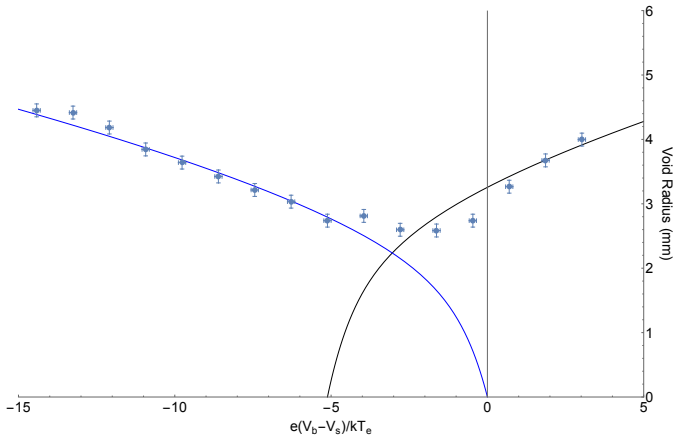

P = 74 mTorr

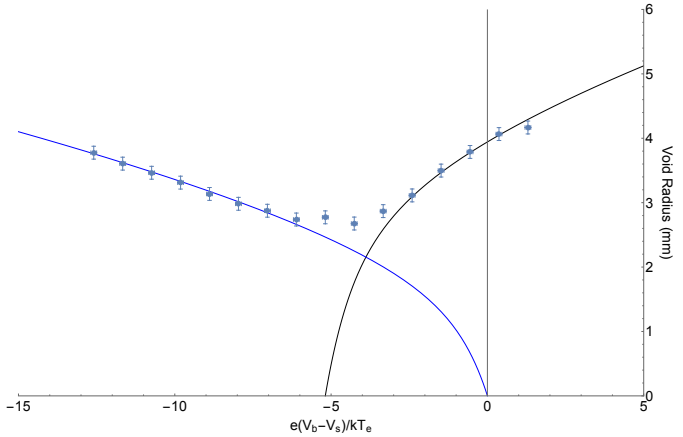

P = 100 mTorr

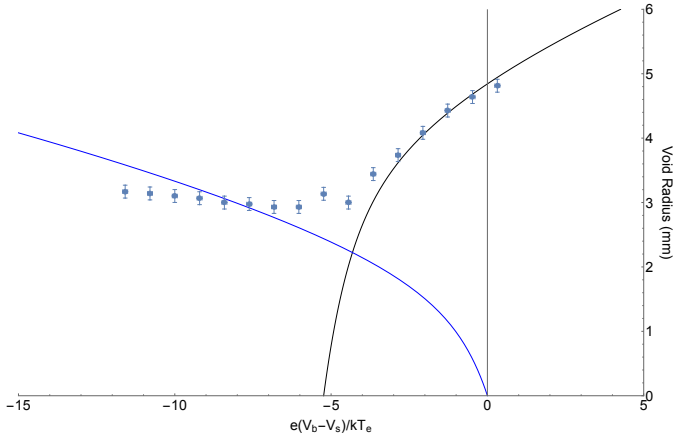

P = 150 mTorr

Figure 4-22: Dust void (average) radius plotted vs theory curves for both ion-collecting (in blue) and ion-source (in black) modes of the Avinash Model. The curves are generated by numerically solving the Avinash Equation (Eq 2-9). By solving for both modes of dust voids, the experimental results can be fully reconciled with the force balance which drives the dust voids, at all values of V_b. Plasma parameters used in these plots are the same as in Figure (4-20), as measured by Langmuir probe (Table 1).

The ion drift velocities for the dust voids, in both the ion-collecting and ion-source modes, can be estimated based on the fits of the measured void radii to the Avinash model in Regions I and III. The dust grain charge in each case is calculated as described in Chapter 1, Section 3 (b), using the electron temperature values measured with the Langmuir probe in Section 1 of this chapter. It is assumed that the ion drift velocity is constant as a function of probe voltage in Regions I and III. This is a reasonable assumption, given that the ion current to a Langmuir probe is known to reach the ion saturation current at relatively small probe voltages.[68,75] The ion drift velocity is directed inwards toward the probe tip in Region I, and outwards away from the probe in Region III. Within the Transitionary Region, there is no reliable way to calculate ion drift velocities at a given probe voltage, but it is a reasonable approximation that the drift velocity is small because in this region the probe is at a potential that is close to the local plasma potential. This means there would be no electric field to drive a flow of ions. The estimated ion drift velocities in Regions I and III for each of the three neutral pressure cases, as well as their relative scale as compared to the Bohm velocity and ion thermal speed, are shown in Table 4.

	Region I – Ion-collecting Mode			Region III – Ion-source Mode		
Pressure	u_i	u_i/v_{Bohm}	$u_i/v_{th,i}$	u_i	u_i/v_{Bohm}	$u_i/v_{th,i}$
74 mTorr	145 m/s	0.045	0.370	125 m/s	0.039	0.319
100 mTorr	290 m/s	0.080	0.740	205 m/s	0.057	0.523
150 mTorr	350 m/s	0.090	0.893	200 m/s	0.051	0.510

Table 4: Estimated drift velocities for both ion-collecting and ion-source modes of probe-induced dust voids. The drifts are well below the Bohm velocity, indicating that they are subsonic. Note that the ion drift velocity is directed radially inwards, toward the probe tip, in Region I, and is directed outwards away from the probe tip in Region III.

By examining the positions of the dust void boundaries, it is thus possible to extract ion flow information from the dusty plasma system. The drift velocities are well below the local sound speed, so the Barnes model of the ion drag force is physically valid.

b. Magnetic Field Influence on Dust Grain Charge

To estimate the effect of the magnetic field on the electric charge of the dust grains, the ion drift velocities found in the non-magnetized cases will be utilized. With the external magnetic field applied to the dust voids, the void dimension was observed to change much more significantly in the dimension perpendicular to the magnetic field than parallel to the field.

It will be taken as an assumption that the ion and electron drifts in the direction parallel to the field ($\vec{u}_{i,e\,||}$) do not change in the presence of the magnetic field, and the non-magnetized velocity results are valid along the axis of the chamber. Using the dust charge calculation method as explained in Section (1-3 (b)), the non-magnetized dust charge is found, and used as a baseline for the magnetized cases.

As was described in Section (2-3), it has been suggested recently by Kodanova et. al. that externally applied magnetic fields can decreased the net charge accumulated on the surface of a dust grain, specifically by magnetizing the electrons and lowering their effective cross-section with the dust.[14] This is consistent with the findings above, as the dust voids under the influence of the external magnetic field were observed to be smaller than non-magnetized voids in the ion-collecting mode, in which the electrostatic force on the dust grain is repulsive. As the dust grain charge lowers, this outward force decreases, and the ion drag force moves the dust grains closer to the probe tip, as can be seen in Figures (4-12), (4-13), and (4-17). In the ion-stream mode, the dust electrostatic force is inward, and indeed these voids were seen to grow as the magnetic field increased, consistent once again with a smaller dust charge.

Using the Avinash model and the previously stated assumption that the ion and electron velocity parallel to the magnetic field are unchanged, the dust grain charge at each magnetic field and neutral pressure can be estimated. The background plasma parameters (ion and electron

temperature, density, space and floating potentials) are taken to be fixed across magnetic field values, held to the same values as were previously listed in Figure (4-21). These results are presented in Figure 4-23, as a fraction of the baseline (non-magnetized) dust charge.

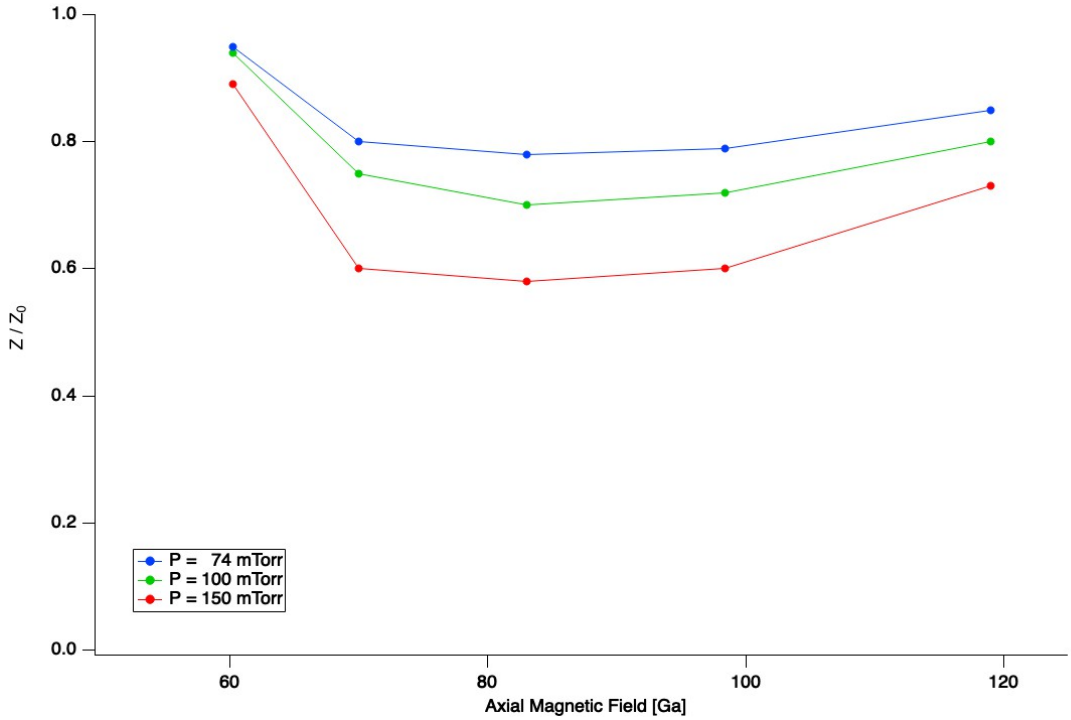

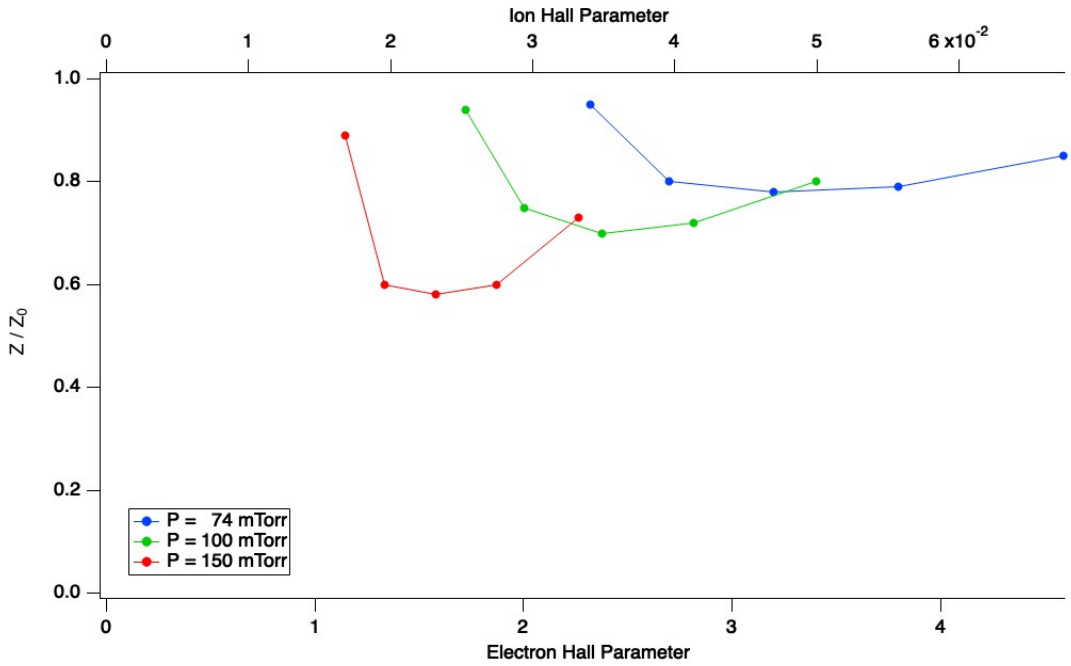

Figure 4-23: Calculated decrease in dust grain charge, as a function of the externally applied magnetic field (above) and the ion and electron Hall parameters (below). Even at relatively low fields, the reduction is significant. The effect seems to increase with neutral pressure.

While Kodanova et. al. predicted that the magnetization of the electron population would lead to decreased net electric charge of the dust grains, the charge losses seen here are somewhat larger than their calculations suggested at these magnetic field levels. The simulations presented by Kodanova et. al. for 4 μm radius dust grains predicted a charge loss of only 0.4% at magnetic fields as high as 1000 Ga, and at similar densities to those presented here.[14] However, their simulation assumed an electron temperature of only 1 eV, whereas the experiments here were carried out with electron temperatures in the 4-6 eV range. As a result, Kodanova's dust grains were assumed to have a baseline, non-magnetized charge of only ~8000 electron charges, significantly lower than the dust grains here which carry charges around 20,000 electron charges. This lower baseline dust grain charge may have been less susceptible to small changes in the magnetic field strength. It is also possible that the relatively small volume of plasma in these experiments, especially in the region with dust, reduced the available electron population to be collected by the dust grains.

c. Dust Void Deformation Effects

As shown above, the shape of the dust voids becomes consistently elongated in the $\perp \vec{B}$ direction as the magnetic field is increased. While it was hypothesized prior to these experiments that this effect or one similar may happen as a result of the magnetization of the ion population, the ion Hall parameter remained quite low even at the highest magnetic field values investigated. The asymmetry of the ion drag force as a result of the magnetization of the ion population is therefore eliminated as an explanation for this deforming effect of the dust voids.

It is much more likely that the effect is a result of an electron $\vec{E} \times \vec{B}$ drift in conjunction with the geometry of the rf sheath. It has long been known in the dusty plasma community that the sheath upon which dust grains tend to levitate in rf plasma systems is rarely flat, but usually has a parabolic shape. This is the result of several factors, including a density gradient as ionization occurs in the center of the plasma volume, as well as the geometry of the conducting surfaces used to confine dust grains.[50] A rough illustration of a parabolic rf sheath in this experiment is shown in Figure 4-24.

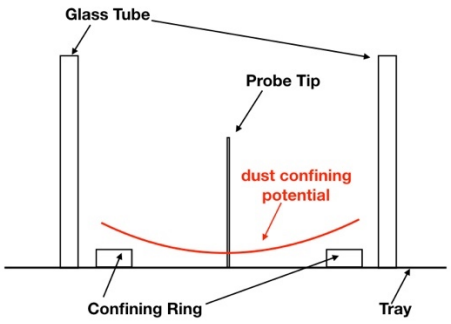

Figure 4-24: Rough illustration of the shape of a typical rf sheath, within the plasma generation apparatus used in these experiments. Rf sheaths tend to be parabolic, due to plasma density gradients as well as the geometry of the system. In particular, the confining ring creates an electrostatic potential well, allowing dust grains to be confined as they levitate on the rf sheath.

The geometry of the electric and magnetic fields in the system are also significant here. While the direction of the magnetic field $\vec{B}$ remains the same between experiments, the direction of the radial electric field due to the probe bias $\overrightarrow{E_b}$ does not. Specifically, it changes directions as the probe's bias is stepped from negative to positive values, relative to ground. An illustration of the directions of these fields, as well as the resultant $\vec{E} \times \vec{B}$ drift, is shown in Figure 4-25.

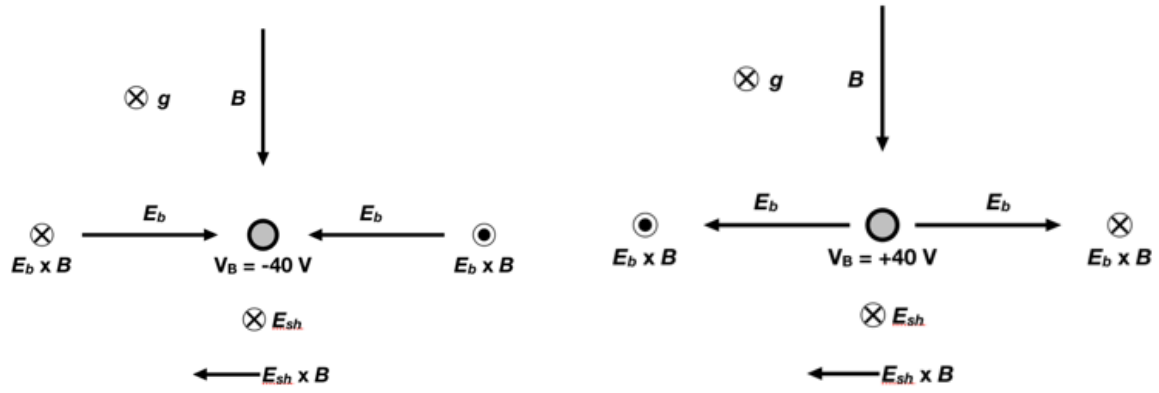

Figure 4-25: Vector directions of the magnetic field ($\vec{B}$), probe electric field ($\vec{E}$), and resultant $\vec{E} \times \vec{B}$ drift for both a negatively and positively biased probe tip. Viewpoint in both images is top-down (gravity into the page) and aligns with the viewing angle in the frame of all videos / images of dust voids presented in this chapter. Even though the magnetic field direction is constant, by changing the bias on the probe tip, the resultant $\vec{E} \times \vec{B}$ drifts on both sides of the experimental area reverse direction.

Because the $\vec{E} \times \vec{B}$ drift in a plasma has the same direction no matter the sign of a particle's charge, the electrons, ions, and dust grains all experience drifts in the same direction. While this is unlikely to directly move the dust grains any significant amount, the drifts of local ion and electron densities have been known to shift dust grains with them, as the plasma potential moves slightly from the dust equilibrium position.[76] By moving the dust grains slightly up or down, their equilibrium levitation along the sheath will also shift laterally along the confining potential well. Specifically, a downward $\vec{E} \times \vec{B}$ shift would correspond to the dust void boundary moving radially inward (the void dimension decreasing), while an upward $\vec{E} \times \vec{B}$ shift would cause outward movement of the void radius. As the magnetic field is increased, this would translate to a generally rightward shift (within the frame of the dust void videos) for negatively biased probe tips, and leftward for positively biased probe tips. This is consistent with the observed shifts in the void boundaries from the non-magnetized cases, as shown in Figure 4-16.

In the parallel and anti-parallel directions relative to the magnetic field, the $\vec{E} \times \vec{B}$ term goes to zero, and accordingly there is far less of a change in the dust void dimension in these directions as the magnetic field is increased (again see Figure 4-16). As Figure 4-18 illustrates, the dust void dimensions consistently change much more dramatically in the directions perpendicular to the magnetic field vector, where the $\vec{E} \times \vec{B}$ term is at a maximum.

While it was hoped at the outset of these experiments to observe the direct effect of ion magnetization on dust void shape via the ion drag force, unfortunately the magnetic fields were not high enough (nor the neutral pressures low enough) to reach such a regime. However, the applied magnetic field was still observed to significantly alter the shape of the dust voids. It is possible that future work at Auburn University would be able to measure directly the magnetization of the ion drag force within a dust void system (see Chapter 5).

6. Attempted Dust Void Experiments in Highly Magnetized Plasmas

While the magnetic field strengths, and associated electron and ion Hall parameters, are limited to the weakly magnetized regime on the 3DPX chamber, an experiment was attempted which would have generated similar dust voids in the highly magnetized environment of Auburn's Magnetized Dusty Plasma Experiment (MDPX). The centerpiece of the MDPX device is the set of four superconducting magnetic coils, which are capable of producing steady state magnetic fields of up to 4 T (over 300 times larger than the strongest magnetic field presented in this dissertation from the 3DPX chamber).

The voids created in the MDPX chamber were probe-induced and were limited to the ion-collecting mode of dust voids. In non-magnetized cases, voids were produced both in vertically-oriented 3-dimensional dust clouds (similar to those produced by Thomas et. al.[59]) and in 2-

dimensional dust monolayers, similar to those described by Bailung et. al.[60], as well as described in this dissertation. Examples of both varieties of dust voids are shown in Figure 4-26.

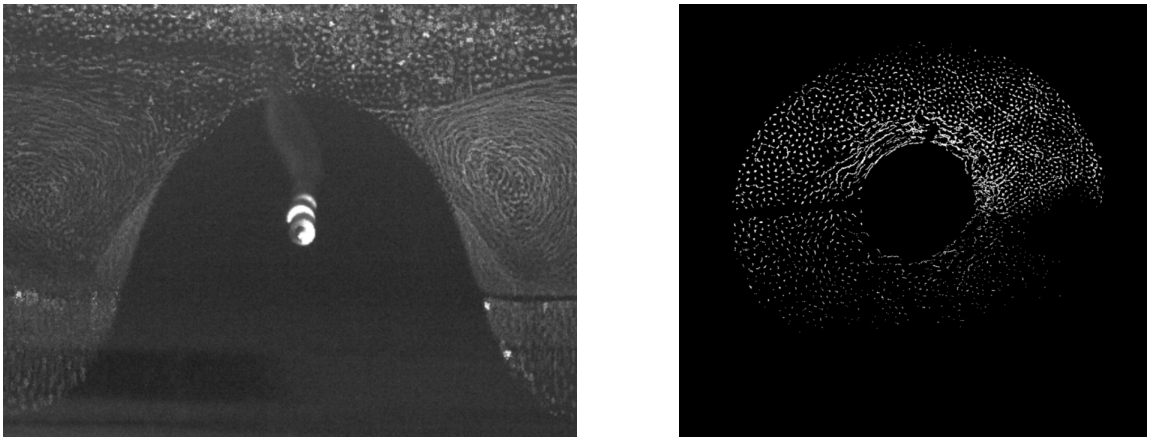

(a) **(b)**

Figure 4-26: Non-magnetized dust voids produced in the MDPX device. Both voids here are probe-induced and ion-collecting. Both experiments demonstrated behavior consistent with the Avinash model for ion-collecting dust voids, ie a decrease in void size as the probe bias potential approaches the plasma space potential from more negative values. (a) A vertically oriented void in a 3-dimensional dust cloud. The rf electrodes were arranged vertically, with the upper electrode powered and the lower electrode grounded. Due to the experimental geometry as the dust levitated in the rf sheath region, dust fully encircling the probe tip was not observed. (b) A horizontally oriented void in a 2-dimensional monolayer.

With the magnetic fields attainable on the MDPX device, it was hoped that the dust voids would be observed under conditions in which the electrons and even the ions were very highly magnetized. Under typical MDPX level magnetic fields, the ion Hall parameter can reach values of 10-20, at which point the ion trajectories are significantly altered. The effects this would have on the dust void shape would be of great interest.

Unfortunately the MDPX-based experiments ran into several difficulties. Many were technical, but there were physical hurdles as well which still must be solved. At magnetic fields of the level produced in MDPX, filament production is a constant concern. The formation of plasma filaments can prohibit dust grains from occupying large regions of the plasma environment. The MDPX

device is also configured with a vertically oriented rf plasma generation system, which, as explained above, can introduce several difficulties in the confinement of dust voids. Finally, the effect of the high magnetic field on dust grain charge, while of great investigative interest, is still not fully understood, and the dust grains were much more difficult to confine in the plasma environment with their apparently greatly lowered electric charges.

One tentative result that was found under high magnetic field conditions on MDPX was the creation of “notch” structures at the top of vertically aligned dust voids. At high fields, the radial dust void dimension in most directions was observed to decrease significantly, likely indicating a decrease in the dust electric charge. Directly above the probe tip, however, in alignment with both the magnetic field and the earth’s gravity, the dust voids resisted this shrinking effect, forming a notch-like shape. An example of such a “notch” can be seen in Figure 4-27.

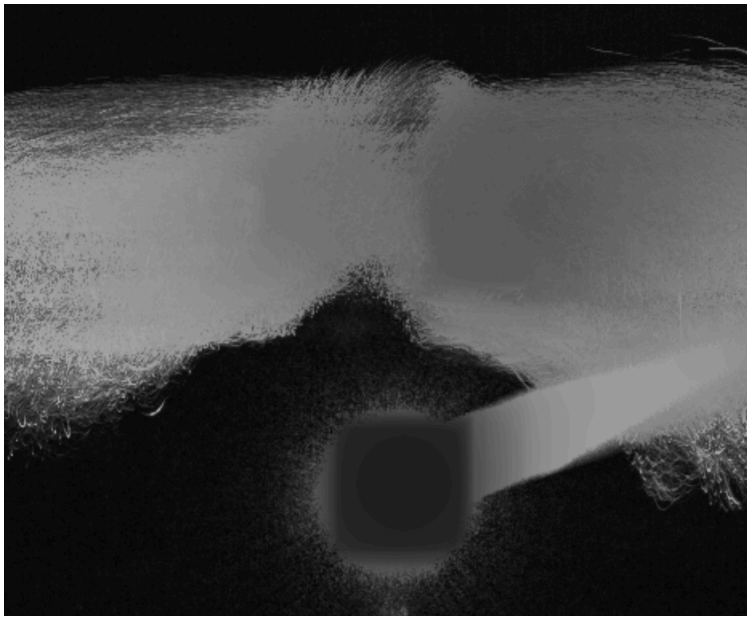

Figure 4-27: A vertically aligned dust void in the MDPX device under high magnetic field. This image was taken at a neutral pressure of 116 mTorr, under 1.8 W of rf power, with a probe bias voltage of -20 V, and under the influence of a 2.0 T magnetic field, oriented straight downward. The "notch" structure is seen at the top of the dust void, visually represented as a rounded protrusion into the region occupied by the dust grains.

Further experiments are necessary before any definitive statements can be made regarding the nature or behavior of these "notch" structures or the physical processes which may cause them to form.

Chapter 5 - Summary and Conclusion

This work was performed at the Auburn University Magnetized Plasma Research Laboratory (MPRL) within the Three-dimensional Dusty Plasma Experiment (3DPX) chamber. To conduct the experiments described in this dissertation, a novel apparatus for creating dust voids within a radio frequency plasma was developed. An ImageJ program was also written to programmatically process large amounts of videographic data and extract physical measurements for the purpose of mathematical analysis.

1. Summary of Experiments

Probe-induced dust voids were created both with and without an externally applied magnetic field. These voids are maintained by an equilibrium of opposing forces, namely an electrostatic force between the negatively charged dust grains and the probe tip, and a drag force created by ions streaming past the dust grains. Dust voids can operate in two separate modes, ion-collecting and ion-streaming, based on the relative bias of the probe tip to the surrounding plasma environment. Because of the specific configuration of the void-creating probe tip and the rf electrodes used to generate the plasma, dust voids were observed operating in both ion-collecting and ion-streaming modes, as well as a transitionary mode between the two, a behavior never before observed in dust voids of any variety.

By comparing the dust voids as observed with the physical model laid out by Avinash[59], ion drift velocities were estimated from the videographic dust void data. The ion drifts were found to be sub-thermal and significantly sub-sonic in nature.

When an external magnetic field was applied, the dust voids were observed to distort in two primary ways. The first was an elongation of the voids in the direction perpendicular to the applied magnetic field. The second was a physical shift of the center of the dust voids away from the probe

tip which was driving them, which occurred in both the directions parallel and perpendicular to the applied magnetic field, but more significantly in the perpendicular direction.

By comparing the void dimensions with and without a magnetic field (specifically in the direction parallel to the magnetic field, in which the ion drift velocity would be largely unchanged), the change in the net electric charge on the dust grains was calculated as a function of the magnetic field, as well as the ion and electron Hall parameters.

Also, while the magnetization of the ions was not attainable within the parameters of these experiments, a deformation of the dust void shape due to the influence of the magnetic field was measured. This effect was caused by the general $\vec{E} \times \vec{B}$ shift of plasma species within the geometry of the dust confining potential of the rf sheath.

2. Future Work

There remain many outstanding questions and potential avenues for investigation regarding dust voids, both with and without an externally applied magnetic field. This investigation was the first to record dust voids in the same experimental apparatus moving between ion-collecting and ion-source modes, but the same effect could possibly be observed in other configurations. With the proper arrangement of rf electrodes, it is likely that a similar transition between these two modes of dust void could be observed in a 3-dimensional dust cloud, either in a ground-based experiment or, perhaps more feasibly, in a microgravity environment.

The potential for significant research on dust voids within a magnetic field is vast, and the surface has only been barely scratched in this dissertation. The experiments described were performed in very weakly magnetized plasmas, but were originally designed to be performed on the Magnetized Dusty Plasma Experiment (MDPX), a device capable of reaching magnetic fields several orders of magnitude higher than those used in this work.[61,77] Due to unfortunate technical

hurdles, these plans were unable to be properly carried out. However, the potential physical regimes which might be reached if these technical challenges were solved are vast.

Because of the ability of the MDPX system to create magnetic fields both parallel and perpendicular to the Earth's gravitational field, multiple physical configurations of dust voids in strongly magnetized plasmas are possible. With the magnetic field aligned vertically over a dust void in a 2-dimensional monolayer, rotations of the dust void around the probe tip or extreme angles of tilting of the monolayer and void are possible. With the magnetic field aligned horizontally, so that the magnetic field vector lies in the plane of the dust void (as in the experiments described in this work), it would be possible to reach ion Larmor radii smaller than the diameter of the probe tip or the dust grains, and confine the ions tightly to magnetic field lines. This would undoubtedly cause dramatic changes in the shape and size of the dust void, and could reveal many details regarding the nature of both ions' and dust grains' responses to very large magnetic fields.

References

[1] W. Crookes, J. Franklin Inst. **108**, 305 (1879).

[2] J.J. Thomson, Philos. Mag. Sci. **90**, 25 (1897).

[3] H.M. Mott-Smith and I. Langmuir, Phys. Rev. **28**, 727 (1926).

[4] L. Tonks and I. Langmuir, Phys. Rev. **34**, 876 (1929).

[5] H. Mott-Smith, Nature **233**, 219 (1971).

[6] D. Mansuroglu, I.U. Uzun-Kaymak, and I. Rafatov, Phys. Plasmas **24**, 053503 (2017).

[7] F.F. Chen, *Introduction to Plasma Physics and Controlled Fusion* (1984).

[8] P.K. Shukla and A.A. Mamun, *Introduction to Dusty Plasma Physics* (CRC Press, 2001).

[9] A. Barkan, N. D'Angelo, and R.L. Merlino, (n.d.).

[10] X. Wang, J. Schwan, H.– W. Hsu, E. Grün, and M. Horányi, (n.d.).

[11] J. Goree, Plasma Sources Sci. Technol. **3**, 400 (1994).

[12] V.N. Tsytovich, N. Sato, and G.E. Morfill, New J. Phys. **5**, (2003).

[13] R. Mishra and M. Dey, IEEE Trans. Plasma Sci. **PP**, 1 (2018).

[14] S.K. Kodanova, N.K. Bastykova, T.S. Ramazanov, G.N. Nigmetova, S.A. Maiorov, and Z.A. Moldabekov, IEEE Trans. Plasma Sci. **PP**, 1 (2019).

[15] D. Law, W. Steel, B. Annaratone, and J. Allen, Phys. Rev. Lett. **80**, 4189 (1998).

[16] J. Carstensen, F. Greiner, and A. Piel, Phys. Rev. Lett. **109**, 1 (2012).

[17] G.I. Sukhinin, M. V. Sal'nikov, and A. V. Fedoseev, J. Appl. Mech. Tech. Phys. **59**, 818 (2018).

[18] W.J. Miloch, D. Darian, and M. Mortensen, (2017).

[19] J. Kong, T.W. Hyde, L. Matthews, K. Qiao, Z. Zhang, and A. Douglass, Phys. Rev. E - Stat. Nonlinear, Soft Matter Phys. **84**, 1 (2011).

[20] Y. Feng, J. Goree, and B. Liu, Phys. Rev. Lett. **109**, (2012).

[21] D. Samsonov and J. Goree, Phys. Rev. Lett. **59**, 1047 (1999).

[22] B. Zhang, J. Kong, M. Chen, K. Qiao, L.S. Matthews, and T.W. Hyde, (2017).

[23] E. Thomas, **93**, 1 (2017).

[24] T. Hall, E. Thomas, K. Avinash, R. Merlino, and M. Rosenberg, Phys. Plasmas **25**, 103702 (2018).

[25] O. V Kravchenko, O.A. Azarova, and T.A. Lapushkina, (2017).

[26] Z. Chen, X. Zhu, F. Huang, W. Gao, and O.V. Kravchenko, AIP Adv. **8**, 105021 (2018).

[27] L. Patacchini and I.H. Hutchinson, Plasma Phys. Control. Fusion **53**, 065023 (2011).

[28] P.K. Shukla, in *Dusty/Complex Plasmas Basic Interdiscip. Res.* (2011), pp. 11–24.

[29] N.N. Rao, P.K. Shukla, and M.Y. Yu, Planet. Space Sci. **38**, 543 (1990).

[30] A. Barkan and R.L. Merlino, Phys. Plasmas **2**, 3563 (1995).

[31] A. Thompson, C. O.; Barkan, Phys. Plasmas **4**, 042107 (1997).

[32] E. Thomas and J. Williams, Phys. Plasmas **13**, (2006).

[33] J.D. Williams, E. Thomas, and L. Marcus, Phys. Plasmas **15**, (2008).

[34] S. Jaiswal, M.Y. Pustylnik, S. Zhdanov, H.M. Thomas, A.M. Lipaev, A.D. Usachev, V.I. Molotkov, V.E. Fortov, M.H. Thoma, and O. V. Novitskii, 1 (2018).

[35] M. Horanyi, Phys. Plasmas **7**, 3847 (2000).

[36] S. Bose, M. Kaur, P.K. Chattopadhyay, J. Ghosh, E. Thomas, and Y.C. Saxena, J. Plasma Phys. **85**, 905850110 (2019).

[37] A.R. Abdirakhmanov, Z.A. Moldabekov, S.K. Kodanova, M.K. Dosbolayev, and T.S.

Ramazanov, IEEE Trans. Plasma Sci. **PP**, 1 (2019).

[38] P.K. Kaw, K. Nishikawa, and N. Sato, Phys. Plasmas **9**, 387 (2002).

[39] S. Jaiswal, P. Bandyopadhyay, and A. Sen, **020015**, 1 (2018).

[40] M. Rosenberg, Planet. Space Sci. **41**, 229 (1993).

[41] D. Winske, S.P. Gary, M.E. Jones, M. Rosenberg, V.W. Chow, and D.A. Mendis, Geophys. Res. Lett. **22**, 2069 (1995).

[42] K.N. Ostrikov, S. V. Vladimirov, M.Y. Yu, and G.E. Morfill, Phys. Rev. E. Stat. Phys. Plasmas. Fluids. Relat. Interdiscip. Topics **61**, 4315 (2000).

[43] M. Mikikian, L. Couëdel, M. Cavarroc, Y. Tessier, and L. Boufendi, New J. Phys. **9**, (2007).

[44] S. Bukhari, S. Ali, S.A. Khan, and J.T. Mendonca, J. Plasma Phys. **84**, 905840202 (2018).

[45] H.M. Thomas and G.E. Morfill, Nature **379**, 806 (1996).

[46] J. Vasut and T.W. Hyde, IEEE Trans. Plasma Sci. **29**, 231 (2001).

[47] F. Melandso, **55**, 7495 (1997).

[48] S. Jaiswal, T. Hall, S. LeBlanc, R. Mukherjee, and E. Thomas, Phys. Plasmas **24**, (2017).

[49] H. Ikezi, Phys. Fluids **29**, 1764 (1986).

[50] A. Piel, (n.d.).

[51] G. Praburam and J. Goree, Phys. Plasmas **3**, 1212 (1996).

[52] A. Melzer, A. Homann, A. Piel, V.A. Schweigert, and I. V. Schweigert, **167**, 167 (1998).

[53] G.E. Morfill, H.M. Thomas, U. Konopka, H. Rothermel, M. Zuzic, A. Ivlev, and J. Goree, Phys. Rev. Lett. **83**, 1 (1999).

[54] E. Thomas, B.M. Annaratone, G.E. Morfill, and H. Rothermel, Phys. Rev. E - Stat. Nonlinear, Soft Matter Phys. **66**, 1 (2002).

[55] A.P. Nefedov, G.E. Morfill, V.E. Fortov, H.M. Thomas, H. Rothermel, T. Hagl, V. Ivlev, M.

Zuzic, B.A. Klumov, A.M. Lipaev, V.I. Molotkov, O.F. Petrov, Y.P. Gidzenko, K. Krikalev, W. Shepherd, A.I. Ivanov, H. Binnenbruck, J.A. Goree, and Y.P. Semenov, New J. Phys. (2003).

[56] A. V Fedoseev, G.I. Sukhinin, M.K. Dosbolayev, and T.S. Ramazanov, Phys. Rev. E **92**, 1 (2015).

[57] R.P. Dahiya, G. V Paeva, W.W. Stoffels, E. Stoffels, G.M.W. Kroesen, K. Avinash, and A. Bhattacharjee, Phys. Rev. Lett. **89**, 125001 (2002).

[58] M. Klindworth, A. Piel, A. Melzer, U. Konopka, H. Rothermel, K. Tarantik, and G.E. Morfill, Phys. Rev. Lett. **93**, 1 (2004).

[59] E. Thomas, K. Avinash, and R.L. Merlino, Phys. Plasmas **11**, 1770 (2004).

[60] Y. Bailung, T. Deka, A. Boruah, S.K. Sharma, A.R. Pal, J. Chutia, and H. Bailung, Phys. Plasmas **25**, (2018).

[61] E. Thomas, U. Konopka, D. Artis, B. Lynch, S. Leblanc, S. Adams, R.L. Merlino, and M. Rosenberg, J. Plasma Phys. **81**, (2015).

[62] M. Puttscher, A. Melzer, U. Konopka, S. LeBlanc, B. Lynch, and E. Thomas, Phys. Plasmas **24**, (2017).

[63] B. Lynch, Microparticle Dynamics in Strongly Magnetized Low Temperature Plasmas, 2017.

[64] E. Thomas, J.D. Williams, and J. Silver, Phys. Plasmas **11**, (2004).

[65] J.D. Williams and E. Thomas, IEEE Trans. Plasma Sci. **35**, 303 (2007).

[66] R. Fisher and E. Thomas, IEEE Trans. Plasma Sci. **38**, 833 (2010).

[67] R.K. Fisher, Measurement of the Phase Space Distribution in a Complex Plasma, 2012.

[68] R.L. Merlino, Am. J. Phys. **75**, 1078 (2007).

[69] S.H. Lam, Phys. Fluids **8**, 73 (1965).

[70] E.P. Szuszczewicz and P.Z. Takacs, Phys. Fluids **22**, 2424 (1979).

[71] N.J. Miller, J. Geophys. Res. **77**, 2851 (1972).

[72] C.A. Schneider, W.S. Rasband, and K.W. Eliceiri, Nat. Methods **9**, 671 (2012).

[73] J. Schindelin, I. Arganda-Carreras, E. Frise, and E. Al., Nat. Methods **9**, 676 (2012).

[74] J. Goree, G.E. Morfill, V.N. Tsytovich, and S. V Vladimirov, Phys. Rev. E. Stat. Phys. Plasmas. Fluids. Relat. Interdiscip. Topics **59**, 7055 (1999).

[75] F.F. Chen, Phys. Plasmas **8**, 3029 (2001).

[76] E. Thomas, Contrib. to Plasma Phys. **49**, 316 (2009).

[77] E. Thomas, A.M. Dubois, B. Lynch, S. Adams, R. Fisher, D. Artis, S. Leblanc, U. Konopka, R.L. Merlino, and M. Rosenberg, J. Plasma Phys. **80**, (2014).

Appendix A: Fiji Image Processing and Analysis Code

```
// lineAverageX function - returns average intensity from (x = midx - rangex, y = yset) to
// (x = midx + rangex, y = yset)
function lineAvgX(midx, rangex, yset)
{
	val = 0;
	for (i = (midx - rangex); i < (midx + rangex + 1); i++)
	{
		val += getPixel(i, yset);
	}
	return val/(2*rangex + 1);
}

// lineAverageY function - returns average intensity from (x = xset, y = midy - rangey) to
// (x = xset, y = midy + rangey)
function lineAvgY(midy, rangey, xset)
{
	val = 0;
	for (i = (midy - rangey); i < (midy + rangey + 1); i++)
	{
		val += getPixel(xset, i);
	}
	return val/(2*rangey + 1);
}

// findEdge function - iterates out from inner circle until void edge is found, using
// lineAvg to search for threshold intensity
function findEdge(direction, x0, y0, thresh, range)
{
// UP old version here ------------------------------
	if (direction == "UP")
	{
//		print("UP started");

		intensityAvg = 0;
		x = x0;
		y = y0;
		while (intensityAvg < thresh)
		{
			y--;
			intensityAvg = lineAvgX(x, range, y);
			if (y < (y0 - 400)) { return "overload"}
		}
//		print("UP completed");
		return abs(y0-y);
	}
/*		if (direction == "DOWN")
```

```
    {
//          print("DOWN started");
            intensityAvg = 0;
            x = x0;
            y = y0;
            while (intensityAvg < thresh)
            {
                y++;
                intensityAvg = lineAvgX(x, range, y);
                if (y > (y0 + 400)) { return "overload"}
            }
//          print("DOWN completed");
            return abs(y0-y);
    }
    if (direction == "RIGHT")
    {
//          print("RIGHT started");
            intensityAvg = 0;
            x = x0;
            y = y0;
            while (intensityAvg < thresh)
            {
                x++;
                intensityAvg = lineAvgY(y, range, x);
                if (x > (x0 + 400)) { return "overload"}
            }
//          print("RIGHT completed");
            return abs(x0-x);
    }
            if (direction == "LEFT")
    {
//          print("LEFT started");
            intensityAvg = 0;
            x = x0;
            y = y0;
            while (intensityAvg < thresh)
            {
                x--;
                intensityAvg = lineAvgY(y, range, x);
                if (x < (x0 - 400)) { return "overload"}
            }
//          print("LEFT completed");
            return abs(x0-x);
    }
-------------------------------------------------

    if (direction == "UP")
    {
        int1 = 0;
        int2 = 0;
```

```
        x = x0;
        y = y0;
        diff = 0;
        while (diff < thresh)
        {
            y--;
            int1 = lineAvgX(x, range, y);
            int2 = lineAvgX(x, range, y+30);
//          print("1 = " + int1 + "   2 = " + int2);
            diff = abs(int1 - int2);
            if (y < (y0 - 400)) {return "overload"}
        }
        return abs(y0-y)
    }
*/
    if (direction == "DOWN")
    {
        int1 = 0;
        int2 = 0;
        x = x0;
        y = y0;
        diff = 0;
        while (diff < thresh)
        {
            y++;
            int1 = lineAvgX(x, range, y);
            int2 = lineAvgX(x, range, y-20);
//          print("1 = " + int1 + "   2 = " + int2);
            diff = abs(int1 - int2);
            if (y > (y0 + 400)) {return "overload"}
        }
        return abs(y0-y)
    }

    if (direction == "RIGHT")
    {
        int1 = 0;
        int2 = 0;
        x = x0;
        y = y0;
        diff = 0;
        while (diff < thresh)
        {
            x++;
            int1 = lineAvgY(y+30+range, range, x);
            int2 = lineAvgY(y+30+range, range, x-20);
//          print("1 = " + int1 + "   2 = " + int2);
            diff = abs(int1 - int2);
            if (x > (x0 + 400)) {return "overload"}
        }
```

```
        return abs(x0-x)
    }

    if (direction == "LEFT")
    {
        int1 = 0;
        int2 = 0;
        x = x0;
        y = y0;
        diff = 0;
        while (diff < thresh)
        {
            x--;
            int1 = lineAvgY(y-30-range, range, x);
            int2 = lineAvgY(y-30-range, range, x+20);
//          print("1 = " + int1 + "   2 = " + int2);
            diff = abs(int1 - int2);
            if (x < (x0 - 400)) {return "overload"}
        }
        return abs(x0-x)
    }
}

function void(input, output, filename)
{
    run("AVI...", "select=" + input + filename + " first = 1 last = 300 convert");
    selectWindow(filename);
    run("Z Project...", "projection=[Min Intensity]");
    imageCalculator("Subtract create stack", filename,"MIN_" + filename);
    selectWindow("Result of " + filename);
    run("Z Project...", "projection=[Max Intensity]");
    selectWindow("MAX_Result of " + filename);
    saveAs("png", output + filename);
    close("*");
}

//-------------------------------------------------------------------------------
//-------------------------------------------------------------------------------
//-------------------------------------------------------------------------------
//-------------------------------------------------------------------------------
//-------------------------------------------------------------------------------


vidInput      = "/Volumes/LeBlanc/LeBlancJune2019/2019-06-30/5/Videos/";
imgOutput  = "/Volumes/LeBlanc/LeBlancJune2019/2019-06-30/5/Images/";
imgInput     = "/Volumes/LeBlanc/LeBlancJune2019/2019-06-30/5/Images/";
procOutput  = "/Volumes/LeBlanc/LeBlancJune2019/2019-06-30/5/Processed/";

vidRun = false;
```

```
//--------------------------------------------------------------------------------
//--------------------------------------------------------------------------------


print("\\Clear")
setBatchMode(true);


if (vidRun == true)
{
	vidList = getFileList(vidInput);
	for (i = 0; i < vidList.length; i++)
		{
			void(vidInput, imgOutput, vidList[i]);
			print((i+1)+" / "+vidList.length);
		}
	imgList = getFileList(imgOutput);
}
else
{
	imgList = getFileList(imgInput);
}


//print(imgList.length);
ii = 0;
while (ii < imgList.length)
{
	midX   = 694;
	midY   = 442;
	rightX = 708;
	leftX  = 679;
	topY   = 428; //less than botY, Y counts down
	botY   = 456;


	if (vidRun == true)
	{
		open(imgOutput + imgList[ii]);
	}
	else
	{
		open(imgInput  + imgList[ii]);
	}


	selectWindow(imgList[ii]);
	imgID = substring(imgList[ii],39,44);                                    //Probe Voltage
//	imgID = substring(imgList[ii],11,13)+"."+substring(imgList[ii],14,15);    //Mag R position
```

```
	run("Gaussian Blur...", "sigma=5");


	upLen	= findEdge("UP",	midX,	topY,	30, 3);
	downLen	= findEdge("DOWN",	midX,	botY,	30, 3);
	leftLen	= findEdge("LEFT", leftX,	midY,	5,	5);
	rightLen	= findEdge("RIGHT", rightX, midY,	5,	5);

	print(imgID+"\t"+upLen+"\t"+downLen+"\t"+leftLen+"\t"+rightLen);

// Add overlay markings here
	makeOval(679, 428, 28, 28);
		run("Flatten");
		close("\\Others");
	if (upLen < 1000)
	{
		makeLine(694, 428, 694, (428 - upLen));
		run("Flatten");
		close("\\Others");
	}
	if (rightLen < 1000)
	{
		makeLine(708, 442, (708 + rightLen), 442);
		run("Flatten");
		close("\\Others");
	}
	if (downLen < 1000)
	{
		makeLine(694, 456, 694, (456 + downLen));
		run("Flatten");
		close("\\Others");
	}
	if (leftLen < 1000)
	{
		makeLine(679, 442, (679 - leftLen), 442);
		run("Flatten");
		close("\\Others");
	}


// Save, close, iterate
	saveAs("jpg", procOutput + "PROCESSED-" + imgList[ii]);
	close("*");
	ii++;
}

if (vidRun == true) beep();

setBatchMode(false)
```